Dense Suspension Rheology and Flow Phenomena

by

Sandeep Dileep Kulkarni

A Dissertation Submitted to the Graduate Faculty in Engineering in Partial Fulfillment of the Requirements for the Degree of Doctor of Philosophy
The City University of New York

2010

This manuscript has been read and accepted for the Graduate Faculty in Engineering in satisfaction of the dissertation requirement for the degree of Doctor of Philosophy.

Date	Prof. Jeffrey F. Morris Chair of Examining Committee
Date	Mumtaz K. Kassir Executive Officer
	Prof. Mark Shattuck
	Prof. Ilona Kretzschmar
	Prof. Charles Maldarelli
	Prof. James F. Gilchrist

Supervision Committee

THE CITY UNIVERSITY OF NEW YORK

Abstract

Dense Suspension Rheology and Flow Phenomena

by

Sandeep D. Kulkarni

Advisor: Jeffrey F. Morris

Rheology of concentrated flows of colloidal and non-colloidal suspensions is probed using simulation and experimental techniques. When subjected to shear, a concentrated suspension exhibits a rich variety of behaviors. The striking behaviors vary from shear induced ordering to shear thickening and hydrodynamic instabilities depending on the particle concentration and flow conditions. A range of these behaviors is studied in terms of microscopic and macroscopic response of the system.

The computational studies use Accelerated Stokesian Dynamics (ASD) simulation technique to investigate colloidal suspension flow at low particle Reynolds number. The first study explores shear-induced ordering in colloidal suspensions. The simulations are performed for particle volume fractions $0.47 \leq \phi \leq 0.57$ at Péclet numbers of $1 \leq Pe = 6\pi\eta\dot{\gamma}a^3/kT \leq 10^4$ where η is the suspending fluid viscosity, $\dot{\gamma}$ is the imposed shear rate, a is the sphere radius and kT is the thermal energy. At $Pe \geq 10$, when particle volume fraction is above $\phi \approx 0.50$, the suspensions undergo ordering over extended periods at the onset of flow, with remarkable reduction in the shear viscosity and self-diffusivity. The thixotropic response is a result of microstructural ordering, which is characterized by the real space pair distribution function and its Fourier transform, the static structure factor; both show that the particles tend to flow in chains with hexagonal packing in the plane normal to the flow. An order parameter is formulated to quantitatively describe the strength of this hexagonal

packing.

The second computational study compares the microstructural anisotropy observed in sheared suspensions simulated by the ASD technique ($\phi < 0.50$) to that observed in an experimental study of pressure-driven flow of Brownian suspensions through a micro-channel. In the experiments, three-dimensional particle locations are obtained via confocal microscopy. The features of the pair distribution function obtained experimentally show excellent qualitative match with that obtained from the simulations.

The third simulation study probes shear thickening (or jamming) in Brownian suspensions based on a 'motion correlation' approach. The correlations for the velocity-gradient (y) direction velocities of the particle pairs are studied for ASD simulated suspensions with $0.05 \leq \phi \leq 0.47$ at various Péclet numbers. The pair motion correlations show strong dependence on ϕ and Pe, and this novel approach captures the long-range structures at microscopic level which could be associated with the shear thickening phenomenon.

The experimental work investigates gravity-driven flow of concentrated suspensions ($\phi > 0.50$) of non-Brownian spherical particles through a channel contraction at low Reynolds number. The abrupt change in the flow area at the contraction forms distinct shear-rate regions having different fluid pressures, which are related to the concept of particle pressure. A model involving particle pressure variation coupled to a Darcy-like behavior for the fluid captures the phenomenon of 'self-filtration', in which the effluent material has lower solid fraction than the input suspension.

In the above experimental set-up, when an external load is added on the suspension, the flow transforms from the smooth motion to a periodically alternating fast and slow motion for $\phi \approx \phi_c \geq 0.55$. This remarkable alternating motion is suggestive

of conversion from a liquid suspension into a thickened 'solid-like' system. The periodic flow behavior is found to be robust, occurring for a range of imposed driving pressure level, particle size and viscosity of solvent. The 'self-filtration' is found to be retained in the periodic flow conditions. The coupling of periodic flow behavior to the system's pressure response is investigated.

Acknowledgements

Without guidance and help of several individuals, this dissertation would not have been possible. It is a pleasure to convey my sincerest thanks to all individuals who have contributed in one way or another in completion of this study.

I owe my deepest gratitude to my advisor, Prof. Jeffrey Morris. His hardworking nature and dedication towards science has always inspired me. He has been very supportive throughout the ups and downs of my research work. Our regular discussions were very enlightening as he used to provide his invaluable inputs and always encouraged me to think independently. I learnt from him how to visualize a scientific issue through different perspectives, identify the key factors in the issue, and come up with the most optimistic solution. Furthermore, I think his exceptional presentation techniques and collaborative skills are benchmarks of professional excellence. To sum up, it was an honor for me to work with Prof. Morris and I am very happy to carry the scientific and professional skills I learnt from him throughout my life.

I am very thankful to my PhD committee, Prof. Mark Shattuck, Prof. Ilona Kretzschmar, Prof. Charles Maldarelli and Prof. James Gilchrist for their useful and constructive comments on this thesis. I would also like to thank our collaborators whose involvement is very valuable in my research work. I am grateful to Prof. James Gilchrist and his student Dr. Changbao for collaborating with us and providing us excellent experimental results to compare with our simulation work on Stokesian Dynamics. A special thanks to Dr. Bloen Metzger for his wonderful inputs and ideas on the experimental work we did in collaboration.

I would like to show gratitude to my labmates: Post-doctoral students Yevgeny, Allan, Jorge, Pablo and Himesh, and PhD students Pandurang, Prasad, Xiajuan,

Ehssan and Hamed. Thanks for our fruitful and enlightening discussions and also for providing a cheerful work environment. I am also grateful to lab technicians Andy, Xu and Junjun, and the Levich administrative assistant Mary for their wonderful support during these years.

I am very fortunate to have a great company of friends at the City College. Seniors including Anil, Manoj, Nikhil, Rajesh, John, Shyam, Rohit, Prasad, Amar, and batchmates Vikas and Pratik, and juniors Gogo, Dada, Shripad, Swapnil, Abhinav, Jayant, Vilobh, Ankur and DJ have not only supported my research at various levels but also provided much needed family environment far away from home.

I would also like to express my sincere appreciation to many of my school, undergraduate and graduate teachers who have been very helpful in shaping my career and nurturing my interest in science.

Finally, I would like to dedicate this thesis to my family. My parents, Mr. Dileep Kulkarni and Mrs. Sunita Kulkarni and my brother Mandar have supported me at each step and made many sacrifices to make my career successful. My wife, Deepali was always there for me during last two years of my PhD. I was only able to do my best as she was around.

Sandeep D. Kulkarni

Contents

List of Figures

List of Tables

Chapter 1

Introduction

1.1 Background and Motivation

Multiphase flows are ubiquitous in nature and in industrial processes. Suspensions are an important class of multiphase systems, where discrete solid particles are suspended in a continuous fluid medium. Typical examples include industrial products like paints, cement, personal care products and biological fluids such as blood and foodstuff. It is a challenge to understand how the material's microscopic and macroscopic properties are affected by various types of external perturbations. Laboratory experiment, analytical theory and computer simulation are the tools which are extensively used to address these challenges. A complete understanding of the transport properties of the suspensions, especially in very dense systems, is not yet available and remains a fundamental problem in fluid dynamics.

The governing physics roughly depends on the length scale of the particulate system and thus, the simulation techniques or analytical tools required change accordingly. Figure 1.1 describes the simulation techniques appropriate for the particle sizes ranging from Angstrom to meter-scale grains. At molecular scale, Molecular Dynamics is used where particles interact through molecular inter-particle forces governed by Newton's law of motion [1]. For larger particles in the range of

$O(10^{-8})$ m to $O(10^{-3})$ m, it is computationally more efficient to consider the solvent molecules as continuum. The colloidal particles interact through inter-particle (e.g. electrostatic), Brownian and hydrodynamic forces. The Brownian forces arise from thermal fluctuations of particles which are smaller than $1\mu m$. As shown in figure 1.1, this range of particle length mostly satisfies low Reynolds number condition ($Re = \rho U a/\eta << 1$, where ρ is the number density, U is the characteristic particle velocity, a is the particle radius and η is the fluid viscosity), where the hydrodynamic interactions are governed by the Stokes equation. The simulation method which accounts for these interactions is Stokesian Dynamics [2]; this simulation technique and experiments in the same range of particle length scale are the main focus of interest for the present study.

For much larger particle size where $Re >> 1$, the motion of particles is governed by inelastic collision; the fluid motion is neglected and Granular Dynamics is used to simulate the particle motion using Newton's laws of motion [3]. When the Reynolds number is neither large ($Re >> 1$) nor small ($Re << 1$), the inertial effect of the flow needs to taken into account [4]. The high Reynolds number flow, however, is not the focus of this study. Our interest of study is the Stokes flow regime ($Re << 1$) and the simulation tool for this regime, Stokesian Dynamics, is established based on the following development of analytical theories.

A system comprising of monodisperse hard-sphere particles suspended in a Newtonian liquid arguably represents the simplest type of suspension. The suspension viscosity, defined as the ability of the system to resist the flow, is higher than the suspending liquid viscosity because of the presence of non-deformable solid particles. Theoretical studies demonstrating the effect of hard-sphere concentration on the suspension viscosity are precursors for the modeling of suspension flows. Einstein [5] found that the suspension viscosity η was increased over that of solvent by a

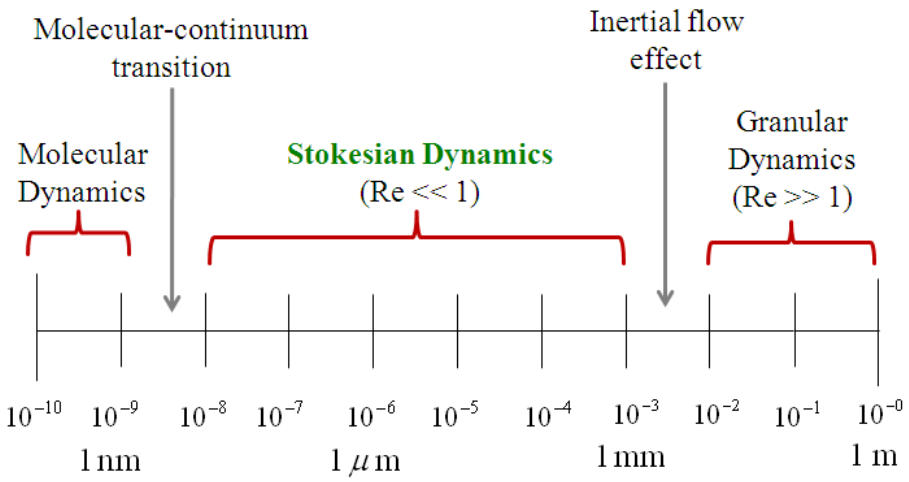

Figure 1.1: Simulation technique and particle size.

factor of $(1+5/2\phi)$. The detailed motion of the two-phase flow can be solved based on the equation of motion for suspending fluid with proper boundary conditions. The equation of motion or the Navier-Stokes equation for the Newtonian fluid is given by

$$Re(\frac{\partial u}{\partial t} + \mathbf{u} \cdot \nabla \mathbf{u}) = -\nabla p + \nabla^2 \mathbf{u}, \tag{1.1}$$

where p and $\mathbf{u}$ are the fluid pressure and velocity respectively. The distance, velocity and time are made dimensionless with a, U and a/U respectively. The particle Reynolds number Re represents the ratio of inertial to viscous forces. When viscous forces are dominant and inertia is completely negligible, $Re \to 0$ which is referred as Stokes flow.

The linearity of Stokes equation gives ability to obtain analytical solution to the flow. Batchelor [6, 7] provided solution for hydrodynamic interactions for two particles in simple shear flow. He also performed calculations for bulk stress which has contributions from the continuous fluid phase and the discrete particle phase [8]. Further work in this area include more accurate calculations of two-body

hydrodynamic resistance functions which involves near-field lubrication forces and far-field interactions [9, 10, 11, 12]. These theoretical studies have been limited to dilute concentrations where two-body interactions dominate. Nevertheless, they have identified fundamental mechanism of particle interactions at low Reynolds number flow and provided a foundation to the simulation method of Stokesian Dynamics. The Stokesian Dynamics (SD) simulation can capture the behavior at high particle concentrations by accounting for many-body hydrodynamic interactions [13, 2]. This is carried out based on pairwise additivity of hydrodynamics interactions using superposition of the forces; the linearity of Stokes flow allows superposition of independent solutions and hence a combined effect of hydrodynamic and non-hydrodynamic (Brownian and interparticle) interactions could be investigated. The simulation method is described in further details in chapter 2.

The findings of Stokesian Dynamics simulation and various analytical techniques have an excellent agreement with the key rheological results of the experimental work on sheared suspensions. The shear thinning and thickening responses observed in the SD simulation as the Péclet number (ratio of shear to Brownian forces) is varied [14] are in good agreement with the experiments on sheared suspensions [15, 16]. The thickening behavior is also predicted theoretically based on the dependence of the value of pair distribution function at contact on the Péclet number, $g(2) \sim Pe$ [17].

The SD simulation [14, 18] and analytical [19, 17] results have shown that strongly sheared suspension generate normal stresses; this behavior is validated by the experimental studies in various flow geometries [20, 21, 22, 23]. The role of shear-induced anisotropy of the suspension microstructure [24] in generating the normal stresses is investigated thoroughly through theory and simulations [17, 14, 18]; the anisotropic behavior under shear agrees qualitatively with the experimental findings [25, 26].

In the experiments of low-Reynolds-number suspension flows that involve variation in the shear-rate across the flow-channel, a phenomena of 'shear-induced migration' is observed [27, 28, 29]. This response is studied in relation with the particle pressure Π which is the mean normal stress exerted by the particle phase in a sheared suspension $\Pi = -\frac{1}{3}[\sum_{11}^{p} + \sum_{22}^{p} + \sum_{33}^{p}]$ [30]; Π is evaluated using SD simulations [18, 31] and experiments [21, 32]. The migration is modeled based on formulation of constitutive relations which relate the suspension stresses to the strain rate [33, 34, 35].

Despite the noted substantial progress in understanding of the suspension flows, a wide range of phenomena, especially in very dense systems ($\phi > 0.35$) are not well understood for various flow conditions. The central goal of this study is to explore rheology of concentrated flows of colloidal and non-colloidal suspensions using simulation and experimental techniques. When subjected to shear, a concentrated suspension demonstrates rich variety of behaviors that ranges from shear induced ordering to shear thickening and jamming depending on the particle concentration and flow conditions. We investigate the response of concentrated colloidal systems computationally using Accelerated Stokesian Dynamics simulation at microscopic and macroscopic level. Experimentally, we study flow-induced dilation and transient jamming observed in the flow of non-Brownian suspensions through a contraction geometry. The relevant background literature in different areas of our study is thoroughly discussed in respective chapters of this thesis.

1.2 Outline

The thesis is arranged as follows. Chapter 2 describes the Accelerated Stokesian Dynamics (ASD) simulation method for solving flow of sheared colloidal suspensions at low Reynolds number condition. Based on the knowledge of time evolution

of particle positions and velocities, the microscopic properties of the system are investigated. The ASD technique also provides macroscopic properties of shear and normal stresses using the calculations of the bulk stresses in the system.

In chapter 3, shear-induced ordering in colloidal suspensions is computationally investigated. The range of parameters for which this order occurs is probed by simulation of monodisperse Brownian hard-sphere suspensions using the ASD technique. The simulations are conducted for dense systems with particle volume fractions $0.47 \leq \phi \leq 0.57$. The Péclet is varied as $1 \leq Pe = 6\pi\eta\dot{\gamma}a^3/kT \leq 10^4$ where a is the sphere radius $\dot{\gamma}$ is the imposed shear rate, η is the suspending fluid viscosity, and kT is the thermal energy. As the flow begins, the suspensions undergo gradual ordering with time for particle volume fraction above $\phi = 0.50$ at $Pe \geq 10$. The ordering is associated with considerable reduction in the self-diffusivity and shear viscosity. The time-dependent viscosity response is a result of microstructural ordering, which is characterized microscopically by the real space pair distribution function and its Fourier transform, the static structure factor. Both microscopic properties show that the particles tend to flow in chains with hexagonal packing in the plane normal to the flow. The strength of this hexagonal packing is quantitatively described by an order parameter C_6. This ordering is not observed at $Pe = 1$. Step changes in Pe are found to result in transitions of the structure and rheology, and hence the steady state rheology determined is uniquely associated with the flow conditions and particle fraction for most of the parameter space studied; however, near the boundary with respect to Pe between flow-induced order and disordered states of suspension at $\phi = 0.55$, the ultimate structure is history dependent within the typical simulation duration of material strain of $O(100)$.

In chapter 4, we compare the anisotropic suspension microstructure obtained from the ASD simulated shear flow to that observed in experiments. The experiments

are conducted to study the pressure-driven flow of Brownian suspensions through micro-channels where the 3D particle locations are obtained by confocal laser scanning microscopy (the experiments are carried out by our collaborators at Lehigh University). The simulations capture the qualitative characteristics of the suspension microstructure that are observed experimentally.

Chapter 5 investigates the phenomena of shear thickening and jamming in suspensions at microscopic level. The microstructure in sheared suspensions has been extensively probed in earlier studies based on the spatial distribution of particles. In this work, a novel tool of pair motion correlation is demonstrated to study the microscopic response of the system. The shear flow of hard-sphere Brownian suspensions is simulated using the ASD technique. The correlations for the velocity-gradient (y) direction velocities of the particle pairs are probed at various Péclet numbers with a range of particle volume fractions between $0.05 \leq \phi \leq 0.47$. The y velocity pair correlations show strong dependence on ϕ and Pe, and notably, they capture the long-range structures which could be associated with the shear thickening behavior. The pair motion correlations in the ASD simulated flow are compared to that in Brownian Dynamics simulated flow to investigate the role of hydrodynamics in the formation of the long-range structures.

Chapter 6 and 7 discuss our experimental work on dense suspension flows. Gravity-driven flow of concentrated suspensions ($\phi > 0.50$) of non-Brownian spherical particles through a channel contraction at low Reynolds number is studied in chapter 6. We observe that the effluent material leaving the contraction has a consistently lower solid volume fraction relative to the input concentration; this phenomenon is known as 'self-filtration'. The internal stress during flow is investigated through measurement of the liquid pressure along the channel boundary, at points in and well before the throat of the contraction. There is strong correlation of the liquid pressure

with the self-filtration. The relation of this liquid pressure to the shear-induced particle pressure Π, a strong function of ϕ and shear rate, is studied.

Chapter 7 describes the experiments on flow through the contraction driven by an imposed load. The suspension flows smoothly under its own weight. Remarkably, under externally added load, the dense suspension $\phi \approx \phi_c \geq 0.55$ flows periodically, alternating between fast and slow motions. The alternating motion is indicative of a transition from the 'liquid-like' state to a thickened 'solid-like' system. The phenomenon is found to be robust, occurring for a range of imposed external load, particle size and concentration, and viscosity of solvent. The periodic flow behavior is thoroughly studied as a function of the above stated parameters. Both steady and periodic flows exhibit 'self-filtration'. The system's pressure response is investigated in relation to the two striking phenomena of periodic flow behavior and self-filtration.

Chapter 2

Accelerated Stokesian Dynamics : simulation method

With Accelerated Stokesian Dynamics (ASD), we solve the equations governing the motion of particles suspended in sheared viscous fluid at low particle Reynolds number ($Re = \frac{\rho\dot{\gamma}a^2}{\eta}$, where ρ is the number density, $\dot{\gamma}$ is the shear rate, a is the particle radius and η is the suspension viscosity). Accelerated Stokesian Dynamics is an advanced version of conventional Stokesian Dynamics (SD). An important advantage of ASD, which uses fast Fourier transform method, is considerably lower computational cost of $O(N \ln N)$ relative to the $O(N^3)$ of standard SD, where N is the number of particles in a periodic unit cell. Here, we describe in brief the fundamental evolution equation on which both SD and ASD simulations are based. SD and ASD are discussed in further details by Brady & Bossis [2] and Sierou & Brady [36] respectively. The ASD code with Brownian motion is provided by Banchio & Brady [37].

For the system of particles suspended in an incompressible Newtonian fluid, the fluid motion is described by the Stokes equation while the particle motion is described

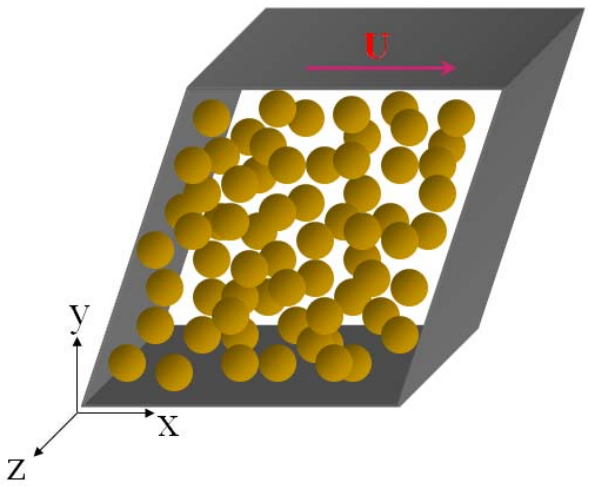

Figure 2.1: Periodic simulation box with Less-Edwards boundary conditions

by the N-body Langevin equation. It can be stated as

$$m\frac{d\mathbf{U}}{dt} = \mathbf{F}^H + \mathbf{F}^p + \mathbf{F}^B, \tag{2.1}$$

where $\mathbf{F}^H$ is the hydrodynamic force while $\mathbf{F}^B$ is the stochastic force due to Brownian motion and $\mathbf{F}^p$ defines the inter-particle/external force. Thus, the rate of change of the particle velocity vector is expressed as the sum the forces.

The hydrodynamic force $\mathbf{F}^H$: The hydrodynamic force-torque equation is characterized on the basis of linearity of the governing Stokes equation [13]. It is stated as

$$\mathbf{F}^H = -\mathbf{R}_{FU} \cdot \mathbf{U}^* + \mathbf{R}_{FE} : \mathbf{E}^\infty, \tag{2.2}$$

where $\mathbf{U}^*$ describes the particle translational-angular velocity relative to the bulk fluid translational-angular velocity estimated at the particle center. The term $\mathbf{R}_{FU}$ defines the hydrodynamic force/torque on the particle due to their motion relative to fluid while the term $\mathbf{R}_{FE}$ is the hydrodynamic force/torque on the particles due to

imposed shear flow. The symmetric part of the velocity gradient tensor is depicted by $\mathbf{E}^{\infty}$.

The Brownian force $\mathbf{F}^{B}$: The thermal fluctuations give rise to the Brownian or stochastic force. The expressions for the Brownian force are stated as

$$< \mathbf{F}^{B} >= 0, \tag{2.3}$$

$$< \mathbf{F}^{B}(0)\mathbf{F}^{B}(t) >= 2kT\mathbf{R}^{FU}\delta(t), \tag{2.4}$$

where T is the absolute temperature, k is the Boltzmann constant and $\delta(t)$ is the delta function.

The interparticle force $\mathbf{F}^{p}$: For the present study, the interparticle are introduced to avoid the overlap of particles. Note that, in fact, the hydrodynamic lubrication forces between the particle would not allow the particle to overlap, but due to the limitation in choosing the time-step for calculations (smaller the time-step, higher the computational cost), there is a possibility of particle overlaps. The form of hard-sphere interparticle force is described by $\mathbf{F}^{p} = \frac{1}{2}kT\hat{\mathbf{r}}\delta(r-2a)$. The dimensionless parameter γ^{*} determines the relative magnitude of the shear and the interparticle forces.

The Langevin equation (2.1) can be integrated twice to give the time evolution of the particle positions as

$$< \Delta\mathbf{x} >= Pe\{\mathbf{U}^{\infty} + \mathbf{R}_{FU}^{-1} \cdot [\mathbf{R}_{FE} : \mathbf{E}^{\infty} + \gamma^{*-1}\mathbf{F}^{P}]\}\Delta t + \nabla \cdot \mathbf{R}_{FU}^{-1}\Delta t + \mathbf{X}(\Delta t). \tag{2.5}$$

Here, Peclet number $Pe = \dot{\gamma}a^{2}/2D$ is the measure of the relative strength of shear to Brownian forces; D is the diffusivity of an isolated particle. Equation (2.5) suggests

that the suspension behavior depends on the dimensionless parameters Pe and γ^{*-1}. The contribution from the hydrodynamic shear forces is given by $(\mathbf{U}^{\infty} + \mathbf{R}_{FU}^{-1} \cdot \mathbf{R}_{FE} : \mathbf{E}^{\infty})\Delta t$. The contribution from interparticle forces is represented by $(\mathbf{R}_{FU}^{-1}\mathbf{F}^{P})\Delta t$ while the Brownian contribution is given by the configuration space-divergence of N-particle diffusivity $\mathbf{R}_{FU}^{-1}\Delta t$ and a random step $\mathbf{X}(\Delta t)$. The Stokesian Dynamics simulation is based on equation (2.5). Once the initial configuration is given, equation (2.5) calculates the dynamic evolution of the suspension microstructure. This understanding of the evolving suspension microstructure is used to determine the macroscopic quantities like diffusivity and to study the pair microstructure in the simple shear flow.

The simulations are performed using periodic boundary conditions in all directions: x, y and z define the flow, the velocity gradient and the vorticity directions, respectively. The Lees-Edwards periodic boundary conditions for shear flow are used in the simulations [1]. For all results presented here, the time is measured in dimensionless form as $\dot{\gamma}t$, which is equivalent to strain. Distances are made dimensionless with particle radius a. All simulations reported are run with 512 particles in the simulation box.

Chapter 3

Ordering transition and structural evolution under shear in Brownian suspensions

3.1 Introduction

In this work, we address the transition of hard sphere colloids from a disordered liquid-like state to a highly-ordered condition due to imposed shearing flow. Transitions from a disordered to ordered state, due either to a thermodynamic transition or to flow, have a history of study. In the absence of flow, systems of hard spheres in vacuum have been extensively studied by molecular dynamics computer simulation dating to Alder *et al.* [38]. These simulations predict a thermodynamic phase transition. Although they do not include a solvent, the simulation results are applicable to the equilibrium properties of colloidal suspensions, as the presence of solvent does not affect the equilibrium structure of colloidal hard spheres. Experimentally, the transition has been studied for colloidal suspensions by many, including Pusey & van Megen [39] and Paulin & Ackerson [40]. The onset of crystallization, or "freezing" transition, of monodisperse suspensions of hard-sphere

This chapter is published as *Ordering transition and structural evolution under shear in Brownian suspensions*, S. D. Kulkarni and J. F. Morris, J. Rheol. **53**, 417 (2009)

colloids occurs at $\phi = \phi_F = 0.494$, where ϕ denotes particle volume fraction. There is coexistence of fluid and crystal forms for $\phi_F \leq \phi \leq \phi_M = 0.545$. The system is in crystalline form between ϕ_M and the glass transition point $\phi_G = 0.58$. Above $\phi_G = 0.58$, up to random close packing $\phi_{RCP} = 0.64$, a long-lived metastable glassy state is formed. Thus, a non-flowing colloidal suspension exhibits a 'disorder-order' thermodynamic phase transition at the onset of coexistence of crystal and fluid, while beyond the glass transition point the disordered liquid-like state fails to order and remains non-ergodic.

When a shear flow is imposed, the behavior depends not only on ϕ but also on the ratio of shearing to thermal motions, characterized by the Péclet number, $Pe = 6\pi\eta\dot{\gamma}a^3/kT$ where η is the suspending fluid viscosity, $\dot{\gamma}$ is the imposed shear rate, a is the sphere radius and kT is the thermal energy. Sheared colloidal suspensions near and beyond the equilibrium freezing fraction ϕ_F have been studied both experimentally and by simulations. We consider first experimental work. Hoffman [41] showed experimental evidence of discontinuous viscosity behavior for concentrated mono-disperse suspensions ($\phi > 0.50$) at high shear rates beyond the instability point and related this behavior to an 'order-disorder' transition with the ordered state being a hexagonal arrangement in the flow-gradient plane, which differs from the orientation of hexagonal order in the gradient-vorticity plane seen in this work. Ackerson [42] investigated hard-sphere colloidal suspensions undergoing steady and oscillatory shear flows, finding string-like and face-centered-cubic ordering near and above ϕ_F. Haw *et al.* [43] found hexagonally ordered regions when suspensions of sterically stabilized particles were subjected to oscillatory shear. Voltz *et al.* [44] observed thixotropic behavior of colloidal suspensions at high Péclet number, but did not describe ordering. Silbert *et al.* [45] considered by analytical methods the shear-thinning behavior of concentrated aggregated dispersions beyond the freezing point.

Butera *et al.* [46] observed in concentrated suspension of charged colloidal spheres that a crystalline state is formed rapidly after flow cessation from a disordered shear thickened state. Paulin *et al.* [47] found hexagonal packed planes stacked in the direction of shear gradient in concentrated soft-sphere suspensions under shear.

Turning to simulation, Sierou & Brady [18] studied sheared non-Brownian suspensions ($Pe = \infty$) using the Accelerated Stokesian Dynamics (ASD) technique [36]. These authors investigated the dependence of the relative viscosity η_r (viscosity of the suspension relative to that of the suspending fluid) on ϕ up to $\phi = 0.60$, and showed that η_r increases with ϕ up to $\phi = 0.50$, whereas for $\phi > 0.50$ it falls to $\phi = 0.55$ and then increases strongly for $\phi = 0.60$, as illustrated by figure 3.1. It was suggested that the fall in the relative viscosity for $0.50 \leq \phi \leq 0.55$ is related to ordering of the microstructure. Leshansky & Brady [48] computed by ASD the self-and gradient-diffusivity coefficients in non-Brownian suspensions based on the dynamic structure factor approach. These authors observed an order-of-magnitude drop in the self-diffusivity coefficients for $\phi = 0.55$ compared to $\phi = 0.50$. The dramatic variation in transport properties of viscosity and self-diffusion is correlated with ordering of the microstructure. Note that neither Sierou & Brady [18] nor Leshansky & Brady [48] considered Brownian motion. The appearance of shear-induced order at $Pe = \infty$ very near the onset value of ϕ for fluid and crystal coexistence ($\phi_F = 0.494$) in the equilibrium system of $Pe = 0$ motivates this work. We seek using ASD inclusive of Brownian motion [37] to determine whether the appearance of order, and sharply weaker rheological response, in this range of ϕ is a general feature of near-hard-sphere dispersions. It is our goal to elucidate the disorder-order behavior of sheared concentrated colloidal systems with respect to both ϕ and Pe, and to determine the time dependence of the structural development.

We study the behavior of sheared concentrated colloidal systems using ASD

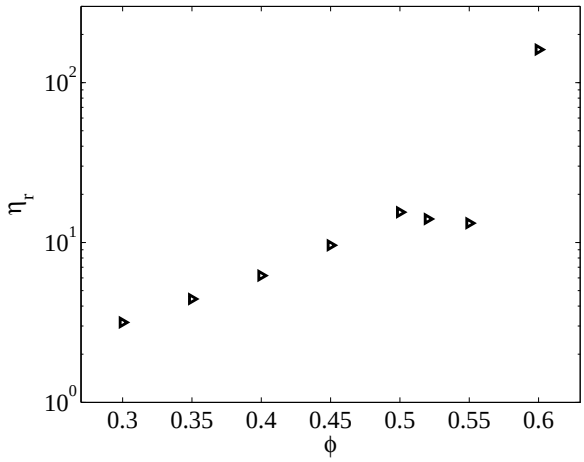

Figure 3.1: Dependence of the relative viscosity on particle volume fraction; Sierou & Brady (2002) : ASD, $N = 512$, $Pe = \infty$.

simulation at $Pe = 1$, 10, 100, and 1000, with limited simulations at $Pe = 10^4$. The microstructural properties of the system are investigated based on analysis of both the pair distribution function and its Fourier transform, the static structure factor. The macroscopic properties of the self-diffusivity and the relative viscosity are studied. We find that at $Pe = 1$, where the shear and Brownian forces are comparable, no signature of ordering is found as ϕ is raised to $\phi = 0.57$; both microscopic as well as macroscopic properties behave monotonically with increasing particle ϕ. On the other hand, at $Pe = 10$, 100, and 1000, particles progressively tend to flow in chains with hexagonal packing in the plane normal to the flow for $\phi > 0.50$. At $Pe = 1$, our results do not show ordering, and thus the equilibrium order is separated by a region in parameter space from the shear-induced ordering at elevated Pe. While there is not a continuous ordering region in parameter space, there is apparently a general tendency toward an ordered state in these very concentrated hard-sphere suspensions. Interesting, the transition with respect to ϕ seems to be largely insensitive to Pe. Some caution is necessary because we have not precisely determined the line between ordered and disordered states in ϕ-Pe space. Further discussion of the transition is

found in §3.4.

Thixotropic behavior of concentrated suspensions at a wide range of Péclet numbers and the relative viscosity dependence on ϕ and Pe are presented in §3.3. In §3.4 we describe the microstructure, and present an order parameter to quantify the degree of ordering observed. We apply an approach based on the ideas of dynamic light scattering which addresses relaxation of the fluctuations in the particle number density in §3.5. This approach provides both a microscopic measure, the static structure factor, and a macroscopic measure, the self-diffusivity.

3.2 Simulation method

We use Accelerated Stokesian Dynamics (ASD) technique to solve the equations governing the motion of particles suspended in sheared viscous fluid which is described in chapter 2.

3.3 Relative viscosity

The bulk stress $< \mathbf{\Sigma} >$ is defined as an average stress over the volume of simulation box containing N particles and is described as

$$< \mathbf{\Sigma} >= -p_f \mathbf{I} + 2\eta \mathbf{E}^{\infty} + < \mathbf{\Sigma} >_p, \tag{3.1}$$

where $2\eta\mathbf{E}^{\infty}$ and p_f are the deviatoric stress and pressure of the fluid and $< \mathbf{\Sigma} >_p$ is the particle stress contribution. The details of calculation of bulk stress are described in Sierou & Brady [36] and Banchio & Brady [37].

The viscosity of suspension relative to that of the suspending fluid is given by

$$\eta_r = \frac{< \Sigma_{xy} >}{2\eta E_{xy}} = 1 + \eta_r^p, \tag{3.2}$$

indicating η_r^p to be the particle phase contribution to the relative viscosity. We study the evolution of η_r with time (or strain) for $\phi = 0.47$ to $\phi = 0.57$ at various Péclet numbers. The observed thixotropic behavior, i.e. a decrease in η_r over time at a constant shear rate, and the dependence of η_r on ϕ and Pe are discussed.

3.3.1 Thixotropic behavior

At $Pe = 1$, the mean relative viscosity is independent of time at $Pe = 1$ up to $\phi = 0.57$. We observe that η_r increases monotonically with ϕ and fluctuates around its mean for $0.47 \leq \phi \leq 0.57$, as illustrated in figure 3.2a. Figure 3.2b shows that at $Pe = 10$, η_r is independent of time up to $\phi = 0.50$ but decreases with time for $\phi > 0.50$. A simple measure of the relaxation time τ for these decays of the relative viscosity is obtained from a fit to

$$\eta_r(t) = A \exp(-t/\tau) + \eta_r^\infty, \tag{3.3}$$

where η_r^∞ is the steady viscosity obtained at the conditions of interest. At $Pe = 10$, $\tau \approx 20$ to 70 for $\phi = 0.51$ – 0.57.

For a fixed solid fraction with $\phi > 0.50$ at $Pe = 10$, there are considerable fluctuations in τ for different initial configurations. For example, for $\phi = 0.55$ at $Pe = 10$, the relaxation times τ with three different initial configurations were 22, 30 and 36. This variability indicates some arbitrariness in defining the onset of this relaxation process, so the relaxation time can only be used in a relative sense. One

cannot necessarily ascribe a single relaxation time to the phenomena underlying the thixotropy, but it is worth noting that the exponential fit to the decaying states is reasonably good with the typical quality measure for linear regression satisfying $R^2 > 0.96$.

As shown in Table 3.1a, the general trend for the relaxation time τ is to decrease with increasing ϕ between $\phi = 0.51$ and $\phi = 0.57$. We note that in some realizations, the system does not immediately exhibit decaying viscosity. As examples, consider $\phi = 0.54$ and $\phi = 0.57$ at $Pe = 10$ shown in figure 3.2b. In these realizations, the relaxation times τ are measured once η_r begins decaying approximately in exponential form. To further characterize these states, we perform many realizations with different initial configurations for $\phi = 0.54$ as well as for $\phi = 0.57$ at $Pe = 10$. For $\phi = 0.54$ at $Pe = 10$, one of six realizations showed slower decay in the beginning while for $\phi = 0.57$ at $Pe = 10$, two of six showed non-decaying states in the beginning.

At $Pe = 100$ and $Pe = 1000$, η_r is again independent of time up to $\phi = 0.50$, as illustrated by figures 3.2c and 3.2d. The dimensionless relaxation times τ for these larger Pe (for $\phi > 0.50$) have about the same range of values as for $Pe = 10$; the similarity of these relaxation times, scaled with shear rate, for different but elevated Pe indicates clearly that the decay process is controlled by flow-driven interactions. Table 3.1b and 3.1c shows that the general trend is for τ to decrease from $\phi = 0.51$ to 0.57. While the mechanistic basis for the ϕ-dependence of τ is not known, it may be due simply to intensified hydrodynamic effects: the timescale for the decay scales as $\dot{\gamma}^{-1}$ and is thus a result of hydrodynamic interactions which become more intense as ϕ increases.

Suspensions which exhibit thixotropy have also been studied following a step change in Pe. At $Pe = 1000$ for $\phi = 0.55$, after evolution to a strain of 50, the suspension is subjected to a step decrease to $Pe = 1$. The relative viscosity quite

rapidly rises and asymptotically approaches the steady state value seen for a system sheared only at $Pe = 1$, as shown in figure 3.3a. The suspension at $Pe = 1000$ and $\phi = 0.55$ at $\dot{\gamma}t = 200$ is nearly at steady state viscosity, and is subjected to a step increase in shear rate to $Pe = 10^4$. As shown by figure 3.3b, η_r rises weakly with an overshoot and then settles at a slightly higher value. Step changes from large Pe to $Pe = 2$ exhibit a richer behavior which will be discussed in §3.4 in connection with the observed order.

3.3.2 Relative viscosity dependence on ϕ

We compare the relative viscosities found at large ϕ for given Péclet numbers. As shown by figure 3.2a, at $Pe = 1$, η_r increases monotonically up to $\phi = 0.57$. At $Pe \geq 10$, η_r increases with ϕ up to $\phi = 0.50$; however, for $\phi > 0.50$, η_r becomes time dependent. If $\dot{\gamma}t = 5$ is considered, η_r increases with ϕ for all concentrations studied (figure 3.4b). This early time data is compared with experimental data on high shear viscosities of hard sphere dispersions by Phan *et al.* [49], corresponding to $Pe = 0.5$ to 22, and there is seen to be close agreement with the $Pe = 10$ early time data of the present study; no thixotropic behavior was reported from these experiments, perhaps owing to the polydispersity of $\approx 5\%$.

In contrast to the early-time data, at $\dot{\gamma}t = 50$, we find $\partial\eta_r/\partial\phi < 0$ for $\phi > 0.50$, as shown in figure 3.4a for $Pe = 1000$. The curve has a plateau between $\phi = 0.51$ and $\phi = 0.55$, and higher values are seen for $\phi > 0.55$. This behavior is similar to that at $Pe = \infty$ studied by Sierou & Brady [18], who considered $\phi = 0.55$ and $\phi = 0.60$ with no intermediate loadings.

3.3.3 Relative viscosity dependence on Pe

Foss & Brady [14] studied the dependence of η_r on Péclet number for $0.316 \leq \phi \leq 0.49$ using Stokesian Dynamics, with $N = 27$ to 123 particles in the unit cell. They observed shear thinning for $Pe \approx 10$ and smaller, while shear thickening behavior for higher Pe. We observe similar behavior over this range of ϕ. As noted, for $\phi > 0.50$, η_r becomes time dependent and the issue is more complicated. If η_r at $\dot{\gamma}t = 5$ is considered, shear thinning is seen at Péclet numbers lower than $Pe \approx 10$ (η_r decreases from $Pe = 1$ to 10: figures 3.2a and 3.2b) while shear thickening is seen at higher Pe (figure 3.4b). In thixotropic systems for $\phi > 0.50$ and $Pe \geq 10$, we examine the behavior of the system after $\dot{\gamma}t = 150$. The suspension also shear thickens here, as illustrated by examination of results at $Pe = 10$, 100, and 1000 in figure 3.4c, but has much lower viscosity values than in the early time states.

(a) $Pe = 10$

ϕ	η_r ($\dot{\gamma}t = 5$)	η_r ($\dot{\gamma}t = 150$)	τ
0.51	12.3	8.7	61
0.53	16.6	9.3	43
0.55	22.2	10.6	30
0.57	32.2	22*	65*

(b) $Pe = 100$

ϕ	η_r ($\dot{\gamma}t = 5$)	η_r ($\dot{\gamma}t = 150$)	τ
0.51	14.3	11	47
0.53	17.1	10.3	41
0.55	24.7	11.9	36
0.57	38.7	15.2	30

(c) $Pe = 1000$

ϕ	η_r ($\dot{\gamma}t = 5$)	η_r ($\dot{\gamma}t = 150$)	τ
0.51	16.6	15.2	52
0.53	20.4	13.7	40
0.55	27.1	14.4	33
0.57	40.1	20*	26*

Table 3.1: Relative viscosity at $\dot{\gamma}t = 5$ (η_r^5), at $\dot{\gamma}t = 150$ (η_r^{150}) and relaxation times τ for a representative set of runs for $\phi > 0.50$ at various Péclet numbers. For measurement of relaxation times τ using equation (3.3), we choose $\eta_r^\infty = \eta_r^{150}$, except for the cases indicated by an asterisk, where decay is delayed and $\eta_r^\infty = \eta_r^{200}$.

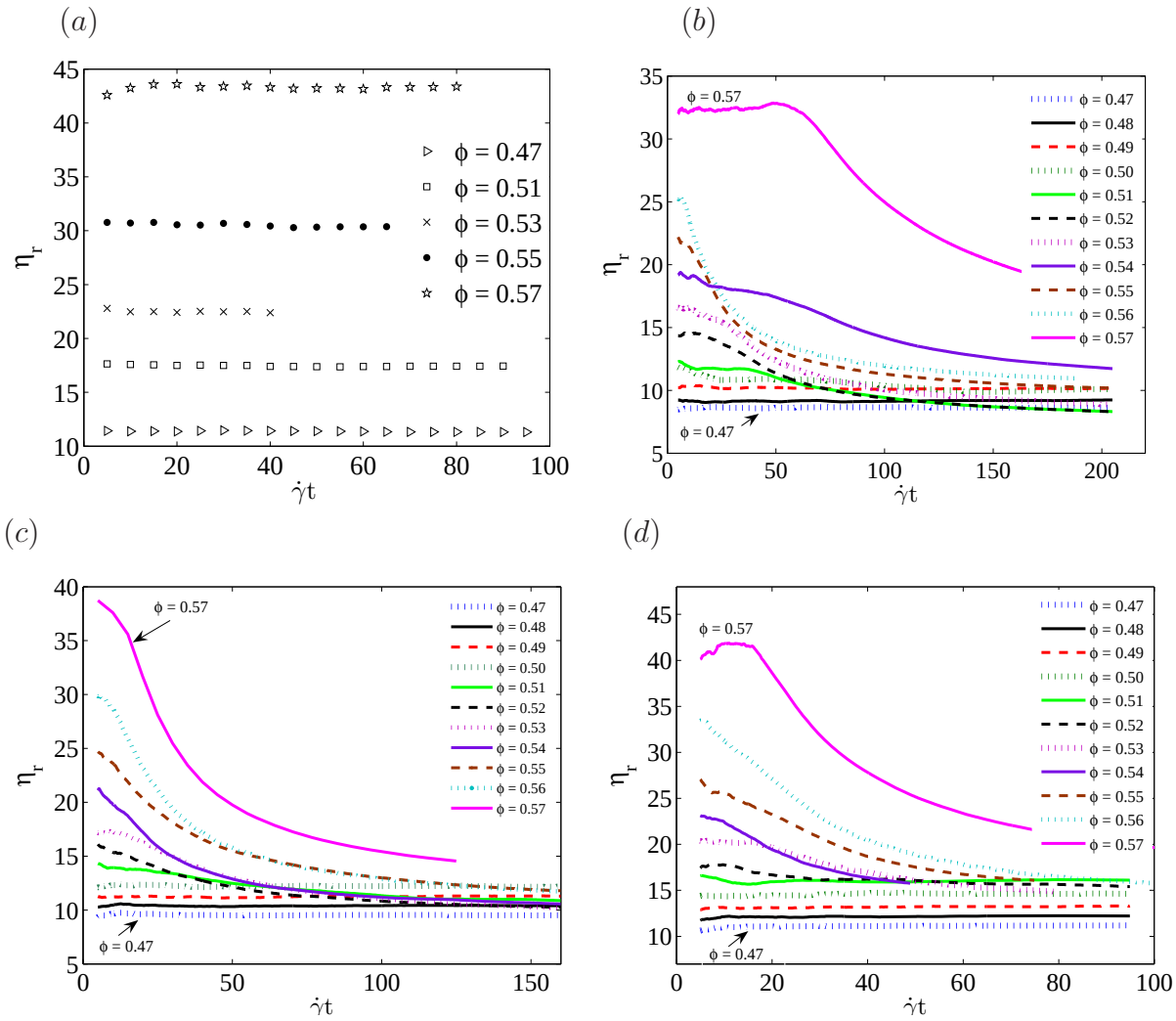

Figure 3.2: Dependence of the relative viscosity on dimensionless time for different ϕ (a) at $Pe = 1$; (b) at $Pe = 10$; (c) at $Pe = 100$; (d) at $Pe = 1000$. To help readers through the crowded figures, we note that the left end data increases monotonically with ϕ.

(a)

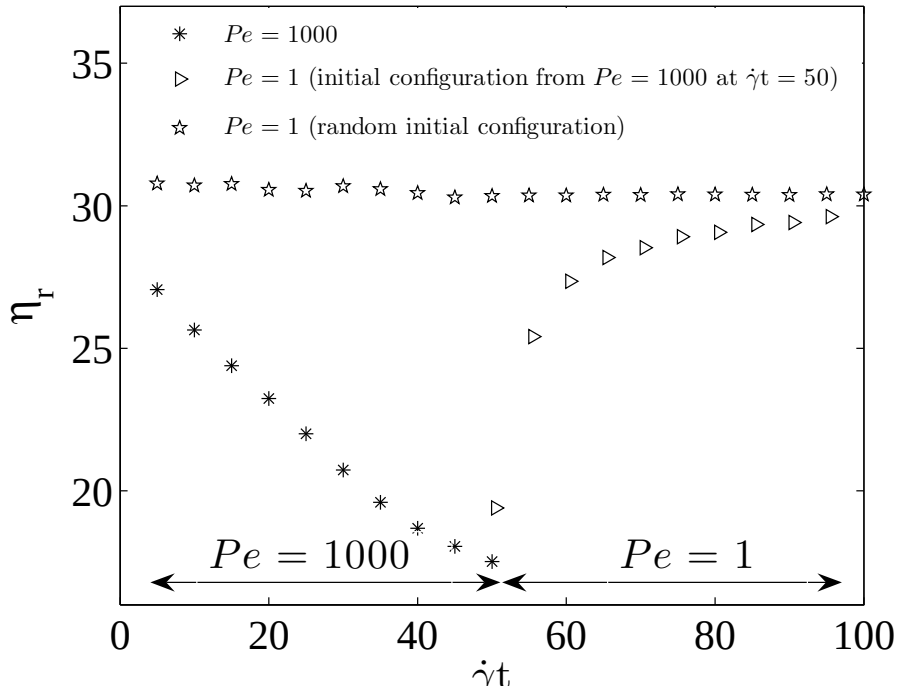

(b)

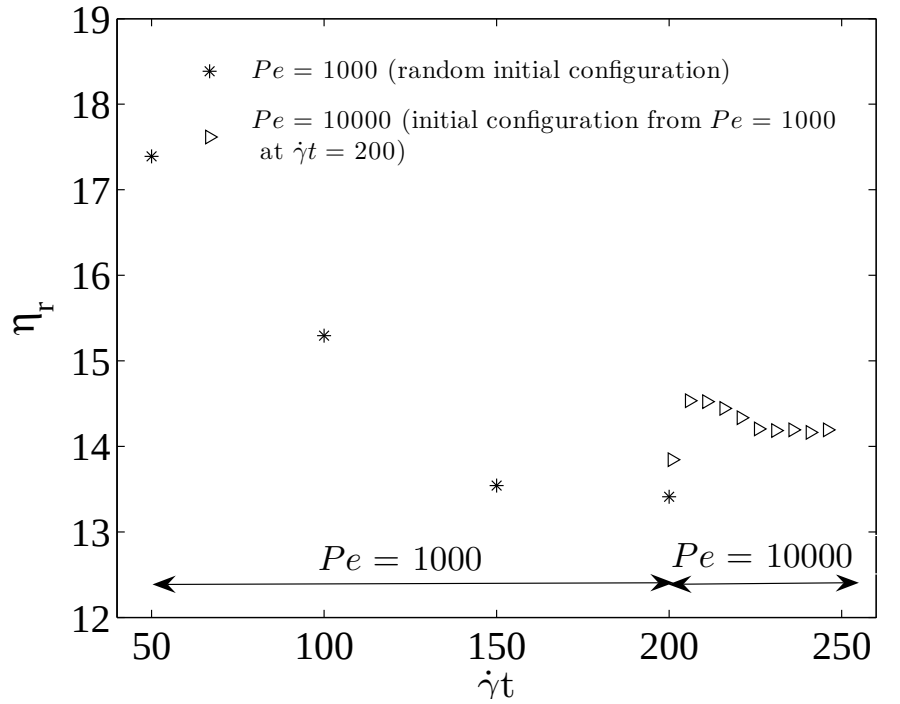

Figure 3.3: Response of a suspension of $\phi = 0.55$ to a step change (a) from $Pe = 1000$ to $Pe = 1$, and (b) from $Pe = 1000$ to $Pe = 10^4$.

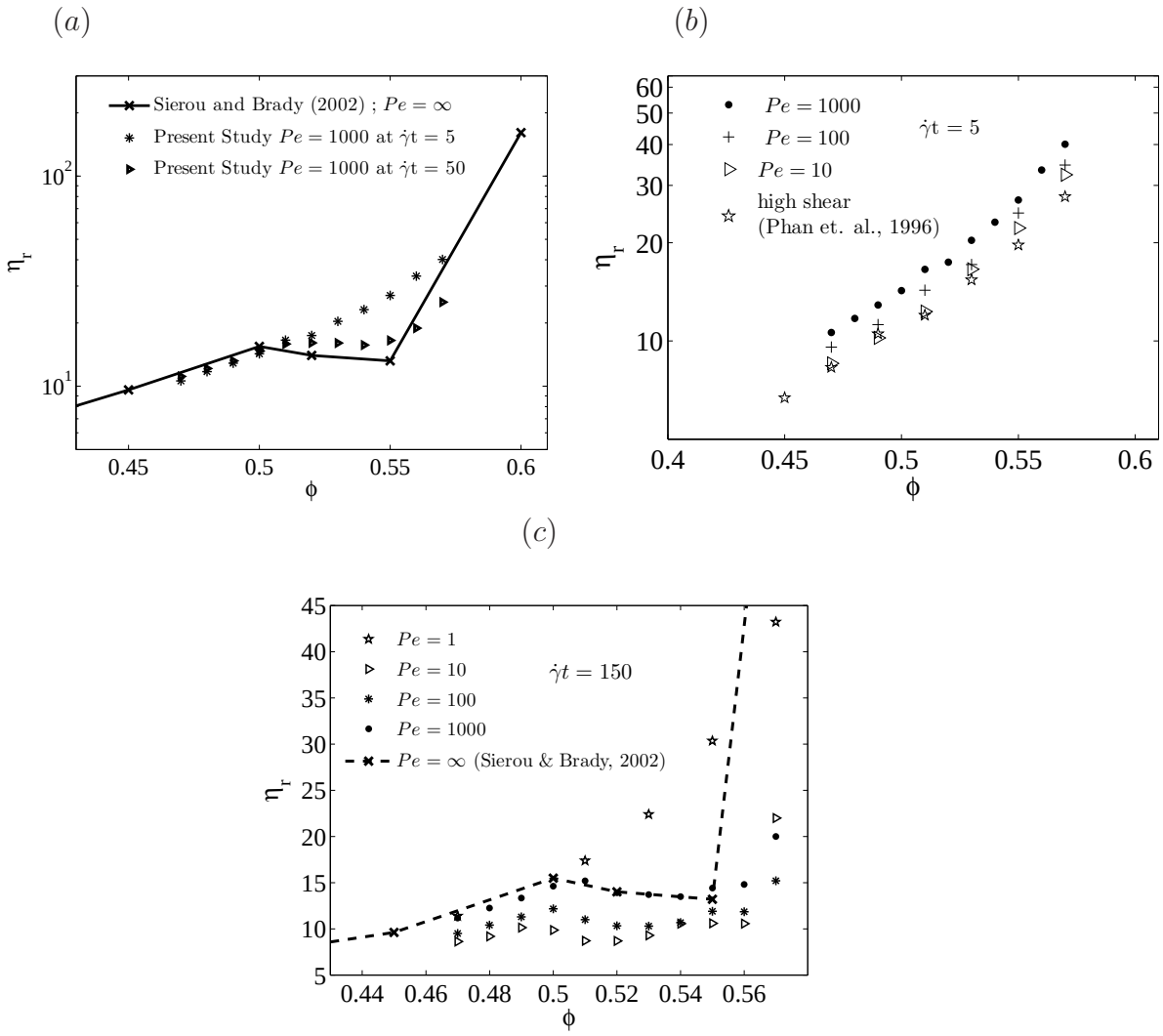

Figure 3.4: (a) η_r vs. ϕ at $Pe = \infty$ from Sierou & Brady (2002), and from this study at $Pe = 1000$ at $\dot{\gamma}t = 5$ and at $\dot{\gamma}t = 50$; (b) $\eta_r(\dot{\gamma}t = 5)$ vs. ϕ for $Pe = 1$, $Pe = 10$, $Pe = 100$ and $Pe = 1000$ compared with experimental study by Phan *et al.* (1996). (c) η_r vs. ϕ at $\dot{\gamma}t = 150$ at $Pe = 1$, $Pe = 10$, $Pe = 100$ and $Pe = 1000$ compared with ASD at $Pe = \infty$ by Sierou & Brady (2002).

3.4 Pair distribution function

The pair distribution function of sheared colloidal suspensions at large ϕ has been studied over the range of Pe described above. To simplify the discussion, we limit consideration to $Pe = 1$ and $Pe = 1000$. This provides a case which shows no thixotropic behavior at $Pe = 1$, while at $Pe = 1000$ thixotropy is observed for $\phi > 0.50$.

The pair distribution function can be written as

$$g(\mathbf{r}) = \frac{P_{1|1}(\mathbf{r})}{\bar{n}}, \tag{3.4}$$

where $\bar{n}$ is the average particle number density and $P_{1|1}(\mathbf{r})$ is the conditional probability of finding a particle at position $\mathbf{r}$ given a particle centered at the origin. Parsi & Gadala-Maria [25] by experiment and Phung *et al.* [50] by simulation studied the effect of flow at large Péclet number upon the pair distribution function. Their studies showed that near contact there is an accumulation of the pair probability in the compressional quadrant and comparatively smaller values in the extensional quadrant. Brady & Morris [17] have analyzed this situation for dilute suspensions in plane strain to show the accumulation is of a boundary-layer structure at distances of aPe^{-1} from particle contact, and Wilson [51] has considered a model of roughness to develop a more complete solution which illustrates the wake associated with the boundary layer. Parsi & Gadala-Maria [25] found that when the flow is reversed, after a specific response time, the material inverts structure by interchanging the compressional and extensional quadrants. Morris & Katyal [24] have examined the pair correlation asymmetry as a function of ϕ and Pe using highly time-resolved Stokesian Dynamics simulations to resolve the boundary-layer correlation and quantify the contact value of

the pair distribution function over the range of $0.2 \leq \phi \leq 0.585$; these authors did not observe ordering described here, perhaps owing to simulation of smaller total strains for the elevated ϕ where the ordering occurs. Here, we focus on $0.47 \leq \phi \leq 0.57$ at $Pe = 1$ and $Pe = 1000$, and determine the pair distribution function using ASD to compute the particle motions. The predicted particle positions are sampled at uniformly spaced intervals of 0.1 strain.

The pair distribution function, $g(\mathbf{r})$, is evaluated on a grid in $\mathbf{r} = (r, \theta, \psi)$ pair space where $2 \leq r$ is the center separation of the equal sized spheres, $0 \leq \theta < 2\pi$ is the polar angle measured counter-clockwise from the positive x-axis (flow direction), and $0 \leq \psi < \pi$ defines the azimuthal angle measured from the positive z-axis (vorticity direction). The simple shear flow is given by $\mathbf{u} = (\dot{\gamma}y, 0, 0)$, so that the x-y plane is the plane of shear, and y-z is the plane perpendicular to the mean flow. Histograms of occurrence $M(r, \theta, \psi, \Omega)$ of the pair separation vectors obtained from dynamic simulations are generated. The value of the pair distribution function can be determined as

$$g(r, \theta, \psi) = \lim_{\Omega \to \infty} \frac{M(r, \theta, \psi, \Omega)}{\bar{n}\Omega\Delta V}, \tag{3.5}$$

where Ω defines the number of sampling events and $\Delta V = r^2 \Delta r \sin\psi \Delta\psi \Delta\theta$ is the volume of the bin of which (r, θ, ψ) is the midpoint. In practice, the result is taken for sufficiently large Ω that the result becomes independent of the number of samples. The discretization mesh is chosen such that the bins are separated by a distance of $\Delta r = 0.025$ particle radius, while $\Delta\theta = 3.6^\circ$ and $\Delta\psi = 9^\circ$.

Figure 3.5 shows that, with bin size $\Delta r = 0.025$, the ASD algorithm used here results in accurate $g(r)$ under equilibrium conditions based on good agreement with Monte-Carlo simulations, and matching to the $g(r)$ obtained from Percus-Yevick

theory [52] with Verlet-Weis correction to within 1%. Note that $\Delta r = 0.025$ is a relatively large bin in the near-contact region for sheared suspensions: using conventional Stokesian Dynamics simulation, Morris & Katyal [24] have shown that capturing the contact value of $g(\mathbf{r})$ in sheared suspensions requires very small near-contact values of Δr, and the value of g near contact found here will be smaller than the more accurate values shown in that work (figure 3.5).

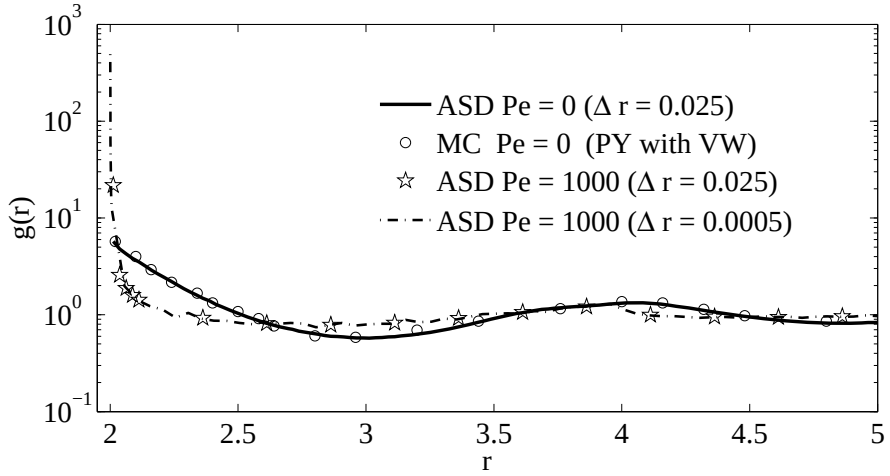

Figure 3.5: Pair distribution function at $\phi = 0.49$. The equilibrium $g(r)$ determined using ASD ($\Delta r = 0.025$) is compared with that obtained from Monte Carlo simulation (Hansen & Mcdonald, 1986) and with $g(r)$ at $Pe = 1000$ for $\Delta r = 0.025$ (the bin size in the present work) and $\Delta r = 0.0005$.

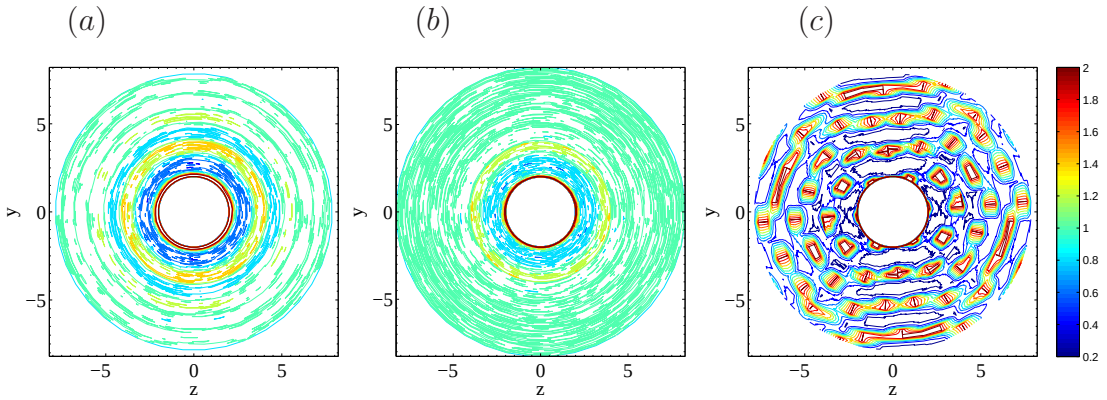

Figure 3.6: Pair distribution function on the y-z plane averaged over $0 \leq \dot{\gamma}t \leq 100$ at (a) $Pe = 1$ for $\phi = 0.55$, (b) at $Pe = 1000$ for $\phi = 0.47$, and (c) at $Pe = 1000$ for $\phi = 0.55$.

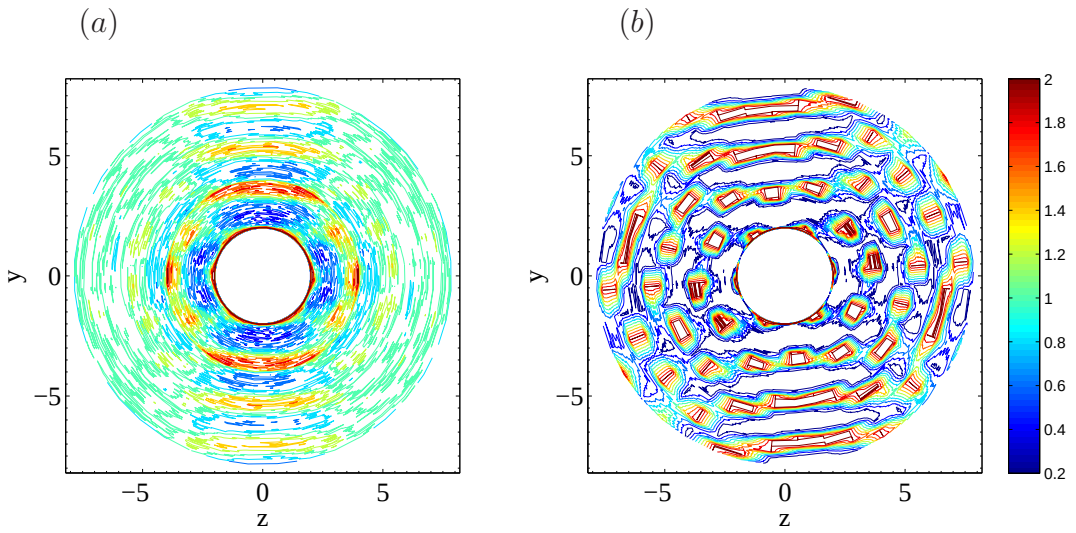

Figure 3.7: Pair distribution function on the y-z plane for $\phi = 0.55$ at $Pe = 1000$ (a) averaged over $5 \leq \dot{\gamma}t \leq 11$, and (b) averaged over $80 \leq \dot{\gamma}t \leq 100$.

In figure 3.6a, we plot $g(\mathbf{r})$ for $\phi = 0.55$ at $Pe = 1$ in the y-z plane, i.e. showing a slice of this function defined over all pair space. Averaging is over the first 100 strains in all of figure 3.6. We plot $g(\mathbf{r})$ in the y-z plane for $\phi = 0.47$ and $\phi = 0.55$ at $Pe = 1000$ in figure 3.6b and 3.6c, respectively, with all $g \geq 2$ of the same shading to obtain a more informative projection. These figures clearly show that, at $Pe = 1000$, the microstructure changes when ϕ is raised from $\phi = 0.47$ to $\phi = 0.55$ and indicate hexagonal ordering for $\phi = 0.55$ with a tilt of 6° relative to planes of fixed y. At $Pe = 1$, only slight ordering of this sort is observed even at $\phi = 0.55$.

The thixotropic behavior of the system at $Pe = 1000$ for $\phi > 0.50$ discussed in the previous section is closely coupled to the microstructural ordering. The fall in the relative viscosity η_r with time under shear is associated with ordering of the microstructure, implying that the order is not abruptly formed but instead becomes more pronounced with time under shear. In figure 3.7, we plot $g(\mathbf{r})$ for $\phi = 0.55$ at $Pe = 1000$ in the y-z plane. The results are averaged over two ranges: $5 \leq \dot{\gamma}t \leq 11$ in figure 3.7a and $80 \leq \dot{\gamma}t \leq 100$ in figure 3.7b, where the ordering is clearly more

pronounced. Owing to the gradual ordering of the microstructure in these thixotropic systems, the second normal stress difference $N_2 = < \Sigma_{yy} > - < \Sigma_{zz} >$, which has large negative values at early time falls close to zero as the system evolves, for example, at $\phi = 0.55$ and $Pe = 1000$, $N_2 = \dot{\gamma}\eta \approx -15$ at early time and falls to -1.5 over the first 45 strain.

The value of $g(\mathbf{r})$ in the bin adjacent to contact will be called the contact value, or $g(2)$. In figure 3.8, $g(2)$ is plotted in the x-y plane for $\phi = 0.47$ to $\phi = 0.57$ at $Pe = 1$ and $Pe = 1000$, with averaging over $0 \leq \dot{\gamma}t \leq 100$. At $Pe = 1$, $g(2)$ increases monotonically as ϕ is raised from $\phi = 0.47$ to $\phi = 0.57$ (figure 3.8a). At $Pe = 1000$, $g(2)$ near the flow direction, $\theta \approx 0^\circ$ and $\theta \approx 180^\circ$, grows as we go from $\phi = 0.51$ to $\phi = 0.55$ and 0.57, while there is surprising fall in $g(2)$ between $\theta = 20^\circ$ and $\theta = 160^\circ$ (figure 3.8b). This is reflective of the increasing tendency of particles to flow in chains in the x-direction.

In figure 3.9, we plot $g(2)$ in the flow-normal or y-z plane ($\theta = 90^\circ$). At $Pe = 1$, the deviation of $g(2)$ from its mean value remains small for all ϕ studied (figure 3.9a). Note that the mean of $g(2)$ increases with ϕ; the increase of pair correlation at contact with ϕ is well-known at equilibrium and this effect is magnified by shear flow. At $Pe = 1000$, the deviation of $g(2)$ from its mean value is small for $\phi = 0.47$ and $\phi = 0.51$. At $\phi = 0.53$, $g(2)$ develops clear minima at $\psi \approx 30^\circ$, $\psi \approx 90^\circ$ and $\psi \approx 150^\circ$ and maxima at $\psi \approx 60^\circ$, $\psi \approx 120^\circ$ and $\psi \approx 180^\circ$ (figure 3.9b). This evidence of hexagonal packing in the y-z plane becomes more pronounced for $\phi = 0.55$ and $\phi = 0.57$. Note that the changes in $g(2)$ at $Pe = 1000$ seen in both the x-y and y-z planes for $\phi > 0.50$ are not seen at $Pe = 1$ where the suspension remains disordered.

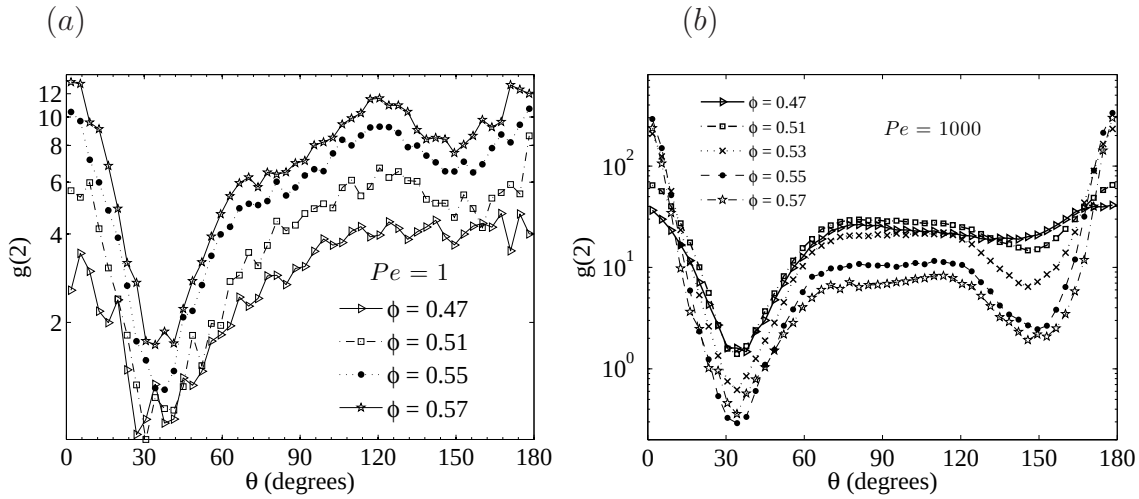

Figure 3.8: The contact value of the pair distribution function in the x-y plane averaged over $0 \leq \dot{\gamma}t \leq 100$ (a) at $Pe = 1$ for different ϕ; (b) at $Pe = 1000$ for different ϕ.

3.4.1 The order parameter C_6

We introduce an order parameter to provide a quantitative measure of hexagonal packing in the y-z plane. It is similar in spirit to the Q_6 parameter [53], and defined as

$$C_6 = \frac{\int_0^{2\pi} g(2, \pi/2, \psi) \cos[6(\psi - \delta)] d\psi}{\int_0^{2\pi} g(2, \pi/2, \psi) d\psi}, \tag{3.6}$$

where δ is a phase shift, which accounts for the tilt in the hexagonal packing relative to lines of constant y; the appropriate value for a specific Pe and ϕ is determined by maximizing C_6 as a function of δ. The order parameter for isotropic structure is $C_6 = 0$, and higher values indicate pronounced hexagonal order in the chosen plane. Figure 3.10 presents C_6 together with η_r for $Pe = 1$ and 1000 for the range of ϕ studied. At $Pe = 1$, C_6 remains close to zero for $\phi \leq 0.51$, while at higher values of ϕ, it increases slightly indicating the presence of a low level of hexagonally-ordered structure. At $Pe = 1000$, $C_6 \approx 0$ for $\phi = 0.47$, and increases sharply for $\phi > 0.51$. The increase in C_6 is seen to coincide with the drop in η_r for the thixotropic $Pe = 1000$

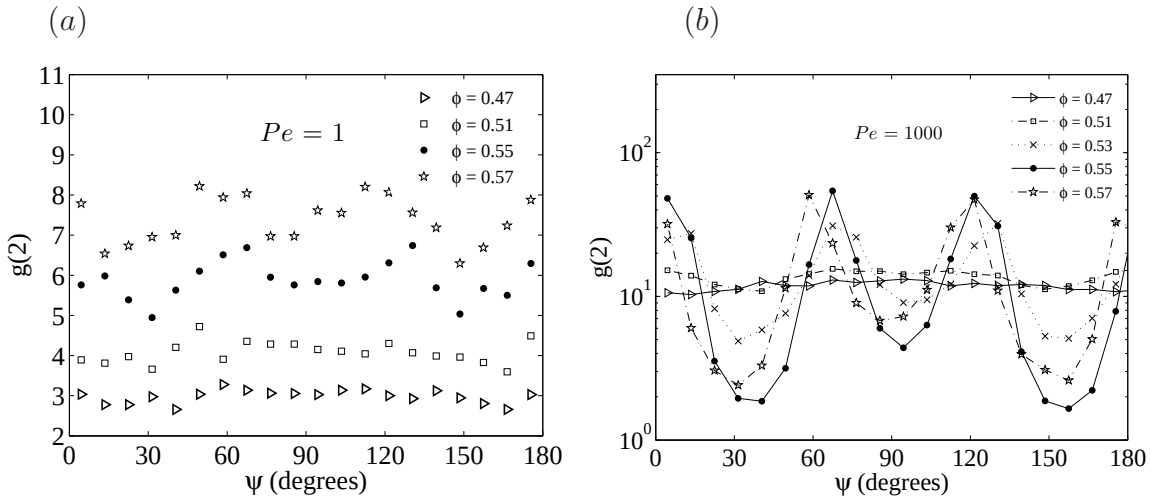

Figure 3.9: The contact value of the pair distribution function in the y-z plane averaged over $0 \leq \dot{\gamma}t \leq 100$ (a) at $Pe = 1$ for different ϕ; (b) at $Pe = 1000$ for different ϕ.

condition.

Suspensions showing thixotropy also grow more ordered with time under shear. A representative case, $\phi = 0.55$ at $Pe = 1000$, is probed. Figure 3.11a shows that, for $g(2)$ in the x-y plane, the structure averaged over $100 \leq \dot{\gamma}t \leq 150$ has higher values of $g(2)$ near the flow direction, $\theta = 0°$ and $\theta = 180°$, and lower values between $\theta = 20°$ and $\theta = 160°$ than when averaged over $5 \leq \dot{\gamma}t \leq 50$. Figure 3.11b shows that, for $g(2)$ in the y-z plane, the oscillatory behavior characteristic of hexagonal ordering is more pronounced for the structure averaged over $100 \leq \dot{\gamma}t \leq 150$ ($C_6 = 30.7$) than that over $5 \leq \dot{\gamma}t \leq 50$ ($C_6 = 23.7$). Note that in the later time window, certain angles are found to have $g(2) = 0$, in the x-y plane near $\theta = 30^o$ and in the y-z plane near $\psi = 150^o$, for example. These positions between the points of hexagonal arrangement of particles around the reference particle are never occupied by a second particle over the operative time window.

The phase shift δ which provides the extent of tilt in the hexagonal packing is strongly dependent on the volume fraction ϕ. Table 3.2 shows values of the phase shift δ for different ϕ at $Pe = 1$ and $Pe = 1000$. It is observed that δ increases as ϕ

ϕ	δ (Pe = 1000)	δ ($Pe = 1$)
0.50	3°	3°
0.51	4°	5°
0.53	8°	11°
0.55	6°	3°
0.57	0°	−3°

Table 3.2: The phase shift δ, which accounts for the tilt in the hexagonal packing and provides the maximized value of C_6, tabulated for different ϕ at $Pe = 1$ and $Pe = 1000$ (error-bar $\pm 1°$).

goes from $\phi = 0.51$ to $\phi = 0.53$ while it decreases as ϕ is increased further as shown in Table 3.2. The rise and fall behavior for δ is more pronounced at $Pe = 1$ as compared to $Pe = 1000$.

In the representative case of $\phi = 0.55$ at $Pe = 1000$ described in the prior paragraph, the value $\delta \approx 6°$ is found for structures averaged over the intervals $100 \leq \dot{\gamma}t \leq 150$, $200 \leq \dot{\gamma}t \leq 250$ and $300 \leq \dot{\gamma}t \leq 350$. The tilt in the hexagonal packing is time-independent once the structure is established.

The pair distribution function of thixotropic suspensions is investigated for a step change in Pe as described previously with figure 3.3a showing the variation of viscosity. For $\phi = 0.55$, after a strain of 50 at $Pe = 1000$, the suspension is subjected to a step change to $Pe = 1$. For the structure averaged over $5 \leq \dot{\gamma}t \leq 15$ and $40 \leq \dot{\gamma}t \leq 50$ at $Pe = 1000$, C_6 rises from 5.4 to 27.8. At $\dot{\gamma}t = 50$, when the system is subjected to $Pe = 1$, C_6 drops to $C_6 = 3.6$ for $55 \leq \dot{\gamma}t \leq 60$ and $C_6 = 1.7$ for $75 \leq \dot{\gamma}t \leq 80$. Thus, the shear induced structure at $Pe = 1000$ 'melts away' at $Pe = 1$.

The ordering transition occurs in the range $1 < Pe < 10$, and to examine this more closely, $Pe = 2$ has been studied. Simulations performed at $Pe = 2$ for $\phi = 0.55$ with random initial configuration remain disordered over extended strain, and η_r is

time-independent. A step change following 50 strain at $Pe = 10$ to $Pe = 2$ was applied to a suspension of $\phi = 0.55$. Unlike the behavior described for an ordered suspension subjected to $Pe = 1$, the suspension in this case remains in the ordered state, and η_r does not increase. The ordered state may be the 'preferred' state, but if so is reached only after large strain of $> O(100)$; we are thus led to believe that $Pe = 2$ is close to the transition value of Pe for this ϕ.

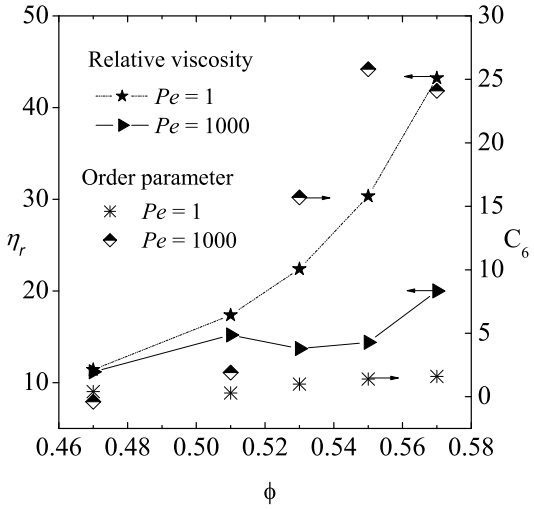

Figure 3.10: Hexagonal order parameter, C_6 averaged over $0 \leq \dot{\gamma}t \leq 100$ (right axis) and steady relative viscosities (left axis) for different ϕ at $Pe = 1$ and at $Pe = 1000$.

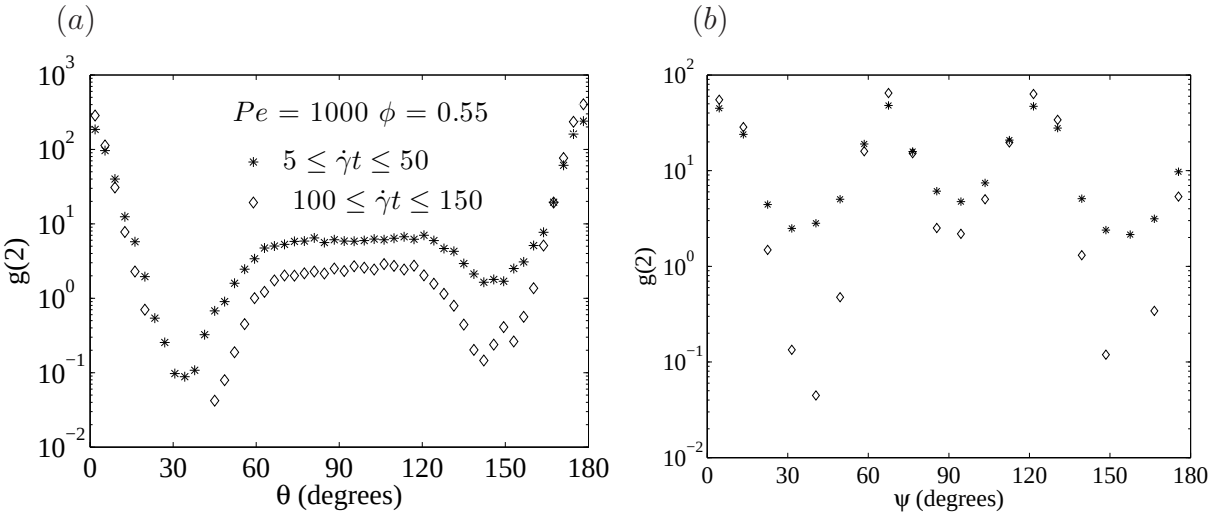

Figure 3.11: The contact value of the pair distribution function at $Pe = 1000$ for $\phi = 0.55$ averaged over $5 \leq \dot{\gamma}t \leq 50$ and $100 \leq \dot{\gamma}t \leq 150$ on (a) the x-y plane; (b) the y-z plane. The legend in (a) applies also to (b). The discontinuity in the curves for $100 \leq \dot{\gamma}t \leq 150$ in (a) near 30° and in (b) near 150° implies $g(2) = 0$.

3.5 Dynamic structure factor

In this section, we study the microstructure of sheared suspensions using the dynamic structure factor approach, which comes from the theory of dynamic light scattering [54]. This approach was applied to the study of particulate diffusion in dilute colloidal suspensions by Rallison & Hinch [55] and implemented for sheared suspensions to study self diffusion by Morris & Brady [56] and collective diffusion by Leshansky *et al.* [57]. Here, we use the approach to explore the effects on structure and diffusion of shearing flow on concentrated Brownian suspension, as demonstrated by Leshansky & Brady [48].

The dynamic structure factor is a two-point time-autocorrelation function of the local particle density. The local particle number density at position $\mathbf{r}$ can be stated as

$$n(\mathbf{r},t) = \sum_{\alpha=1}^{N} \delta(\mathbf{r} - \mathbf{r}_\alpha(t)). \tag{3.7}$$

The spatial Fourier transform of the particle number density is

$$\hat{n}(\mathbf{k},t) = \int \exp(i\mathbf{k}\cdot\mathbf{r}) \sum_{\alpha=1}^{N} \delta(\mathbf{r} - \mathbf{r}_\alpha(t)) d\mathbf{r} = \sum_{\alpha=1}^{N} \exp(i\mathbf{k}\cdot\mathbf{r}_\alpha(t)). \tag{3.8}$$

The autocorrelation in the number density is

$$F(\mathbf{k},t) = \frac{1}{N} < \hat{n}(\mathbf{k},t)\hat{n}^*(\mathbf{k},0) >= \frac{1}{N}\langle \sum_{\alpha,\beta}^{N} \exp[i\mathbf{k}\cdot(\mathbf{r}_\alpha(t) - \mathbf{r}_\beta(0))]\rangle, \tag{3.9}$$

where $< \cdot >$ implies an ensemble average and $\hat{n}^*$ is the complex conjugate of $\hat{n}$. The

function $F(\mathbf{k},t)$ at $t=0$ yields the static structure factor $S(\mathbf{k})$:

$$F(\mathbf{k},t=0) \equiv S(\mathbf{k}) = \frac{1}{N} < \hat{n}(\mathbf{k},0)\hat{n}^*(\mathbf{k},0) >= \frac{1}{N}\langle \sum_{\alpha,\beta}^{N} \exp[i\mathbf{k}\cdot(\mathbf{r}_\alpha(0)-\mathbf{r}_\beta(0))]\rangle. \tag{3.10}$$

The static structure factor is related to the pair distribution function through a three-dimensional Fourier transform [1] as

$$S(\mathbf{k}) = 1 + \bar{n}\int \exp(i\mathbf{k}\cdot\mathbf{r})g(\mathbf{r})d\mathbf{r}, \tag{3.11}$$

where $\bar{n} = N/V$ is the average particle number density. The wave-vector $\mathbf{k}$ is chosen to fit the simulation box and can be described as $\mathbf{k} = (k_x, k_y, k_z)$ where L is the simulation box length and k_x, k_y, k_z are integer multiples of $\frac{2\pi}{L}$; L is related to the solid fraction by $L = \left(4\pi a^3 N/3\phi\right)^{1/3}$. $F(\mathbf{k},t)$ measures the density fluctuations on the length scale $l = 2\pi/|\mathbf{k}|$. When $|\mathbf{k}| = k$ is small, we are probing long length scales: $k \to 0$ represents hydrodynamic modes associated with the idea that on this scale conservation principles may be simply applied.

Both $F(\mathbf{k}, t \neq 0)$ and $S(\mathbf{k}) \equiv F(\mathbf{k}, t = 0)$ can be obtained from equation (3.9) and equation (3.10) using the knowledge of particle positions as a function of time from ASD simulations. We focus again on $0.47 \leq \phi \leq 0.57$ at $Pe = 1000$ where pronounced hexagonal ordering occurs for $\phi > 0.50$ and at $Pe = 1$ where the ordering is not seen.

The wave-vector in the velocity-gradient (y) direction is given by $\mathbf{k} = (0, k_y, 0)$, while that in the vorticity (z) direction is given by $\mathbf{k} = (0, 0, k_z)$. The dependences of $S(\mathbf{k})$ on k_y and k_z at $Pe = 1$ for $\phi = 0.47$ and $\phi = 0.55$ averaged over $0 \leq \dot{\gamma}t \leq 100$ are shown in figures 3.12a and 3.12b. Figures 3.13a and 3.13b show the projection of the

static structure factor for $\phi = 0.47$ and $\phi = 0.55$ at $Pe = 1000$ (again averaged over $0 \leq \dot{\gamma}t \leq 100$) on the y and z directions. There are prominent peaks with respect to both k_y and k_z. The first peak corresponds to a length scale $l = (2\pi/k) \approx 2$, i.e. the particle diameter which is the approximate center separation in these dense suspensions.

At $Pe = 1$, both $S(k_y)$ and $S(k_z)$ increase in their first peak as ϕ varies from $\phi = 0.47$ to $\phi = 0.55$. This is attributed to the increase in $g(2)$ with ϕ as described in section 4 (figures 3.8a and 3.9a). At $\phi = 0.55$, the first peak value in $S(k_y)$ is about twice that of $S(k_z)$, showing evidence of structural anisotropy.

At $Pe = 1000$, $S(k_y)$ undergoes an extraordinary increase in the first peak from $\phi = 0.47$ to $\phi = 0.55$ as seen in figure 3.13a. This dramatic increase is mainly attributed to the formation of chain-like structures in the x-y plane for $\phi = 0.55$. The projection of $S(k_z)$ shows that between $\phi = 0.47$ and $\phi = 0.55$, the second peak value grows beyond the first peak. This may be explained by noting that the hexagonal packing in the y-z plane has crests in $g(2)$ at $\psi \approx 60°$, $\psi \approx 120°$ and $\psi \approx 180°$ and symmetry through the origin (figure 3.9b). The crests at $\psi \approx 60°$ and $\psi \approx 120°$, are approximately at $z = 2\cos 60° = 1$, which is roughly the offset distance in z of four of the six particles hexagonally arranged around a reference particle. This second peak in $S(k_z)$ becomes prominent as seen in figure 3.13b. Xue & Grest [58] and Leshansky & Brady [48] observed similar shear-induced structure.

It is of interest to consider the observed ordering in relation to the freezing criterion stated by Hansen & Verlet [59], namely that phase transition for the equilibrium hard-sphere system occurs when the value of the first peak of $S(k) > 2.85$. In the present work, shear induced structural anisotropy makes $S(k)$ direction dependent, and this criterion is apparently not directly applicable. As an example, for $\phi = 0.47$, $S(k_z)$ fails to meet the Verlet-Hansen criteria at both $Pe = 1$ and $Pe = 1000$, which is in

agreement with the disordered state at these conditions; however, $S(k_y) > 3$ (and the average of $S(k_y)$ and $S(k_z)$ surpasses 2.85) for $Pe = 1$ and yet the system remains disordered.

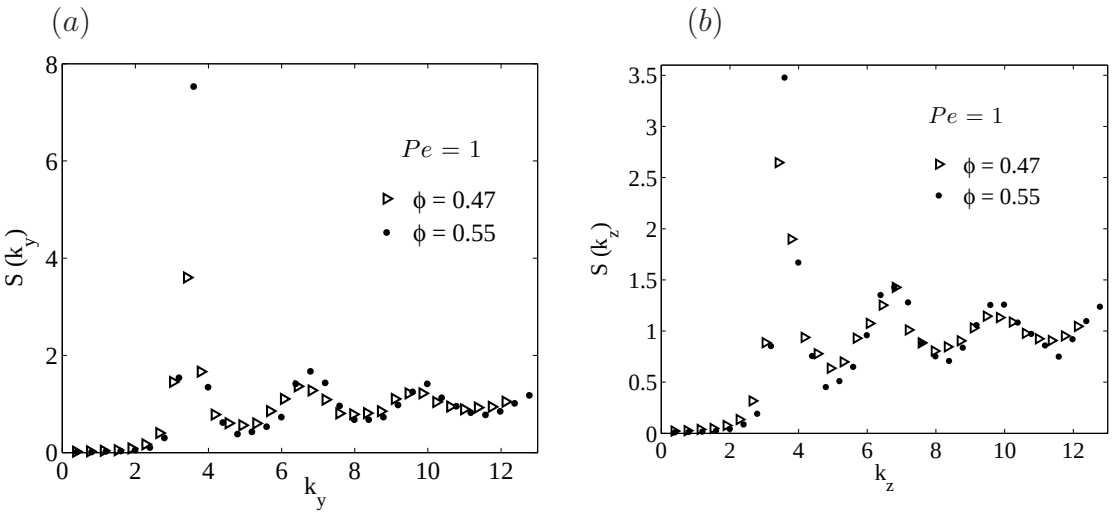

Figure 3.12: Projection of the static structure factor for $\phi = 0.47$ and $\phi = 0.55$ at $Pe = 1$ averaged over $0 \leq \dot{\gamma}t \leq 100$ on (a) the velocity gradient axis; (b) the vorticity axis.

Finally, we probe shear induced long-time self-diffusivity, which we determine both from the rate of change of mean-square particle-displacement, and the decay of the self-dynamic structure factor. The structure factor, also called the 'self-intermediate scattering function,' is obtained by ignoring the cross-correlations in F from equation (3.9),

$$F_s(\mathbf{k}, t) = \frac{1}{N} < \hat{n}(\mathbf{k}, t)\hat{n}^*(\mathbf{k}, 0) >= \frac{1}{N}\langle \sum_{\alpha}^{N} \exp[i\mathbf{k} \cdot (\mathbf{r}_\alpha(t) - \mathbf{r}_\alpha(0))]\rangle. \tag{3.12}$$

One method for determination of the self diffusivity is based on the conservation equation for the particle number density. The conservation equation is stated as

$$\frac{\partial n}{\partial t} + \dot{\mathbf{\Gamma}} \cdot \mathbf{r} \cdot \nabla n + \mathbf{U} \cdot \nabla n = -\nabla \cdot \mathbf{j}, \tag{3.13}$$

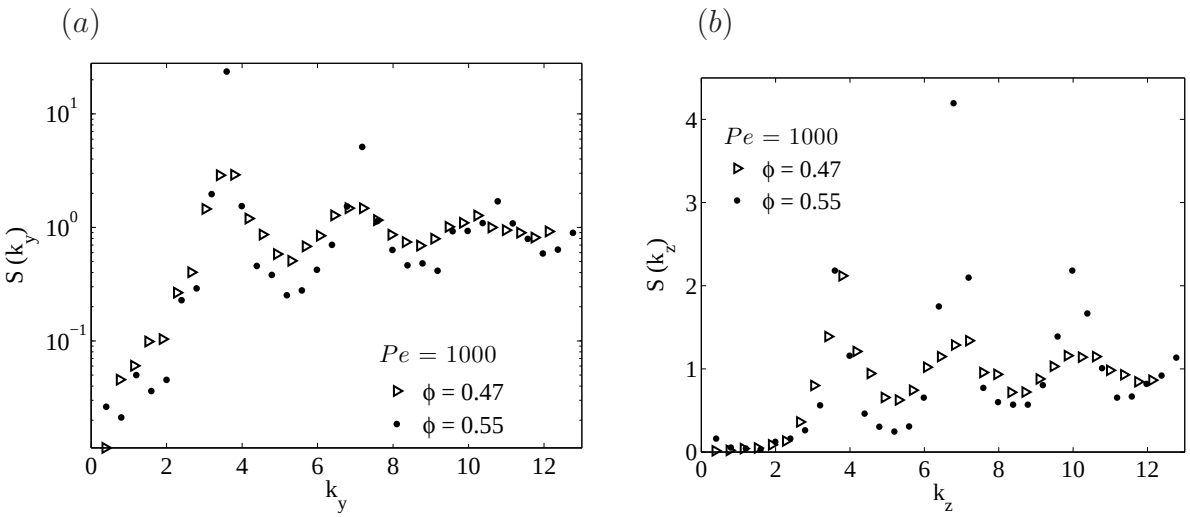

Figure 3.13: Projection of the static structure factor for $\phi = 0.47$ and $\phi = 0.55$ at $Pe = 1000$ averaged over $0 \leq \dot{\gamma}t \leq 100$ on (a) the velocity gradient axis (note the logarithmic scale in this case); (b) the vorticity axis.

where $\mathbf{U}$ is the bulk average velocity measured at an arbitrary field point, $\dot{\mathbf{\Gamma}}$ is the velocity gradient tensor and $\mathbf{j}$ is the diffusive flux of the particles. Taking the spatial Fourier transform of the above equation and multiplying both sides by $\hat{n}^*$ gives

$$\frac{\partial F_s}{\partial t} - \mathbf{k} \cdot \dot{\mathbf{\Gamma}} \cdot \nabla_k F_s - i\mathbf{k}\mathbf{U}F_s = -\mathbf{k} \cdot \hat{D}^s \cdot \mathbf{k}F_s. \tag{3.14}$$

For $\mathbf{k} \perp (\dot{\mathbf{\Gamma}} \cdot \mathbf{x})$, the convective terms in equation (3.14), i.e. the last two left-hand side terms, can be neglected and the self-diffusivity can be expressed as

$$-\frac{\dot{F}_s}{k^2 F_s} = \tilde{\mathbf{k}} \cdot \hat{\mathbf{D}}^s_\perp \cdot \tilde{\mathbf{k}}. \tag{3.15}$$

Thus, the slope of $-k^{-2} \ln F_s(k,t)$ plotted as a function of time yields the self-diffusivity component (normalized by $\dot{\gamma}a^2$) in the direction of the corresponding wave-vector. Figure 3.14 describes decay of F_s at $Pe = 1000$ and $\phi = 0.47$ for the three smallest values of wave-vectors $\mathbf{k}$ in the velocity gradient ($\mathbf{k} = k_y \hat{i_y} = \frac{2\pi m_y}{L} \hat{i_y}$ where

$m_y = 1, 2, 3$) and in the vorticity direction ($\mathbf{k} = k_z \hat{i_z} = \frac{2\pi m_z}{L} \hat{i_z}$ where $m_z = 1, 2, 3$). The plot of $-k^{-2} \ln F_s(k,t)$ vs. time gives the same slope ($D^s_{yy} = 0.057 \pm 0.002$) for all the three wave-vectors in the y-direction at long times ($\dot{\gamma} t > 2$), and similarly for the three wave-vectors in z ($D^s_{zz} = 0.042$). Thus, for a given ϕ and Pe, D^s_{yy} and D^s_{zz} are independent of $|\mathbf{k}|$ for values well below that associated with the first peak of S. For larger values of k, where we probe length scales comparable to the particle diameter or smaller, a linear dependence of $-k^{-2} \ln F_s(k,t)$ on time is not observed.

The method presented above to calculate long-time self diffusivities D^s_{yy} and D^s_{zz} is important from the perspective of light scattering experiments. The values of D^s_{yy} and D^s_{zz} obtained from this method match those obtained the rate of change of mean square displacement (MSD) in real space. In the further discussion, the more intuitively clear MSD approach is used to calculate D^s_{yy} and D^s_{zz}.

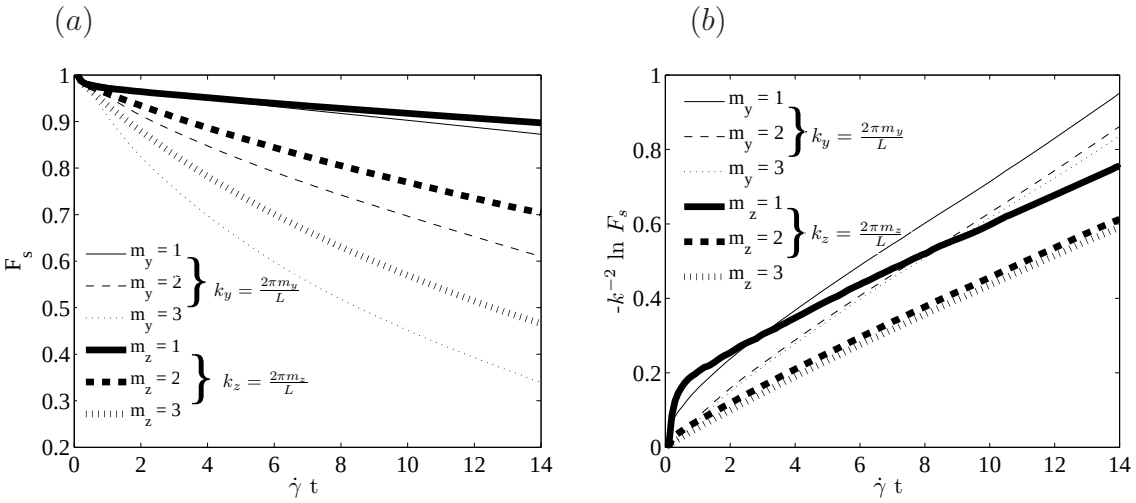

Figure 3.14: For $\phi = 0.47$ at Pe=1000 (a) $F_s(\mathbf{k}, t)$ vs. time and (b) re-plotting the same data as $-k^{-2} \ln F_s(k,t)$ vs. time.

(*a*) $Pe = 1$

ϕ	D^s_{yy}	D^s_{zz}
0.35	0.23	0.22
0.47	0.18	0.15
0.51	0.16	0.13
0.55	0.16	0.13
0.57	0.15	0.13

(*b*) $Pe = 1000$ and $Pe = \infty$

	I. $Pe = 1000$		II. $Pe = \infty$ (SB)		III. $Pe = \infty$(LB)	
ϕ	D^s_{yy}	D^s_{zz}	D^s_{yy}	D^s_{zz}	D^s_{yy}	D^s_{zz}
0.35	0.047	0.018	0.046	0.0185	0.0467	0.0173
0.40	—	—	0.062	0.029	0.0633	0.0285
0.45	—	—	0.0583	0.045	0.0624	0.0404
0.47	0.057	0.042	—	—	—	—
0.50	0.056	0.046	0.0580	0.0520	0.0572	0.0502
0.51	0.046/0.04	0.045/0.045	—	—	—	—
0.53	0.015/0.0086	0.018/0.011	—	—	—	—
0.55	0.0041/0.00059	0.0078/0.0029	—	—	0.0027	0.0051

Table 3.3: Average values of the long-time self-diffusivity components $D^s_{yy}/\dot{\gamma}a^2$ and $D^s_{zz}/\dot{\gamma}a^2$ for different ϕ at (a) $Pe = 1$; (b) at $Pe = 1000$ (set I) and at $Pe = \infty$ (set II from Sierou & Brady (2004) and set III from Leshansky & Brady (2005)). In set I, for $\phi > 0.50$ where ordering and thixotropy occur, D^s_{yy} and D^s_{zz} are represented in the form A/B, where A and B represent values averaged over $0 \leq \dot{\gamma}t \leq 100$ and over $100 \leq \dot{\gamma}t \leq 150$, respectively.

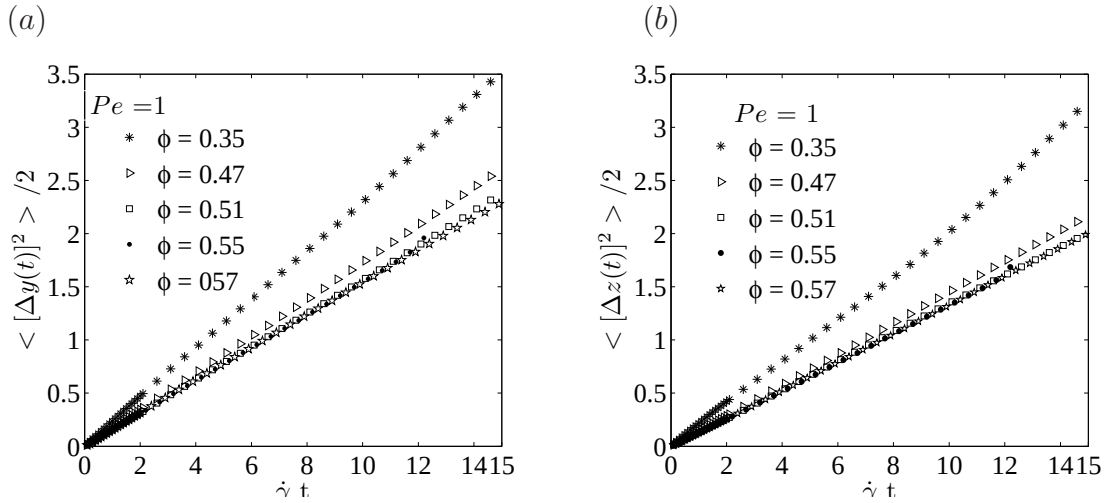

Figure 3.15: Mean-square displacement curve growth with time at $Pe = 1$ for different ϕ averaged over many initial times drawn from the first 100 strain, in (a) y-direction and (b) z-direction.

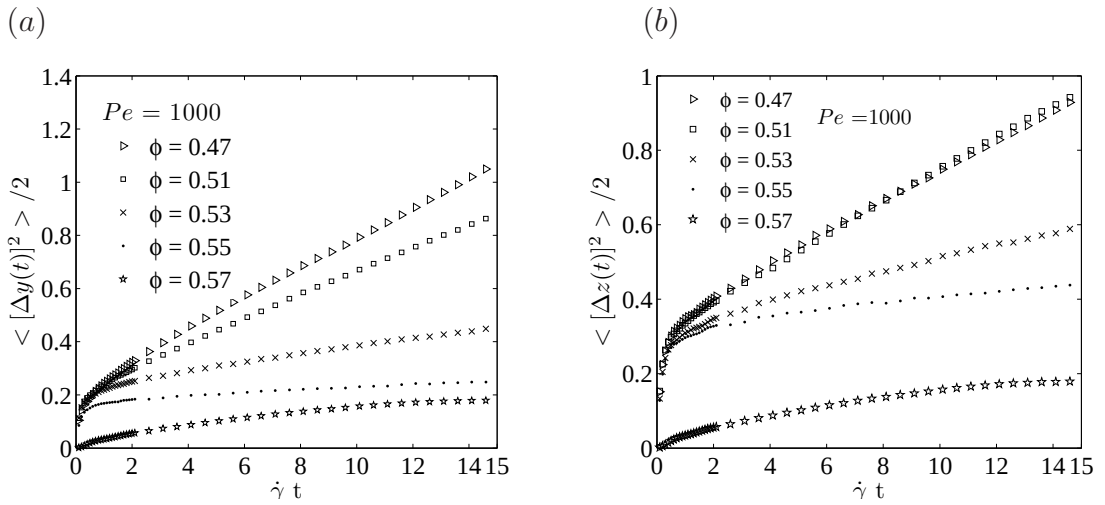

Figure 3.16: Mean-square displacement curve growth with time at $Pe = 1000$ for different ϕ averaged over many initial times drawn from the first 100 strain, in (a) y-direction and (b) z-direction.

Alternatively, the long-time self-diffusivity may be calculated based on the definitions

$$D^s_{yy} = \lim_{t\to\infty} \frac{1}{2}\frac{d}{dt} < [y(t) - y(0)]^2 >, \tag{3.16}$$

$$D^s_{zz} = \lim_{t\to\infty} \frac{1}{2}\frac{d}{dt} < [z(t) - z(0)]^2 > . \tag{3.17}$$

At very short time, non-linear temporal behavior is observed at $Pe = 1000$ (figure 3.16), as the particle motion is initially deterministic and diffusive motion has yet to be established, but at long time we find linear variation of the MSD, or a constant slope in either equation (3.16) or equation (3.17).

The values of D^s_{yy} and D^s_{zz} presented have been normalized by $\dot{\gamma}a^2$, because this is the natural scale of shear-induced self-diffusivity which is the dominant diffusive mechanism at large Pe [60]. At $Pe = 1$, the diffusivities normalized by by $\dot{\gamma}a^2$ or by the diffusion coefficient of an isolated Brownian particle, $D_0 = kT/6\pi\eta a$, will have the same value. On the other hand, the diffusivities normalized by D_0 can be simply computed by multiplying the reported values with normalization by $\dot{\gamma}a^2$ by Pe.

At $Pe = 1$ and $Pe = 1000$, for $0.47 \leq \phi \leq 0.57$, the values of D^s_{yy} and D^s_{zz} are obtained as slopes of mean-square displacement curves at longer times ($\dot{\gamma}t > 2$) where the function behaves linearly as seen in figures 3.15 and 3.16 and presented in Table 3.3. $< [\Delta y(t)]^2 >$ and $< [\Delta z(t)]^2 >$ are evaluated by taking many initial times from the first 100 strain and averaging to obtain a statistically meaningful value.

For non-colloidal suspensions, Sierou & Brady [61] have shown that both D^s_{yy} and D^s_{zz} increase with ϕ from $\phi = 0.10$ to $\phi = 0.40$, and there is a plateau region for D^s_{yy} between $\phi = 0.40$ to $\phi = 0.50$ while D^s_{zz} continues to rise up to $\phi = 0.50$. Our

$Pe = 1000$ results are consistent with these trends. In Table 3.3b (data set I), we see that at $Pe = 1000$ both D^s_{yy} and D^s_{zz} dramatically *decrease* as ϕ is raised from $\phi = 0.51$ to $\phi = 0.55$. The fall of the self-diffusivity components is related to the ordering into hexagonally arranged strings. This eliminates the velocity fluctuations driven by shear which are the crucial mechanism at large Pe [56, 17, 60]. For $\phi = 0.57$ at $Pe = 1000$, the mean-square displacement curves are not linear in both the y and z directions, but the instantaneous slopes of these curves for $\dot{\gamma}t > 5$ are comparable to that for $\phi = 0.55$. The ratio $\frac{D^s_{yy}}{D^s_{zz}} \gg 1$ up to $\phi = 0.40$ [61], becomes closer to 1 for $\phi = 0.40$ to $\phi = 0.50$, and falls below 1 for $\phi > 0.51$. The ratio continues to fall up to $\phi = 0.55$.

Foss & Brady [14] have shown that, at low Péclet numbers, the self-diffusivity decreases with increasing ϕ for $\phi < 0.45$. Consistent with their findings, Table 3.3a indicates that, at $Pe = 1$, both D^s_{yy} and D^s_{zz} decrease from $\phi = 0.35$ to $\phi = 0.47$. At low Péclet number, Brownian motion plays an important role and is hindered with increasing ϕ, while at high Péclet number shear forces dominate and shear induced diffusivity tends to increase with increasing ϕ. At $Pe = 1$, there is a plateau region for D^s_{yy} and D^s_{zz} for ϕ between $\phi = 0.51$ and $\phi = 0.57$. The ratio of $\frac{D^s_{yy}}{D^s_{zz}}$ at $Pe = 1$ remains close to unity for all ϕ.

Figure 3.17 shows the time variation of $< [\Delta y(t)]^2 >$ and $< [\Delta z(t)]^2 >$ at $Pe = 1000$ for $\phi = 0.55$. These quantities are evaluated by taking many initial times from the intervals $5 \leq \dot{\gamma}t \leq 50$ and $100 \leq \dot{\gamma}t \leq 150$, and averaging the resulting curves. The slopes of these plots show that average values of the self-diffusivity components over $100 \leq \dot{\gamma}t \leq 150$ are smaller ($D^s_{yy} = 5.9 \times 10^{-4}$, $D^s_{zz} = 2.9 \times 10^{-3}$) than that over $5 \leq \dot{\gamma}t \leq 50$ where $D^s_{yy} = 0.01$ and $D^s_{zz} = 0.014$. To quantitatively illustrate the change in the self-diffusion for ordering systems, we show the later time self-diffusivites (averaged over $100 \leq \dot{\gamma}t \leq 150$) alongside the early time diffusivites (averaged over

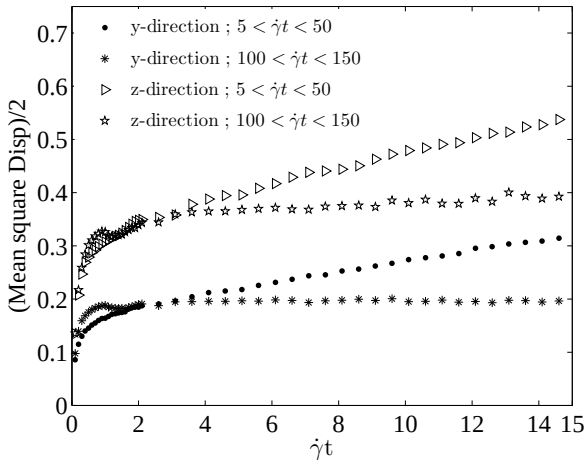

Figure 3.17: Mean square displacement as function of time at $Pe = 1000$ for $\phi = 0.55$ averaged over $5 \leq \dot{\gamma}t \leq 50$ and $100 \leq \dot{\gamma}t \leq 150$.

$0 \leq \dot{\gamma}t \leq 100$) in Table 3.3b (set I), with the later values being smaller. This is a further consequence of the ordering ($\approx$ hexagonal packing), which becomes more prominent as the system evolves.

3.6 Concluding remarks

The ordering behavior is summarized in figure 3.18. For the thixotropic systems with $\phi > 0.50$ and $Pe \geq 10$, ordering is observed with hexagonal packing in the y-z plane. The ordering of sheared suspensions for $\phi > 0.50$ at $Pe \geq 10$ is suggestive because it occurs in the same range of ϕ for which particle ordering in the form of a fluid-crystal coexistence occurs ($\phi_F = 0.494$) in the absence of flow, i.e. in Brownian suspensions at $Pe = 0$ (figure 3.18). However, ordering in this range of ϕ is not observed at all Péclet numbers, as we find it to be essentially absent at $Pe = 1$. For $1 < Pe < 10$, the ordering behavior beyond $\phi = 0.50$ depends on the state of initial configuration; thus these history-dependent structures may be termed as meta or bi-stable (figure 3.18).

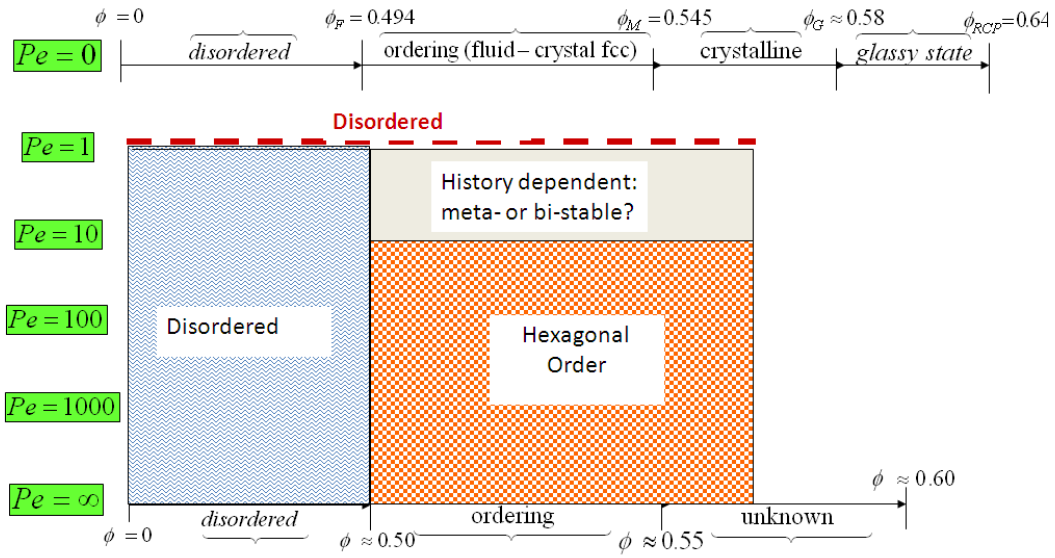

Figure 3.18: The ordering phase diagram in $Pe - \phi$ space.

The mechanistic basis for formation of an ordered state under shear has not been resolved by this work, but several points are clear. As noted just above, the process is driven by shear flow interactions: for sufficiently large Pe to obtain order, the time for ordering scales as $\dot{\gamma}^{-1}$, implying it is the imposed strain which is relevant. The onset of ordering appears to be a result of shear flow both breaking the spatial isotropy and introducing strong correlations in the disordered suspension [24, 62]. This correlation results in accumulation of particle pairs in the compressional quadrant and along the direction of flow; the latter are naturally seen as a possible source of "nucleation" for the observed hexagonal structure, but the ordering process remains unclear. It is a simpler matter to consider the stability of the observed ordered state. The hexagonal order is apparently stable provided the typical Brownian displacement over the time $\dot{\gamma}\Delta t \approx 1$ (unit strain) is sufficiently small; $\dot{\gamma}\Delta t \approx 1$ is the time for a string of particles to move one particle relative to a neighboring string in the gradient direction in a dense suspension. The disorder-order transition lies in the range $1 \leq Pe \leq 10$. Defining the Brownian displacement within a unit strain as $\Delta \underline{x}^B$, $(|(\Delta \underline{x}^B|/a)^2 \sim D_0^s(\phi)/(\dot{\gamma}a^2) =$

Pe_{eff}^{-1}, with D_0^s the short-time self-diffusivity (kT times the average mobility), and the effective Péclet number is defined $Pe_{\text{eff}} = \dot{\gamma}a^2/D_0^s = PeD_0/D_0^s(\phi)$. Taking the quiescent suspension diffusivity for scaling purposes, $D_0^s \sim 0.85(1 - \phi/\phi_{\max})$ and $\phi_{\max} = 0.64$, this yields for $\phi = 0.5$ and $Pe = 10$ a value of $Pe_{\text{eff}} \approx 50$, or $|\Delta \underline{\mathrm{x}}^B|/a \approx 0.14$. As expected, the displacement is a small fraction of the particle size. At $Pe = 2$, ordering was not found in runs of $\dot{\gamma}t = O(100)$, but an initially hexagonally ordered structure formed at higher Pe and $\phi = 0.55$ was found to remain stable. Here, $|\Delta \underline{\mathrm{x}}^B|/a \approx 0.24$. Brownian displacements at $Pe = 1$ are sufficient not only to prevent flow-induced ordering but also to cause sufficient perturbation of an ordered structure to allow shear-induced interactions to thoroughly disorder the structure. This is seen in the step change from an ordered state at $\phi = 0.55$ and $Pe = 1000$ to disordered and higher viscosity at $Pe = 1$.

We conclude that there is a pronounced tendency toward ordering for dispersions above $\phi \approx 0.5$, regardless of whether the dominant mode of motion is Brownian or shear. It is then natural to seek a fundamental driving force for the change in symmetry. In equilibrium, the formation of cubic crystalline structure at a bulk $\phi > 0.494$ results in a drop in the osmotic pressure relative to a fully disordered fluid arrangement. Shear flow breaks a symmetry, and thus the order seen is of a significantly different hexagonally packed string form, but results in reduced contact interaction and hence the rheology and particle normal stresses, including an isotropic portion which is the nonequilibrium analog of the osmotic pressure [31], are substantially below their values for the disordered state. In the equilibrium system, free energy minimization is the criterion for the equilibrium state, and it is thus plausible to view some measure of the stress response of the dispersion as a non-equilibrium surrogate for the free energy. The normal stress is the most natural candidate, and further study of this issue is warranted.

Chapter 4

Anisotropic suspension structure in pressure-driven flow

In this chapter, the microstructure obtained from the Accelerated Stokesian Dynamics simulation is compared with that obtained from experiments on pressure driven flow of Brownian suspensions through a micro-channel. The experiments are done by our collaborative group lead by Prof. James Gilchrist at Lehigh University.

4.1 Introduction

The shearing of suspensions with moderate to high particle volume fractions is known to generate normal stresses [63, 34, 21]. Brownian and non-Brownian systems ranging in volume fraction $0.3 < \phi < 0.5$ have been studied extensively through theory and simulations to identify and understand the effect of shear-induced microstructural anisotropies on the development of normal stresses [17, 14, 18]. Experimentally, detailed three dimensional (3D) particle-level information is necessary in order to identify local structure in sheared systems, but experiments to date lack the detail available via simulation. The main objective of this work is to obtain 3D measurement

A part of this chapter is published as *Direct investigation of anisotropic suspension structure in pressure-driven flow*, C. Gao, S. D. Kulkarni, J. F. Morris and J. F. Gilchrist, Phys. Rev. E **81**, 041403(2010)

of particle locations in the experiments of flow under shear and to enable direct microstructure comparison to the particle locations generated by the Accelerated Stokesian Dynamics simulation.

Stokesian Dynamics simulations predict a higher correlation of nearest neighbor interactions along the compressive axes of the flow in the $\mathbf{v} - \nabla\mathbf{v}$ projection of the pair distribution function, g($\mathbf{r}$) [24]. From an isotropic state, these dynamics develop quickly with the onset of flow [64]. While the normal stresses disappear upon cessation of flow in non-Brownian systems, the structural anisotropy is preserved [64, 65]. This anisotropy is destroyed upon reversal of the flow direction and reemerges oriented relative to the new flow direction [64]. This connection between local structural anisotropy and discontinuities observed upon flow reversal was confirmed by direct imaging of experiments exhibiting this fore-aft asymmetry [25] but these experiments did not provide detailed 3D structural information.

4.2 Experiments

Confocal laser scanning microscopy (CLSM) is used to obtain 3D particle-level anisotropy generated from shear in a pressure-driven flow. The suspensions are made of monosized $2a = 1.01\ \mu m$ diameter SiO_2 microspheres in 3:1 glycerol:water with 0.1 mM rhodamine-B to obtain a fluorescent index-matching solution. The bulk volume fraction is chosen as $\phi_{bulk} = 0.41$. To minimize electrostatic interactions, NaCl and NaOH are added to adjust the pH to 8.0 and the screening length to $\kappa^{-1} = 1.5$ nm. The suspension is passed through a $50\ mm \times 40\ \mu m \times 100\ \mu m$ microchannel (figure 4.1a) at a pressure drop as high as 1 atm using compressed nitrogen. The coordinates (x, y, and z) represent the ($\mathbf{v}$, $\nabla\mathbf{v}$, $\nabla \times \mathbf{v}$) directions. The region of interest (ROI) is located near the channel exit, at the center of the z direction ($20 \times 40 \times 20\ \mu m^3$)

as shown by the red box in figure 4.1a. The distances are made dimensionless with $H = 20\mu$m, which is half-height of the channel in the y direction. The nonlinear shear gradient as a result of pressure-driven flow induces significant suspension migration similar to [27, 29]. The final steady volume fraction profile far from the entrance is shown in figure 4.1b, ϕ is higher at the center and lower near the walls. Local viscosity depends on local volume fraction, therefore the velocity profile deviates from axial Poiseuille flow of a Newtonian fluid. Fully developed far from the entrance region, this generates a velocity profile across the y-direction at the center having a roughly 1 mm/s center velocity, plotted in figure 4.2. For comparison, axial Poiseuille flow of a Newtonian fluid, as calculated using the solution derived in Butera *et al.* [46], is also shown in figure 4.2. The local shear rate $\dot{\gamma}_y$, calculated from the local slope of the velocity profile over measured values within the nearest 6 μm of each point, is nearly linear and is used to define the local P*é*clet number, $Pe_y \equiv \frac{6\pi\eta_0\dot{\gamma}a^3}{kT}$, where η_0 is the fluid viscosity and kT is the thermal energy. The nonlinear velocity profile as a result of pressure-driven flow creates shear rate variation in the z-direction as well and it's effect is discussed later.

Dynamic confocal laser scanning microscopy (VTeye, Visitech Int.) allows single plane particle tracking for velocimetry to measure velocity profiles as well as measurement of particle concentration patterns in the plane transverse to the direction of flow [66, 67]; however its scanning speed is insufficient to track fast moving particles in 3D space and enable investigations of the microstructure. To eliminate transients, after flowing for 10 minutes we quickly stop the flow, similar to Dendukuri *et al.* [68], and scan the entire depth of the channel in the $\nabla\mathbf{v}$ direction within the region of interest (ROI). Use of compressed nitrogen gives a stable driving pressure and fast pressure release using a three-way valve near the channel entrance allows rapid arrest of suspension flow without flow reversal. In non-Brownian density-matched

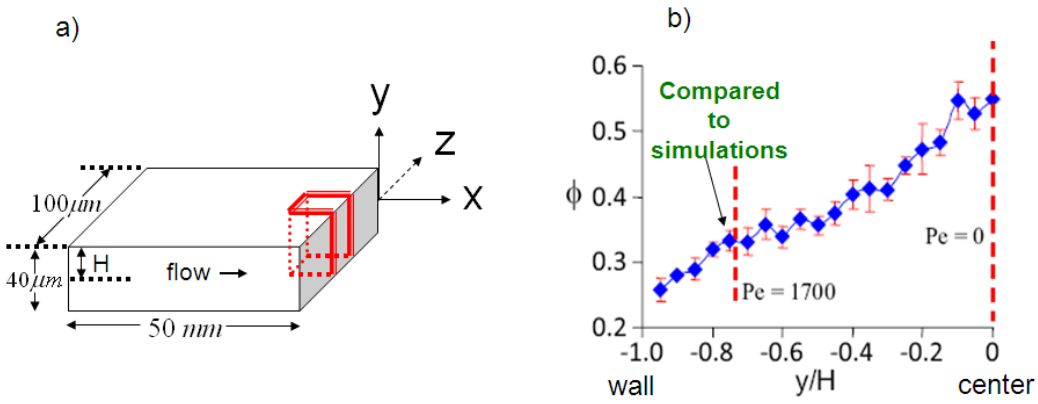

Figure 4.1: (a) The channel geometry with the Region of Interest (ROI) indicated by the red box; (b) The particle volume fraction along the y direction in region of interest where data is sampled after stopping the flow.

systems, the structure that produces normal stresses is preserved upon cessation of the flow provided the flow does not reverse [65]. After suspension flow stops, the ROI is scanned at high speed at ∼10 pixels/μm over 2.4 s and the 3D location of particles within are identified [69]. Fast scanning allows identification of particle locations before significant Brownian diffusion and sedimentation alter the local structure. Multiple scans are obtained and the insignificant Brownian and buoyant drift that occurs in the time between scans suggests the structure is unaltered in the duration of a single scan. The average particle number density $\bar{n} = N/V$ is used to calculate the local volume fraction as $\phi = \bar{n}\frac{4}{3}\pi r^3$. With the particle locations, local coordination can be used to investigate the suspension structure.

4.3 Comparison of microstructure: simulation and experiments

The particle configurations obtained from Accelerated Stokesian Dynamics simulation of sheared suspensions (chapter 2) are sampled over extended configurations

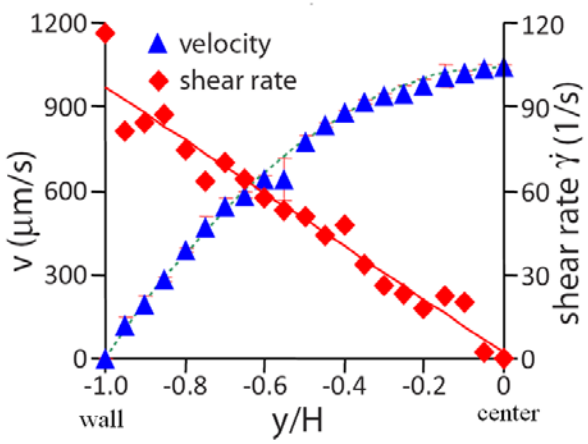

Figure 4.2: The measured velocity profile in the region of interest (triangles) and the parabolic profile (green dotted line) for comparison. The shear rate profile calculated from the velocity in y direction (diamonds) fit with a linear trend line (red solid line).

to determine the pair distribution function,

$$g(\mathbf{r}) = \frac{P_{1|1}(\mathbf{r})}{\bar{n}}, \tag{4.1}$$

where $P_{1|1}(\mathbf{r})$ is the probability of finding a particle at position $\mathbf{r}(r_x, r_y, r_z)$ given a particle centered at the origin, and $\bar{n}$ is the average particle number density. The pair space discretization method chosen here is different from that used in chapter 3; the change is made to be consistent with the experimental sampling procedure.

To compare with the experimental data, $g(\mathbf{r})$ is evaluated in different planes. For example, $g(x, y)$ defines $g(\mathbf{r})$ within the shear plane. To calculate $g(x, y)$, we consider all pair separations in which the magnitude of the z component of the separation satisfies $r_z < 2a$. The discretization of the planar pair space is convenient in polar coordinates, $\mathbf{r}^* = (r^*, \theta)$, with $r^* = \sqrt{(r_x^2 + r_y^2)}$ and $0 \leq \theta < 2\pi$ measured counter-clockwise from the positive x-axis to $\mathbf{r}^*$. For binning the data, the mesh chosen has bins separated by $\Delta r^* = 0.2a$, while $\Delta\theta = 3.6°$. The pair distribution, $g(x, y)$ is then evaluated from histogram of occurrence of pair separation vectors in the bins

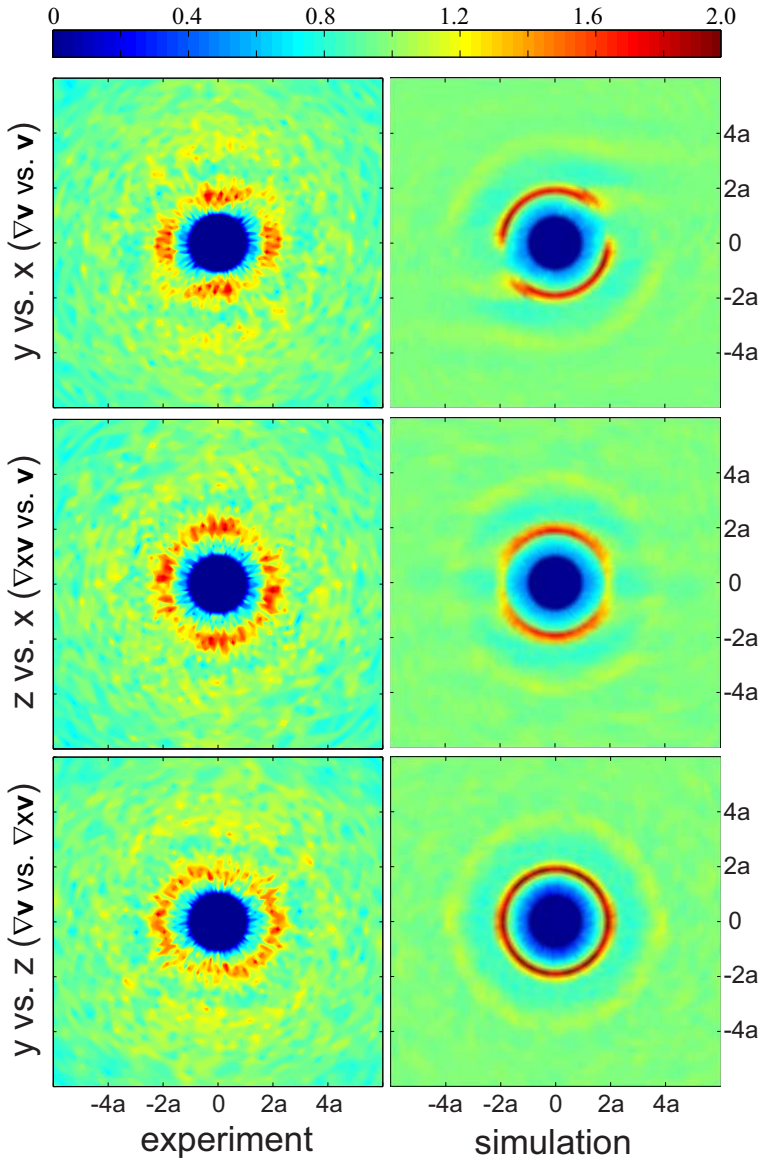

Figure 4.3: Experimental compilation (left) and Stokesian Dynamics (right) simulations of local pair distribution functions. Pair distribution functions $g(x, y)$ (first row), $g(x, z)$ (second row) and $g(z, y)$ (third row) are calculated in the ROI at -0.85 $\leq y/H \leq$ -0.65 with $\phi \approx 0.32$ and $Pe_y = 1700$; the simulations are performed for the same conditions of ϕ and Pe.

normalized by volume of the respective bins with averaging taken over a sufficiently large number of configurations that the result becomes independent of the number of configurations [24, 70]. The distributions $g(y,z)$ and $g(x,z)$ are evaluated in the same fashion. All plots of $g(\mathbf{r})$ span dark blue to red colors representing the range $0 \leq g(\mathbf{r}) \leq 2$.

In the experiments, the ROI is probed to obtain particle locations at $-0.85 \leq y/H \leq -0.65$ which represents the conditions of $\phi \approx 0.32$ and $Pe_y = 1700$ as indicated in figure 4.1b; the data is averaged over five experiments. The ASD simulations are performed for the same conditions of ϕ and Pe with simple shear flow, the simulated $g(\mathbf{r})$ is compared with experimental data as shown in figure 4.3. Both experiments and the simulations are seen to have a central region of particle exclusion. As a result of the way data is represented, symmetry through the origin is mandatory in all pair distribution functions. For $g(x,y)$ representing the shear-plane structure, inside of $r < 2a$ ($a =$ particle radius) a strong pair correlation exists in the compressional region near the line $x = -y$ and less in the extensional region neighboring a particle. This appears at $r < 2a$ due to the way out of plane data is projected. In the simulation, the near-contact peak is similar to that found in previous studies [14, 24] and is the primary microstructural generator of macroscopic normal stresses. This peak deviates from the experimental measurement in that the correlation is less uniform in the θ-direction, and in particular is stronger along the x and y axes. The shape of the wake is different in the extensional region in the two cases. In both experiments and simulations, a second peak just inside of $r = 4a$ is apparent but direct comparison of the structural details is difficult due to the weakness of correlation in this region and the resulting lower signal to noise ratio.

In $g(x,z)$ for the microstructure in the velocity-vorticity plane, the fore-aft symmetry apparent in the simulations is not found experimentally. We hypothesize

that the shear gradient along the z-direction, $\dot{\gamma}_z$, is non-zero in the experiment even though the measurements are near $z = 0$, and is significant enough to create increased correlation along the compressional region similar to $g(x, y)$, the shearing effect in the z direction is discussed in detail later. In the first ring of higher probability inside $r = 2a$, simulations show lower correlation in the x-direction near $z = 0$ that results from averaging the $g(x, y)$ data. This same projection for the experimental data results in higher pairwise probability in the x-direction near $z = 0$. A second ring of higher probability is found again inside $r = 4a$ for both experiments and simulations.

In the vorticity-shear gradient plane where flow goes into the plane of the page, the experiment demonstrate first and second order rings of higher probability in the pair distribution function $g(z, y)$ as found in the simulation. There are also dissimilarities, where simulations predict near uniformity in probability in the angular direction while the experiments show slightly higher probability in the vorticity direction.

4.4 Shearing effects in z direction

In the present experimental geometry, the boundaries in the z direction would induce shear rate variation in this direction as well. In the ROI, we compare the shear rates in the y and z directions and show that the shearing motion in the z direction is not completely negligible.

Earlier, we compared the simulation results for simple shear flow at $Pe = 1700$ and $\phi = 0.32$ with the experimental results for a region in ROI with $13\mu m \leq y \leq 17\mu m$. For this region in ROI, $\dot{\gamma}_y$ and $\dot{\gamma}_z$ are compared below.

Based on the dimensions of the channel cross-section $40\mu m \times 100\mu m$ ($L_x \times L_y$),

it could easily interpreted that

$$\frac{\dot{\gamma}_{y,max}}{\dot{\gamma}_{z,max}} \approx 2.5. \tag{4.2}$$

We consider that, $\dot{\gamma}_y$ vs. y and $\dot{\gamma}_z$ vs z are linear where y and z represent the distances from the center of the ROI. This is confirmed by figure 4.2 where $\dot{\gamma}_y$ vs. y is approximately linear. Thus, for the region in ROI with $13\mu m \leq y \leq 17\mu m$,

$$< \dot{\gamma}_y > \approx \frac{\dot{\gamma}_{y,max}}{L_y} \times 15\mu m, \tag{4.3}$$

$$< \dot{\gamma}_z > \approx \frac{\dot{\gamma}_{z,max}}{L_z} \times 5\mu m, \tag{4.4}$$

where $< \dot{\gamma}_z >$ is the magnitude of average z shear rate in ROI on either side of the center; we obtain $\frac{<\dot{\gamma}_z>}{<\dot{\gamma}_y>} \approx 0.05$ i.e. $Pe_z \approx 0.05 \times Pe_y \approx 85$. If the measurements in ROI are exactly symmetric in the z direction across the center, then shearing is z on either side of center would cancel each other's effect on $g(x, z)$ i.e. there would be fore-aft symmetry for $g(x, z)$. However, slightly off-centered measurements could result in asymmetry in $g(x, z)$ which could describe the experimental observation.

4.5 Conclusion

CLSM-enabled 3D measurement of particle locations in experiments enable direct microstructure comparison to particle locations generated by Accelerated Stokesian Dynamics simulation. The shear rate variation in the pressure driven flow results in suspension migration in the velocity-gradient (y) direction. The experimental technique provides access to variations in ϕ and Pe across the channel cross-section.

Experimental and simulated pair distribution functions largely agree, though the details deviate possibly due to the lateral confinement of the suspension in the z-direction.

Chapter 5

Motion correlations : microscopic study of shear thickening

5.1 Introduction

Shear thickening is observed when a concentrated suspension is subjected to strong shearing. In this context, jamming occurs when there is a discontinuous rise in the viscosity of the suspension under shear which obstructs the flow completely (or almost completely). Bertrand *et al.* [71] have shown that non-Brownian suspensions of moderate concentrations demonstrate shear thickening at high shear rates. In addition, at high enough concentrations, the suspension under shear can be transformed into persisting paste; they termed this behavior as 'shear induced jamming.' Lootens *et al.* [72] have conducted strain-rate controlled measurements of concentrated colloidal suspensions and observed 'giant' stress fluctuations when the 'transition' shear rate is reached. Haw [73] studied flow of concentrated Brownian suspensions through a contraction induced by a pressure gradient and found erratic fluctuations in the flow speed beyond a critical concentration which is suggestive of 'transient jamming'. Computationally, Foss & Brady [14] studied the dependence of the relative viscosity η_r on Péclet number for $0.316 \leq \phi \leq 0.49$ in hard sphere

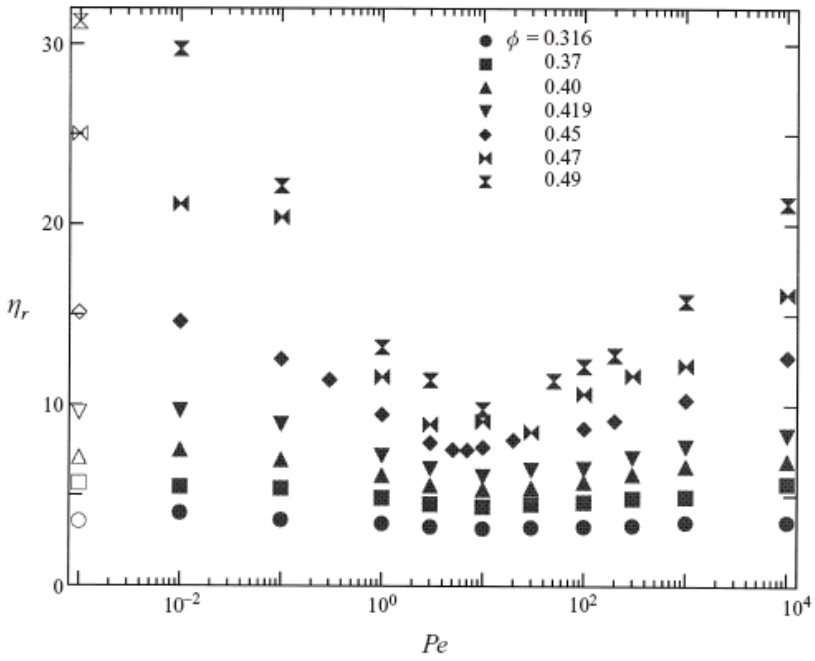

Figure 5.1: The plot is obtained from Foss & Brady (2000) who investigated Stokesian Dynamics simulation for hard-sphere suspensions under shear. The relative viscosity η_r data is presented for a range of volume fractions $0.316 \leq \phi \leq 0.49$ as the Péclet is raised through six decades of magnitude. The open symbols on the far left describes the relative viscosity data determined by an equilibrium Green-Kubo analysis for $Pe \to 0$.

suspensions using Stokesian Dynamics simulation. They observed shear thinning for $Pe \approx 10$ and smaller, while shear thickening behavior for higher Pe as seen in figure 5.1. The tendency to shear thicken increases with particle concentration. The simulation results are in good agreement with the experiments of van der Werff & de Kruif [16] on silica suspensions and of D'Haene *et al.* [15] on PMMA particle suspensions.

Several attempts have been made to understand the shear thickening and jamming phenomena in concentrated suspensions at microscopic level and to model this behavior. It is considered that the shear thickening is a result of shear induced organization of the particles into clusters. Using Stokesian Dynamics simulations,

Brady & Bossis [2] observed clustering among the particles in a monolayer under shear. Ball & Melrose [74] simulated the shear flow where only lubrication terms in the hydrodynamics forces are considered; they found clusters of particles along the compressional axis in 3-D systems. Yurkovetsky & Morris [75] have observed that, as Péclet number increases, the particles have higher tendency to form 'open triplets' (linear structures) as opposed to 'closed triplets' (equilateral triangle structures). Based on the dependence of the value of pair distribution function at contact on the Péclet number, $g(2) \sim Pe$, Brady & Morris [17] theoretically predicted thickening in sheared suspensions. Farr *et al.* [76] used a cluster aggregation approach to provide a microscopic theory for jamming behavior based on the 'rod-like' motion of the particle clusters. Experimentally, using on small angle neutron scattering measurement, Maranzano & Wagner [77] measured microstructural response associated with shear thickening in colloidal suspensions. Most of the above studies use the spatial correlation of particles to investigate the formation of clusters associated with shear thickening. We provide computational evidence to the long range structures based on a novel approach of pair motion correlations. This approach facilities further understanding and characterization of the shear thickening behavior.

We study the shear induced microstructural evolution in Brownian suspensions based on 'velocity-correlation' approach, where the particle positions and velocities under simple shear flow are generated using the Accelerated Stokesian Dynamics (ASD) technique. Our idea is that as the formation of 'hydrodynamic clusters' is associated with the shear thickening (or jamming) in Brownian suspensions, long-range motion correlations will exist which characterize the rigidity of the 'clusters'. Farr *et al.* [76] used the idea of 'rod-like' motion of the particle clusters to establish a theory for jamming behavior, however they did not provide any statistical evidence for the correlated motion.

The ASD simulated simple shear flow is given by $\mathbf{u} = (\dot{\gamma}y, 0, 0)$. Note that the product of velocity fluctuation vectors for a particle pair would give a nine-component correlation tensor. We focus on correlation of velocity-gradient (y) direction velocities of a particle pair, $< {u_y}^i(\mathbf{r}_i) \cdot {u_y}^j(\mathbf{r}_j) >$, where $\mathbf{r}_j - \mathbf{r}_i = \mathbf{r}$. As there is no convective motion in the y direction, the y velocities obtained from the simulation are fluctuations. We study y-velocity correlations as a function of particle concentration and the Péclet number. We also investigate the role of hydrodynamics by comparing the microscopic analysis of the ASD simulated flow to that of Brownian Dynamics simulated flow which neglects the hydrodynamic effects.

5.2 Simulation method

Simple shear flow of viscous suspensions is simulated using Accelerated Stokesian Dynamics (ASD) in the limit of zero particle Reynolds number. The simulation method is described in chapter 2. The flow, the velocity gradient and the vorticity directions are defined by x, y and z respectively. For the simulation results described here, the distances are made dimensionless with particle radius a while time is measured in strain units $\dot{\gamma}t$ which is also a dimensionless form.

5.3 Formulations for motion correlation

To study the motion correlations, we incorporate the pair product of the y velocities in the pair distribution function as described below. The pair distribution function is given by

$$g(\mathbf{r}) = \frac{1}{N} < \sum_{i=1}^{N} \sum_{j=1}^{N} \delta(\mathbf{r} + \mathbf{r}_j - \mathbf{r}_i) >, \tag{5.1}$$

which represents the pair particle density at a separation vector $\mathbf{r} = \mathbf{r}_j - \mathbf{r}_i$, normalized by the average density of the system. The y-velocity correlation is given by

$$V^y(\mathbf{r}) = \frac{1}{N} < \sum_{i=1}^{N} \sum_{j=1}^{N} u_i^y u_j^y \delta(\mathbf{r} + \mathbf{r}_j - \mathbf{r}_i) >, \tag{5.2}$$

where u_i^y & u_j^y are instantaneous velocities (normalized by $\dot{\gamma}a$) in the y-direction of particles located at $\mathbf{r}_i$ & $\mathbf{r}_j$. This formulation denotes the average velocity correlations of the pairs separated by a vector $\mathbf{r} = \mathbf{r}_j - \mathbf{r}_i$, normalized by the average density of the system.

The y-velocity correlation normalized by the pair distribution function is stated as

$$\bar{V}^y(\mathbf{r}) = \frac{< \sum_{i=1}^{N} \sum_{j=1}^{N} u_i^y u_j^y \delta(\mathbf{r} + \mathbf{r}_j - \mathbf{r}_i) >}{< \sum_{i=1}^{N} \sum_{j=1}^{N} \delta(\mathbf{r} + \mathbf{r}_j - \mathbf{r}_i) >}. \tag{5.3}$$

Equation (5.3) represents the the average velocity correlations of the pairs separated by a vector $\mathbf{r}$ normalized by the corresponding pair density at $\mathbf{r}$ separation. This formulation gives the strength of the motion correlation *per pair* at a given separation distance.

ASD generated particle positions and velocities are used to obtain the data. The pair distribution function $g(\mathbf{r})$ and the y-velocity correlation $\bar{V}^y(\mathbf{r})$ are evaluated by making grids on $\mathbf{r} = (r, \theta, \psi)$ pair space where θ is the polar angle measured counter-clockwise from the positive x-axis and ψ defines the azimuthal angle measured from the positive z-axis. The discretization mesh is chosen such that the spherical bins are separated by a distance of 0.025 (this distance is non-dimensionalized with radius of the particle). For every bin, the angular discretization in $0 \leq \theta < 360^\circ$ is fixed at 3.6° while the angular discretization in $0 \leq \psi < 180^\circ$ is fixed at 9°.

If the motion of the particles is not correlated, $V^y(\mathbf{r}) = 0$. For a sheared system, when two particles interact in an infinitely dilute concentration limit, the y-velocities will remain negatively correlated ($\bar{V}^y(\mathbf{r}) < 0$) and the correlation fades away with distance [6]. However, in the dense systems under shear, the formation of rigid clusters or long-range structures of different sizes and shapes would yield a different form of velocity correlations. For example, consider a 4-particle *linear* cluster in the shear plane as described in figure 5.2. Suppose a rigid-body (rod-like) motion for the particle cluster. The cluster rotates in the shear plane about its center of mass. The shearing motion would induce positive correlations in the particles at each side of the rod's center of mass and negative correlations in the far end particles of the rod. We observe that the particle pairs '1,2' and '3,4' ('2,3' is an exception) yield dominant positive correlation at $r/a \approx 2$. On the other hand, the pairs '1,3' and '2,4' show negative correlation, indicating dominant negative correlation at $r/a \approx 4$. Correlation between the particles at the either end of the cluster (pair '1,4') would cause negative correlations at longer distances. Thus, the motion correlation response is expected to change significantly as the particles form rigid-body clusters in the shear flow.

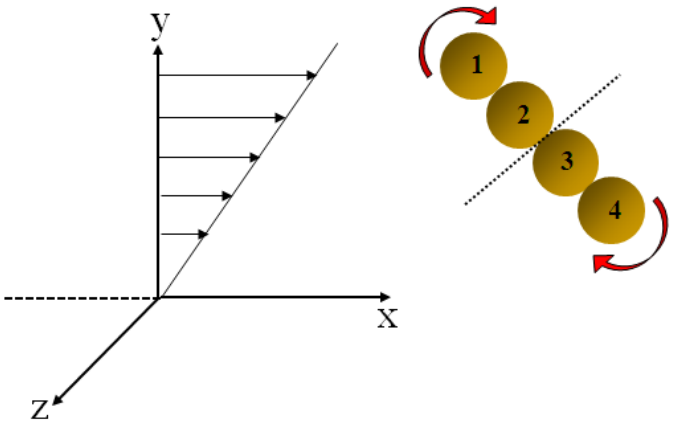

Figure 5.2: Schematic of a correlated particle-cluster.

5.4 y-velocity correlations : effect of ϕ at $Pe = 1000$

5.4.1 Spherically averaged y-velocity correlations

Figure 5.3 shows the spherical mean of $g(\mathbf{r})$ and $\bar{V}^y(\mathbf{r})$ for various particle volume fractions at $Pe = 1000$ (bin size $\Delta r = 0.025$). As ϕ grows, the pair correlation in the bin adjacent to contact, $g(2)$, increases; this is because of the decrease in Brownian diffusion and and the increase in the hydrodynamic stresses as ϕ increases [78]. The rise in the near-contact values with ϕ is followed by an increasingly bigger dip between $2 < r/a < 3$ and then by rise in the peak value at $r/a \approx 4$; this behavior is consistent with the observation by Morris & Katyal [24] who studied the pair correlation asymmetry in the shear flow as a function of ϕ and Pe using highly time-resolved and spatially-resolved (much smaller first bins) SD simulations.

The plot of $\bar{V}^y(r)$ vs. r in figure 5.3b describes that, for the dilute case of $\phi = 0.05$, the system is dominated by 'two-body' interaction effect i.e. the effect of a pair interacting in a dilute limit as observed by Batchelor & Green [6]; thus, $\bar{V}^y(r)$ remains negative for several bins near the contact and the correlation fades away as the distance increases.

For $\phi = 0.10$, the near contact bins are again dominated by the 'two-body' interaction. On the other hand, the farther bins show positive y-velocity correlations ($\bar{V}^y(r) > 0$) which we consider as an effect of the 'many-body' interaction. The correlation falls to zero beyond $r/a \approx 4$. We observe that, for $\phi = 0.20$, $\phi = 0.35$ and $\phi = 0.47$, the contact bins and several following bins show $\bar{V}^y(r) > 0$ suggesting dominant 'many-body' interactions or an effect of formation of the particle clusters with 'rigid-body' motion. In general, these clusters could be of different sizes and shapes. Note that, for $\phi = 0.35$ and $\phi = 0.47$, $\bar{V}^y(2)$ is the maximum value of the correlation function (for the present bin size $\Delta r = 0.025$) while for $\phi = 0.20$ the

maximum is observed at r away from the contact bin. Another important observation from figure 5.3b is that, for $\phi = 0.35$ and $\phi = 0.47$, there is a notable negative correlation at longer distances beyond $r/a \approx 7$. In addition, at high concentrations ($\phi \geq 0.20$), a distinctive dip is observed at $r/a \approx 4$ which we probe further in the shear plane.

5.4.2 y-velocity correlations at the contact in the shear plane

Parsi & Gadala-Maria [25] by experiment and Phung *et al.* [50] by simulation examined the effect of flow at large Péclet number upon the pair distribution function. Their work demonstrated that near contact there is an accumulation of the pair probability in the compressional quadrant while the probability has comparatively smaller values in the extensional quadrant. Figure 5.4a shows consistent results for $g(2)$ i.e. the value of $g(\mathbf{r})$ in the bin adjacent to contact, which is plotted with respect to θ in the shear plane ($\psi = 90^0$). Note that the mean of $g(2)$ increases with ϕ which qualitatively matches with the results of Morris & Katyal [24] who examined $g(2)$ for much smaller values of Δr compared to this work.

Figure 5.4b shows that, for $\phi \leq 0.20$, $\bar{V}^y(2) < 0$ in significant portions of both the compressional and extensional quadrants owing to the dominant 'two-body' interaction for these lower concentrations. On the other hand, for $\phi = 0.35$ and $\phi = 0.47$, $\bar{V}^y(2) < 0$ in the extensional quadrant while $\bar{V}^y(2) > 0$ in the compressional quadrant. This growing positive correlation in the contact bins of the compressional quadrant is a result of the 'many body' interaction i.e. an effect of 'rigid-body' motion of the particle clusters in this quadrant. To probe these clusters further, we study average $\bar{V}^y(r)$ behavior in the compressional quadrant of the shear plane defined by $\psi = 90^0$ where $108^0 < \theta < 168^0$ as described in the following section. Another

important observation from figure 5.4b is that the maximum values of $\bar{V}^y(2,\theta)$ is observed in the region around $\theta \approx 90^0$.

5.4.3 y-velocity correlations in the compressional quadrant of the shear plane

Figure 5.5 shows $g(r)$ and $\bar{V}^y(r)$ in the compressional quadrant of the shear plane averaged over the angular distribution between $108^0 < \theta < 168^0$ at $Pe = 1000$ for various ϕ values. We observe that $g(r)$ under these conditions behaves similar to the spherically averaged $g(r)$. Considering motion correlation, we note that at $\phi \leq 0.20$, $\bar{V}^y(2) < 0$ similar to spherically averaged motion correlations

At high concentrations, $\phi = 0.35$ and $\phi = 0.47$, $\bar{V}^y(r) > 0$ in the bins near contact, which is similar to the spherically averaged y-velocity correlations and is related to different types of particle clusters with 'rigid-body' motion. However, at $r/a \approx 4$, a remarkable negative correlation 'dip' is observed which grows with ϕ. The strong positive correlations near the contact $r/a \approx 2$ followed by the anti-correlation at $r/a \approx 4$ specifically indicates the presence of *linear* particle clusters with 'rod-like' motion in the compressional quadrant; the interpretation is based on the characteristics of the representative *linear* cluster shown in figure 5.2. In addition, at high concentrations, $\bar{V}^y(r) < 0$ beyond $r/a \approx 7$ (see inset of figure 5.5b) demonstrating presence of motion correlations at longer distances.

Earlier studies including [14] show that, under strong shear, the tendency to shear thicken increases with particle concentration (see figure 5.1). Our study suggests that the motion correlation transform form dominant 'two body' interaction for lower concentration to a significantly different state for higher concentrations. The motion correlation demonstrate 'rigid-body' motion of the particle clusters at high

concentrations. Specifically, it indicates growth in the *linear* 'rod-like' clusters in the compressional quadrant as the concentration increases. The stress in a rod roughly grows as the length cubed [2], which could be related to the higher tendency to shear thicken as ϕ increases. Thus, the motion correlation response (which is highly ϕ sensitive) provides a microstructural understanding to the shear thickening state.

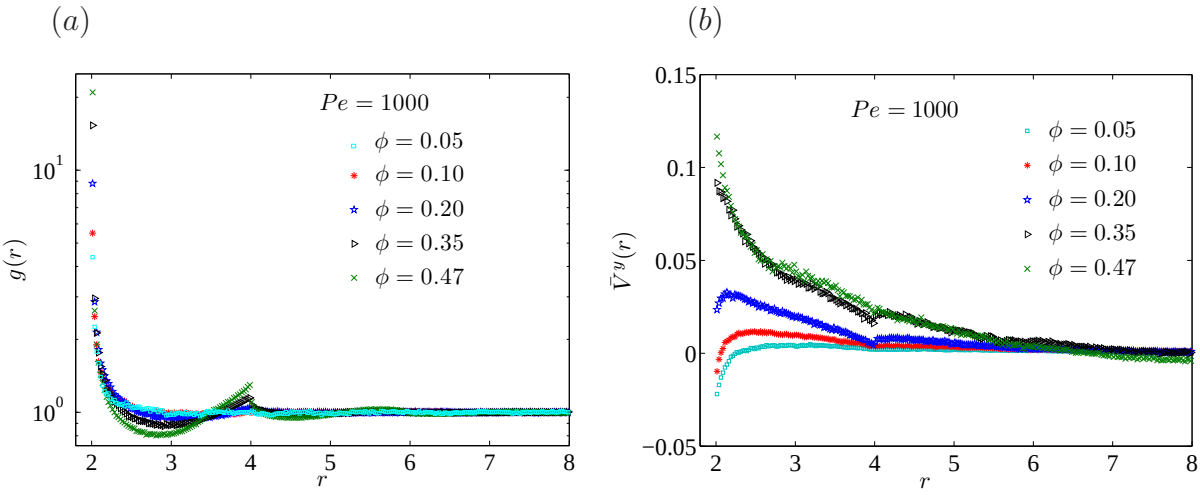

Figure 5.3: At $Pe = 1000$ for different ϕ (a) spherical average of $g(r)$; (b) spherical average of $\bar{V}^y(r)$.

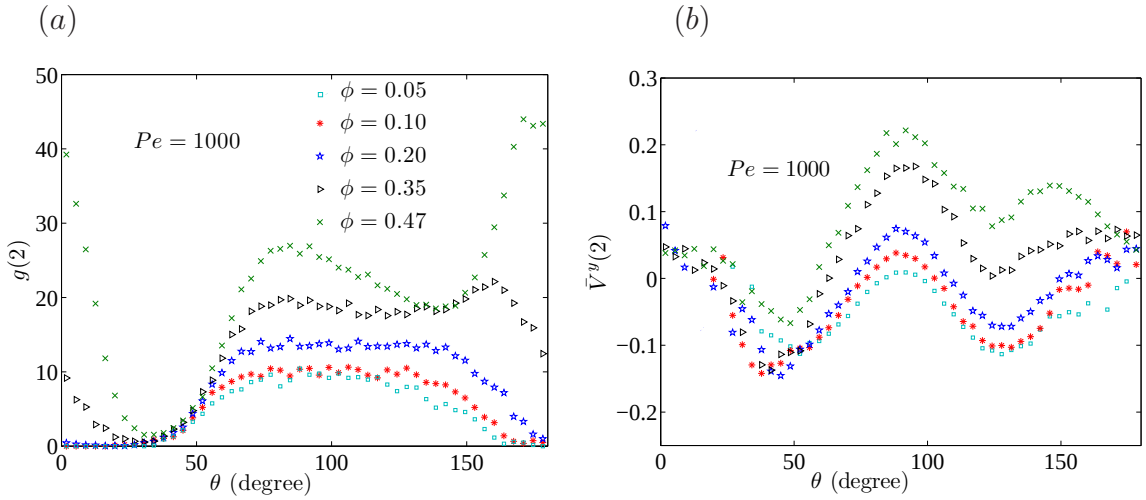

Figure 5.4: At $Pe = 1000$ for different ϕ (a) contact values of the $g(\mathbf{r})$ in the shear plane; (b) $\bar{V}^y(\mathbf{r})$ at contact in the shear plane. The legend in (a) also applies to (b).

(a)

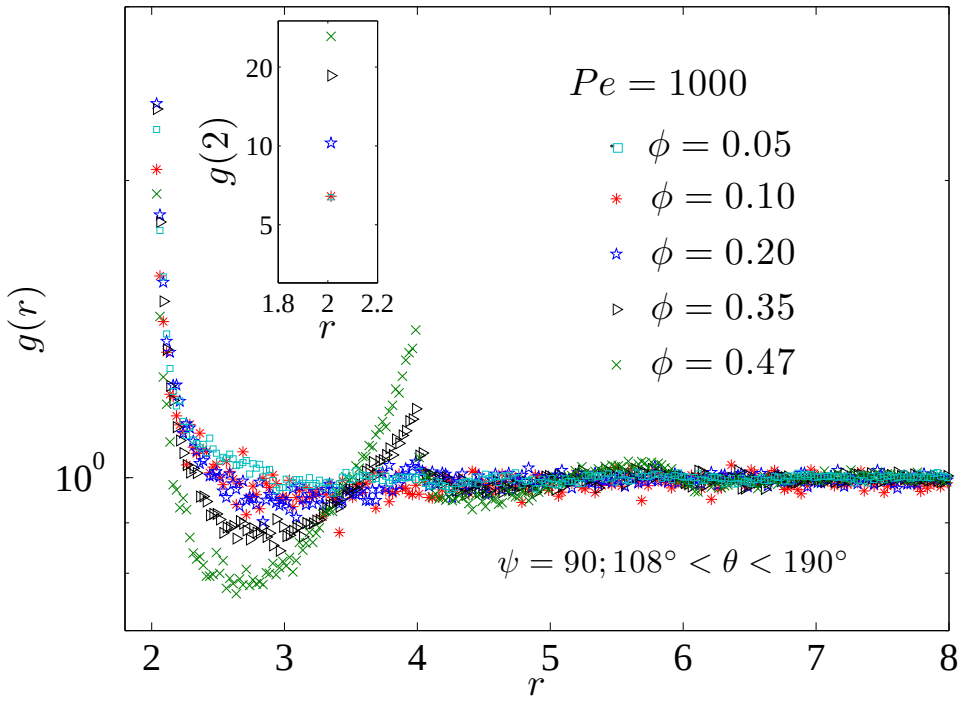

(b)

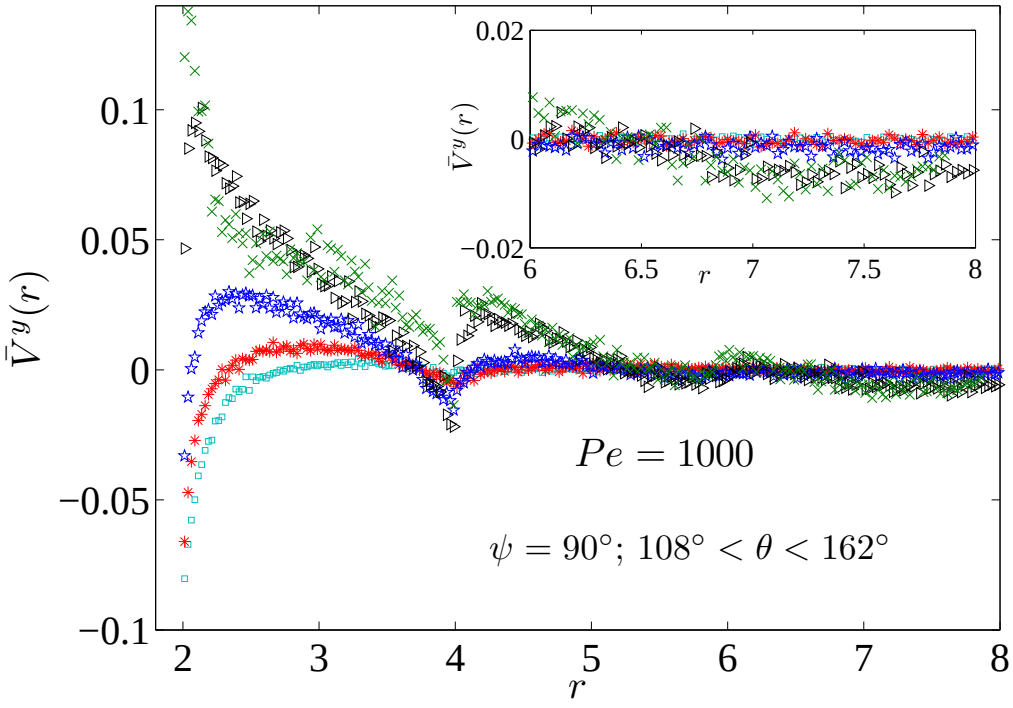

Figure 5.5: At $Pe = 1000$ for different ϕ (a) average $g(r)$ in the compressional quadrant of the shear plane; (b) average $\bar{V}^y(r)$ in the compressional quadrant of the shear plane. The legend in (a) also applies to (b).

5.5 y-velocity correlations : effect of Pe at $\phi = 0.47$

5.5.1 Spherically averaged y-velocity correlations

In this section, we seek to examine the effect of Péclet number on the motion correlations. Figure 5.6 shows that the spherical mean of $g(\mathbf{r})$ and $\bar{V}^y(\mathbf{r})$ for $\phi = 0.47$ at $Pe = 1$ and $Pe = 1000$. The $g(r)$ at $Pe = 1000$ has higher values near contact and then the curve drops more rapidly compared to $Pe = 1$; this behavior qualitatively agrees with the study by Morris & Katyal [24] and also with the theoretical understanding of the boundary layer structure developed by Brady & Morris [17] and Wilson [51]. In addition, the dip between $2 < r/a < 3$ is closer to unity for $Pe = 1000$, which also agrees with the observation by Morris & Katyal [24].

Figure 5.6b shows that, at $Pe = 1$, $\bar{V}^y(r)$ remains positive in the near contact bins but the correlations are significantly weak compared to that at $Pe = 1000$. The motion correlation at $Pe = 1$ gradually falls to zero at $r/a \approx 6$ showing absence of long-distance motion correlations; on the other hand, at $Pe = 1000$, the motion correlations become negative beyond $r/a \approx 7$. In addition, similar to $Pe = 1000$, a 'dip' is observed at $r/a \approx 4$ for $Pe = 1$. We further explore the motion correlations in the shear plane.

5.5.2 y-velocity correlations at the contact in the shear plane

At $\phi = 0.47$, for both Pe conditions, the $g(2)$ in the shear plane exhibits compressional and extensional quadrants and the mean $g(2)$ increases with Pe as expected (figure 5.7a). At $Pe = 1$, $\bar{V}^y(2)$ remains negative in significant portions of both compressional and extensional quadrants, which is indicative of dominant 'two-body' interactions (figure 5.7b). To the contrary, at $Pe = 1000$, $\bar{V}^y(2) > 0$

in the entire compressional quadrant, a characteristic change suggesting the effect of dominant many body interactions or long range structures in the compressional quadrant as noted earlier.

5.5.3 y-velocity correlations in the compressional quadrant of the shear plane

The plot of $g(r)$ and $\bar{V}^y(r)$ in the compressional quadrant of the shear plane averaged over the angular distribution between $108^0 < \theta < 168^0$, at $\phi = 0.47$ for both Pe numbers, is shown in figure 5.8. Note that $g(r)$ under these conditions behaves similar to the spherically averaged $g(r)$.

Figure 5.8b shows that, $\bar{V}^y(2) < 0$ at $Pe = 1$, which demonstrates dominant 'two-body' motion correlations near contact in the compressional quadrant. For the following bins, $\bar{V}^y(r)$ has similar but significantly weak motion correlation pattern at $Pe = 1$ as compared to that at $Pe = 1000$. Foss & Brady [14] computationally and D'Haene *et al.* [15] experimentally have shown that, at high ϕ, $Pe \approx 1000$ provides an extensively higher shear thickened state compared to $Pe \approx 1$ (see figure 5.1). The shear thickening with respect to Péclet number is accompanied by pronounced rise in the strength of motion correlations as we have demonstrated above.

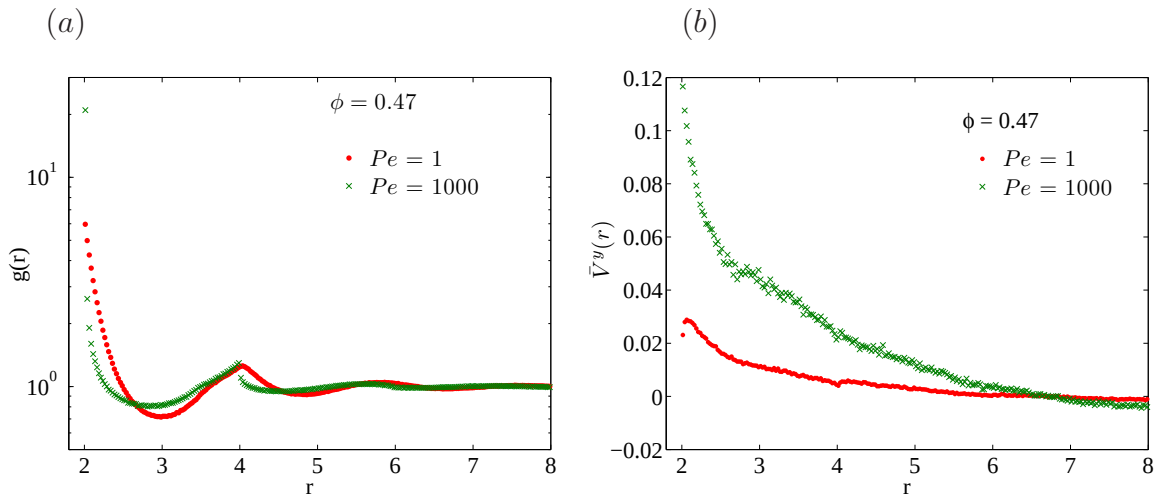

Figure 5.6: At $\phi = 0.47$ for different Pe (a) spherical average of $g(r)$; (b) spherical average of $\bar{V}^y(r)$.

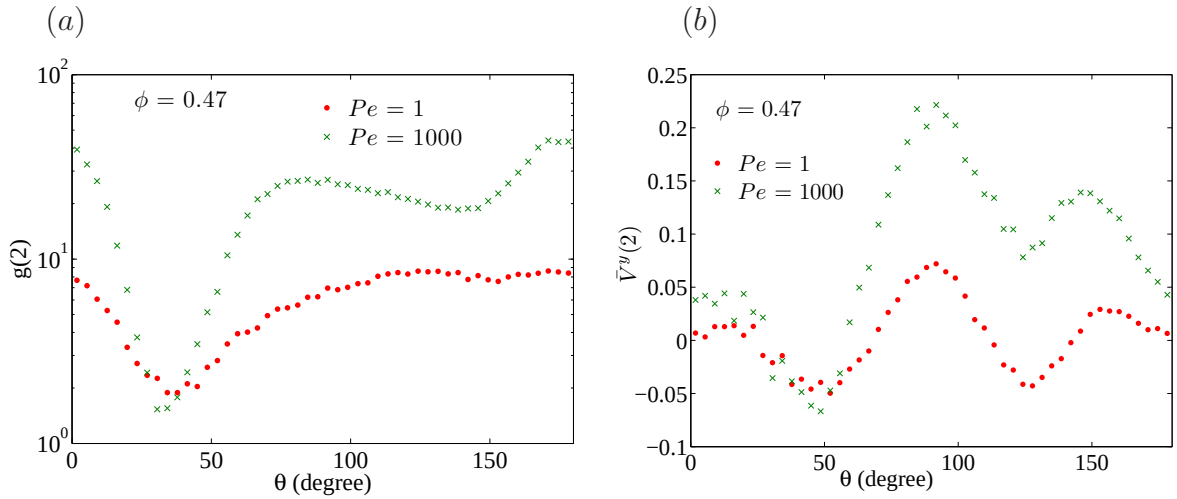

Figure 5.7: At $\phi = 0.47$ for different Pe (a) contact values of the $g(\mathbf{r})$ in the shear plane; (b) $\bar{V}^y(\mathbf{r})$ at contact in the shear plane.

(a)

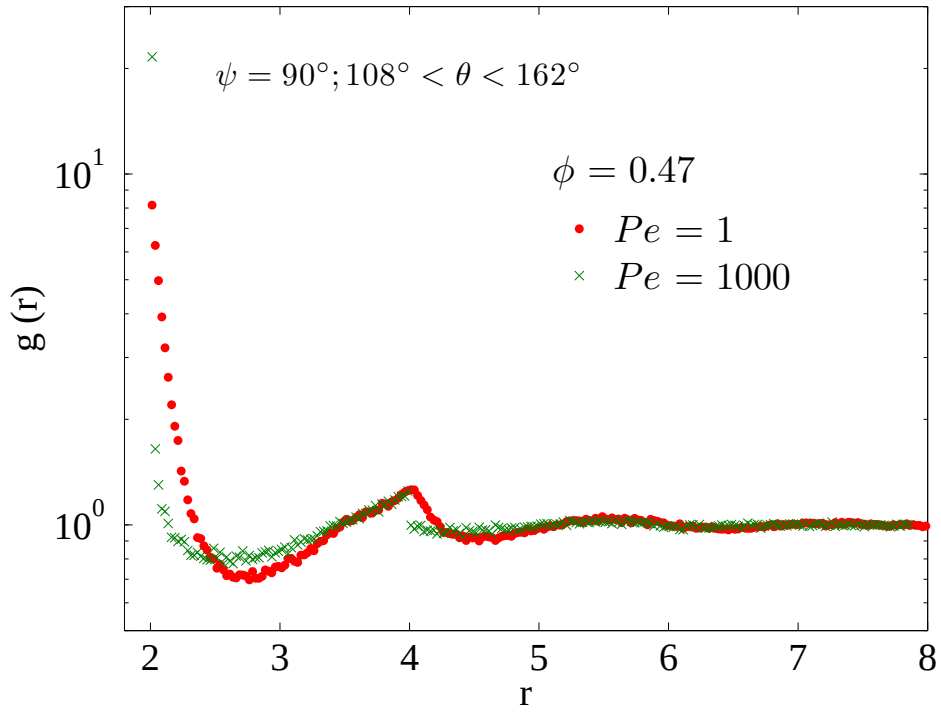

(b)

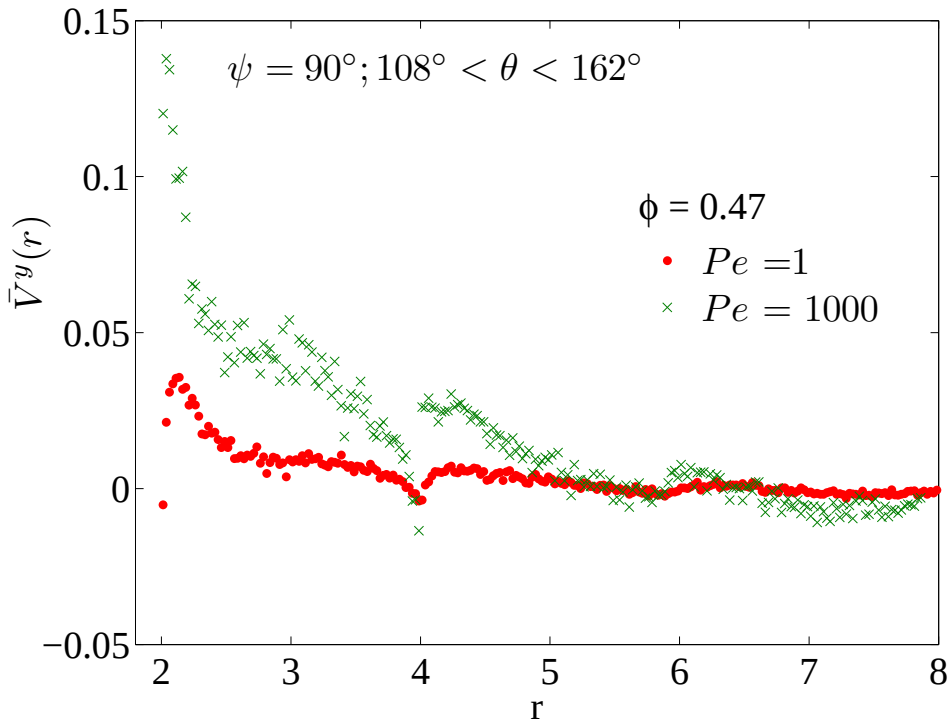

Figure 5.8: At $\phi = 0.47$ for different Pe (a) average $g(r)$ in the compressional quadrant of the shear plane; (b) average $\bar{V}^y(r)$ in the compressional quadrant of the shear plane.

5.6 Role of hydrodynamics: comparison with Brownian Dynamics

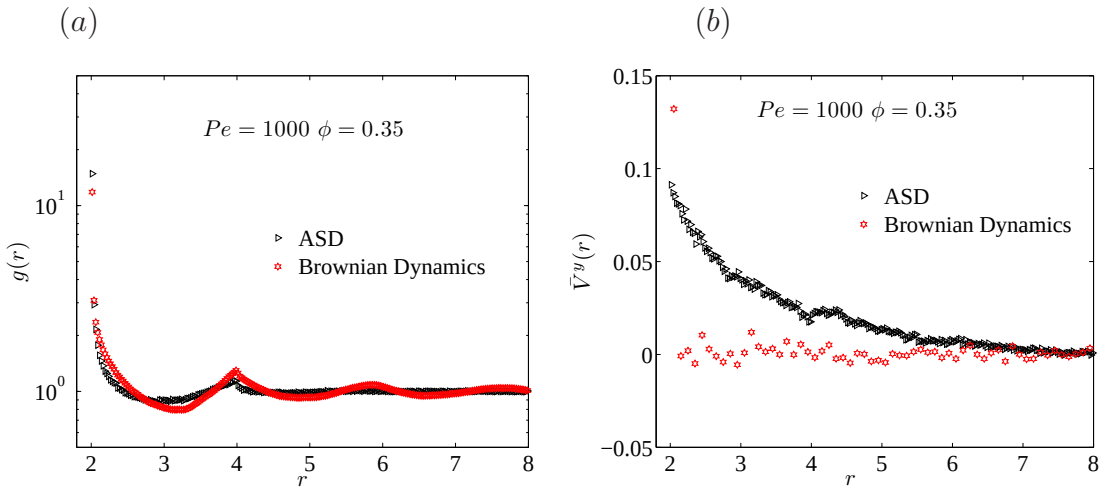

Figure 5.9: At $\phi = 0.47$ and $Pe = 1000$ (a) spherical average of $g(r)$; (b) and spherical average of $\bar{V}^y(r)$ in ASD and Brownian Dynamics simulated flows.

In this section, we compare the y-velocity correlations in the typical ASD simulated shear flow with that in the Brownian Dynamics (BD) simulations which neglects hydrodynamic interactions. Figure 5.9 shows the spherical mean of $g(\mathbf{r})$ and $\bar{V}^y(\mathbf{r})$ for $\phi = 0.47$ at $Pe = 1000$ in case of ASD and BD simulated flows. The $g(r)$ for ASD has higher values near contact and then the curve drops more rapidly compared to BD simulated $g(r)$. In addition, the dip between $2 < r/a < 3$ is closer to unity for the ASD simulated $g(r)$.

Figure 5.9b shows that, for BD simulated flow, $\bar{V}^y(2)$ is positive and for the following bins $\bar{V}^y(r)$ fluctuates around zero; this behavior is strikingly different from the long-range y-velocity correlations observed in the ASD simulated flow. The lack of correlated motion indicate that the BD simulated flow might not show shear thickening behavior at the given conditions of Pe and ϕ which is indeed true as observed by Brady [79]. Thus, only ASD system which takes into account the

hydrodynamic interactions between particles may capture the long-range structures and the associated thickening behavior observed in the sheared systems.

5.7 Conclusion

The velocity or motion correlations suggest long-range structures, especially 'rod-like' *linear* clusters in the compressional quadrant of shear plane at high ϕ and Pe. The strength of these motion correlation increases with increase in either ϕ or Pe, which is accompanied with increase in shear thickening state of the system. The shear flow simulated by ASD and Brownian Dynamics show very distinct y-velocity correlations, which underlines the role of hydrodynamic interactions in inducing the long-range structures. In the present study, we investigated only one component ($< {u_y}^i(\mathbf{r}_i) \cdot {u_y}^j(\mathbf{r}_j) >$) of the fluctuation velocity correlation tensor for the particle pair; the other components of the tensor need to be probed to further understand the long-range structures in different dimensions. The abrupt thickening or jamming behavior is not seen in these simulations; perhaps introduction of the frictional interactions between particles could lead the system into the jamming limit with corresponding changes in the motion correlations, a further study of this issue is warranted.

Chapter 6

Particle pressure induced self-filtration in concentrated suspensions

6.1 Introduction

Flows of concentrated suspensions, from mud to ceramic precursor slurries, are commonly encountered in nature and industry. Suspensions ranging from colloidal dispersions to wet granular flows, demonstrate ability to generate spatial variation in the material concentration under various flow conditions. Isa *et al.* [80] studied micro-fluidic flow of concentrated colloidal suspensions; they observed variation in the material concentration along the flow channel. In liquid-immersed granular flows, dilatancy effects are seen for underwater granular avalanches [81]. Relevant works on the spatial redistribution of the suspension concentration also include the phenomena of suspension and paste extrusion studied in basic and applied research [82, 83]. Haw [73] investigated 'self-filtration' in concentrated colloidal suspensions in which the effluent from a pressure-driven contraction flow has lower solid loading than the upstream material; this work is closely related to our study in terms of geometry and

A part of this chapter is submitted as *Particle pressure induced self-filtration in concentrated suspensions*, S. D. Kulkarni, B. Metzger and J. F. Morris, Phys. Rev. Lett. (Nov. 2009)

solid fraction. The earlier works [80, 73] have linked the concentration variation or the 'self-filtration' in dense suspensions to the erratic flow oscillations observed in these materials. The present study of flow of dense non-colloidal suspensions through a contraction elucidates the development of a flow-induced liquid pressure field and its relation to the 'self-filtration' in steady and oscillatory flows.

Particle migration is observed in a number of low-Reynolds-number suspension flows, including curvilinear [27] and pressure-driven rectilinear flows [29]. The migration has been modeled based on 'particle pressure' as driving potential [34, 18, 31]. The particle pressure Π is the mean normal stress exerted by the particle phase $\Pi = -\frac{1}{3}[\sum_{11}^{p} + \sum_{22}^{p} + \sum_{33}^{p}]$ in a sheared suspension [30]. A compressive particle pressure Π quantifies the tendency of the dispersed phase to spread under shear. For this spreading to take place, liquid must replace the particles, and there must be an equal but opposite (and hence, suction) pressure in the suspending liquid $\Pi_{liq} = -\Pi(\dot{\gamma}, \phi)$; this is deduced as a result of the constraint of material incompressibility [31, 32]. The relation of diffusion with liquid pressure in solid-liquid systems is a broadly relevant topic, e.g. for the ultrafiltration process, where theory of the suspending liquid pressure has established equivalency of Fick's and Darcy's law [84]. Measurements at a porous boundary show evidence of opposing normal stresses in the two phases of sheared suspensions [23]. A clear demonstration is provided by measurement of the solvent pressure in a sheared suspension, by a method analogous to measurement of osmotic pressure in quiescent solutions across a semipermeable membrane [32].

In this work, we study a contraction geometry, in which distinct shear-rate regions form and are found to have significantly different solvent phase suction pressures Π_{liq}. In addition, at large ϕ, we observe a reduction of suspension concentration

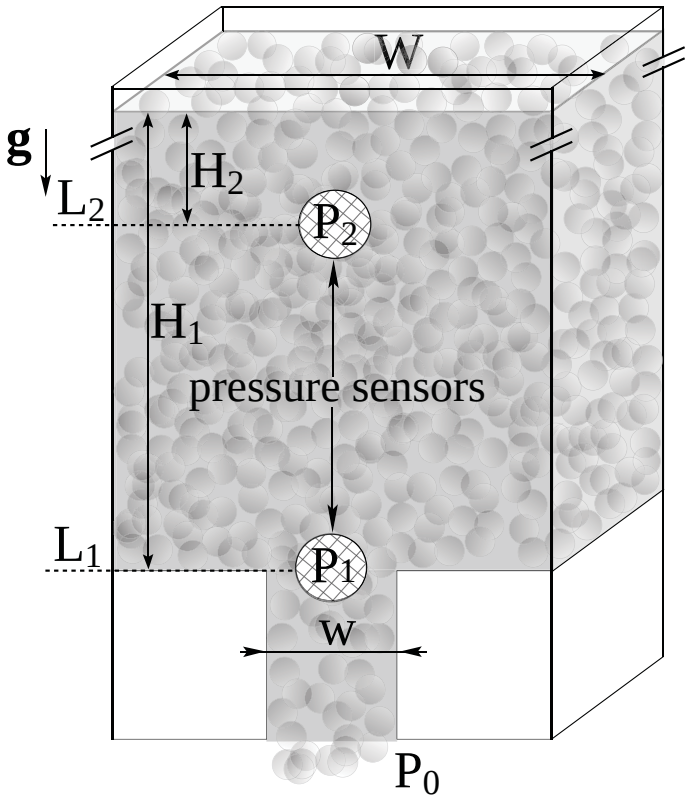

Figure 6.1: Sketch of the experiment.

downstream of the contraction relative to the upstream. This dilation or 'self-filtration' and its relation to the flow-induced liquid pressures is studied for steady and oscillatory flow conditions.

6.2 Experiments: set-up and protocol

Materials & apparatus: The suspensions are composed of spherical polystyrene particles (380-500 μm diameter; Maxi-Blast Inc.) and UCON 50-HB-660 (Dow Chemical), a Newtonian liquid with viscosity $\eta_f = 0.3$ Pa.s and density 1.05 g.cm^{-3} at 25°, very close to that of polystyrene. Inertia is negligible as $Re_p = \rho U a/\eta_f \ll 1$, where U is the average flow speed, a is the sphere radius, and ρ and η_f are the

fluid density and viscosity, respectively. Flows of two more viscous liquids without particles, mixtures of UCON 75-H-90000 and 75-H-1400 (both of density 1.09 g.cm^{-3}) having viscosities 36.5 Pa.s (liquid X) and 7 Pa.s (liquid Y) at 25°, are also studied.

The flow passes through a contraction in a vertical channel constructed of acrylic, with geometry shown in figure 6.1. The length, width (W) and depth of the channel are 20, 2.5 and 2 cm, respectively. The contraction is formed by symmetrically inserting two rectangular blocks of length 4 cm, depth 2 cm (equalling the channel depth), and of width yielding the ratio of the contraction channel width to that of original channel $w/W = 1/6$ (figure 6.1). A CCD camera images the flow along an axis orthogonal to the channel wall.

For liquid pressure measurement, holes are made along the channel boundary, one at the beginning of the contraction (level L_1) and the other 5 cm vertically above the contraction (level L_2) as shown in figure 6.1. A horizontal tube connected to each hole is filled with the suspending liquid and its other end is attached to a differential pressure transducer (Omega; ± 1 psi). The differential pressure transducer measures the system pressure relative to atmospheric pressure. For suspension flows, the liquid pressure alone is measured by placing across each hole a screen with 200 μm square openings to retain the particles in the channel and not to let them enter in the tubes.

Data acquisition: The CCD camera records the decline of the suspension column height as the material flows through the contraction. The image acquisition provides information of the decline in H_1 and H_2 with time, where H_1 and H_2 are heights of suspension column at levels L_1 and L_2 respectively as shown in figure 6.1.

The liquid pressures P_1 and P_2 in the flowing systems are measured by differential transducers (Omega; ± 1 psi) attached across holes in the channel wall at the level L_1 and level L_2; reported pressures are thus relative to atmospheric. We confirm experimentally that the extent of significant non-axial flow above the contraction

level is $\approx 3w$: L_2, well above this zone, is in a unidirectional flow region. This result is also verified based on the numerical analysis of suspension flows through contraction geometry [85]. For suspension flows, liquid pressure alone, rather than that exerted by both particles and fluid, is measured by placing a mesh across each hole to retain the particles, as previously shown [32].

Experimental protocol: The suspension is poured carefully into the channel to avoid bubble capture. During this filling operation, a bottom plate restricts outflow. The suspension is poured into the channel to a level 15 cm above the contraction. Then the bottom plate restricting outflow is removed and the pressure and image data is recorded as the suspension flows through the contraction geometry. The effluent material collected at the exit as the suspension column height drops about 7 cm is weighed; the particles are recovered by thorough washing and drying, then weighed separately to obtain the outlet concentration. This measurement gives us information about the self-filtration. Unless mentioned, the upper surface of the suspension is open to the atmosphere. Experiments with additional driving force use a closely-fitted weighted piston placed on the upper surface of the mixture.

We first present an experiment to illustrate different internal stress states within the *mixture* under different flow restrictions. Figure 6.2 shows the liquid pressure response measured at L_1 and L_2 for $\zeta = 1/6$ and particle volume fraction $\phi = 0.58$ for the initial head level of 15 cm. Case (i) represents a condition where the flow is completely restricted by the bottom plate; the liquid pressure at a point is equal to static fluid head above it. In case (ii), the particle flow is restricted by a mesh at the bottom while the liquid phase flows under gravity, yielding Darcy flow through a column of particles; from liquid pressure measurements, we estimate $\frac{dP}{dH} \approx 50$ Pa/cm above the contraction. Finally, in case (iii), the suspension is allowed to flow under gravity without any restriction. The significant decrease in the liquid pressure from

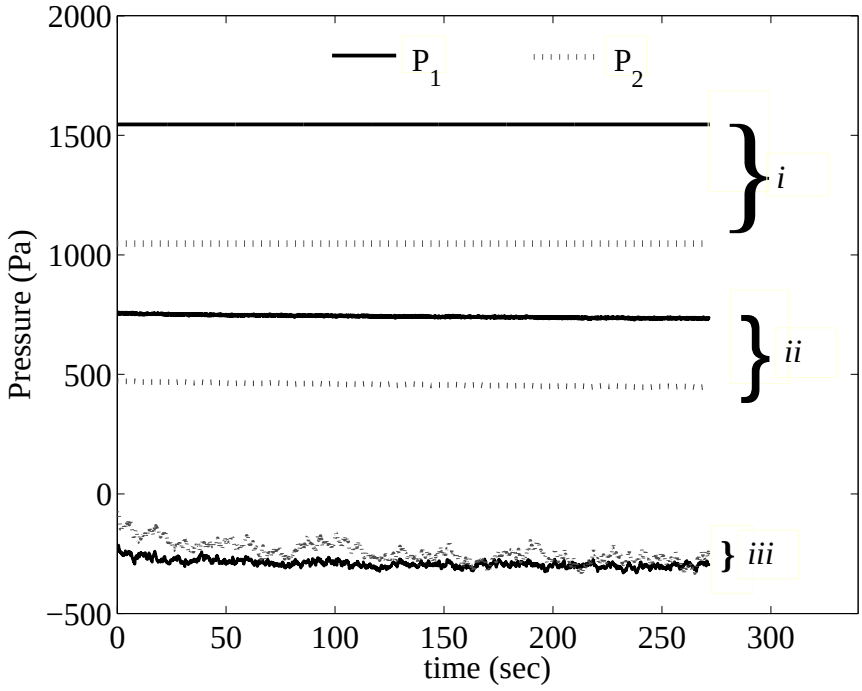

Figure 6.2: Liquid differential pressure response for $\zeta = 1/6$ and $\phi = 0.58$, case (i): static condition; case (ii): mesh at the bottom which only lets liquid phase flow; case (iii): suspension flow. The drop of the upper surface, from 15 cm at time $t = 0$, in cases (ii) and (iii) is only a few mm.

case (ii) to case (iii), notably dropping the local absolute pressure below atmospheric, is indicative of a considerable change in the internal stress state. The decrease is consistent with the idea of the suction pressure $\Pi_{liq} = -\Pi(\dot{\gamma}, \phi)$ [32] generated in the suspending liquid phase due to motion of the particles. This flow-induced suction pressure is a key parameter used to describe the flow behavior in the present system. In the following work, we focus on the gravity driven suspension flow without any restriction at the end of the contraction similar to case (iii).

6.3 Experimental results

Figure 6.3 shows P_1 vs. H_1 and P_2 vs. H_2 for flow of different materials through the contraction, where H_1 and H_2 are heights of liquid (or suspension) column at respective measurement levels as shown in figure 6.1. For the pure liquid ($\phi = 0$) flow, the pressures P_1 and P_2 are slightly below the corresponding static heads $\rho g H_1$ and $\rho g H_2$ (indicated by solid lines), as a result of viscous pressure losses accounted as $\Delta P_1 = \rho g H_1 - P_1$, as labeled in figure 6.3a, and $\Delta P_2 = \rho g H_2 - P_2$. Figure 6.3 shows that, for pure liquids X and Y differing in viscosity by a factor of over five, the pressure (and hence ΔP) dependence on fluid-column height is identical. In contrast, suspension flows are characterized by reduction in liquid pressures, differing with volume fraction; this reduction for a suspension of $\phi = 0.5$ is labeled as Π_1 in figure 6.3a to indicate the relationship to particle pressure which we develop later.

We note that the equivalence of pressure dependence for different viscosity pure liquids is a consequence of hydrodynamic linearity under the Stokes-flow conditions. The viscous loss ΔP_1 (or ΔP_2) is proportional to the shear stress $\eta_s \dot{\gamma}$. The shear rate may be written as $\dot{\gamma} = K(\mathbf{x})(\rho g H_1/\eta_s)$, where $K(\mathbf{x})$ accounts for spatial variation in shear rate due to the contraction; the liquid column head $\rho g H_1$ above the contraction is the driving force for flow, and the resistance to flow scales with η_s. Thus $\Delta P_1 \sim \eta_s \dot{\gamma} \sim \rho g H_1$, confirming independence of viscous losses on material viscosity. The experimental data for both liquids yields $\Delta P_1 = 0.16 \rho g H_1$, and $\Delta P_2 = 0.03 \rho g H_1$.

We now assess the liquid pressure for flow of suspensions at solid fraction $\phi = 0.50$, 0.52, 0.55, and 0.58, with $\eta_f = 0.30$ Pa.s (in one case η_f=0.9 Pa.s). The suspension effective viscosity satisfies $\eta_s = \eta_s^*(\phi)\eta_f$ where $\eta_s^* \sim (1 - \phi/\phi_{max})^{-2}$, with $\phi_{max} \approx 0.6$ the maximum packing fraction. Recall that the liquid pressure *alone* is obtained by placing screens across holes at L_1 and L_2 [32], and that the pressure drop due to

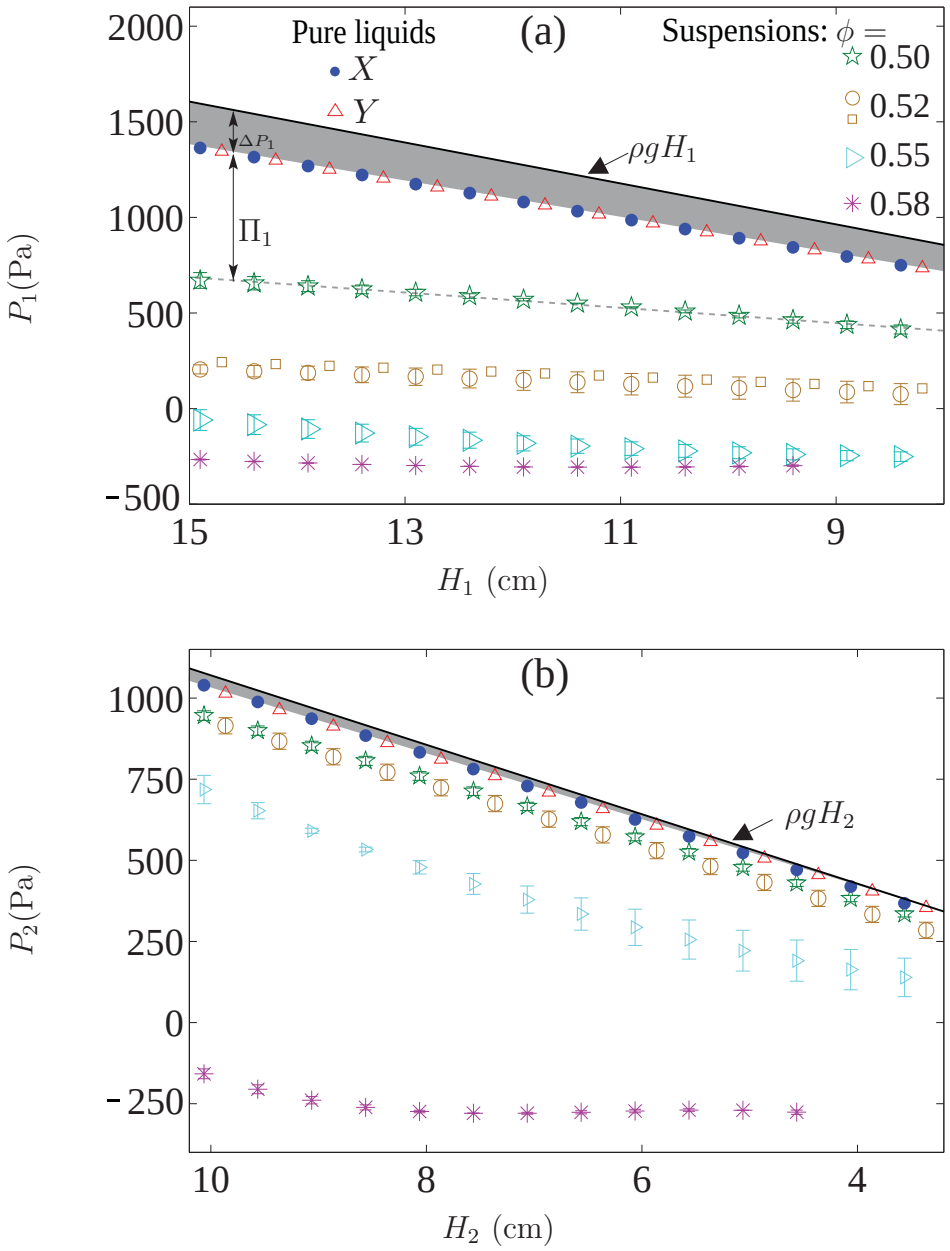

Figure 6.3: (color online) Liquid pressure of flowing systems measured (a) at L_1 in the beginning of the contraction; (b) at L_2, 5 cm vertically above L_1, plotted against fluid column height at each measurement level. The legend in (b) applies also to (a). Viscosities are, for liquid X 36.5 Pa.s and for liquid Y 7 Pa.s; For suspensions, the suspending fluid has $\eta_f = 0.3$ Pa.s, except for one set of data at P_1 for $\phi = 0.52$, where $\eta_f = 0.9$ Pa.s (open squares).

viscous losses is independent of the viscosity η_s and depends (for fixed density) only on fluid column height H_1. Yet figure 6.3 shows that the measured liquid pressure values for a suspension decrease relative to those found for the pure liquid flows, and the decrease becomes more pronounced with increasing ϕ. The striking conclusion is that the additional decrease in liquid-phase pressures P_1 and P_2 observed for suspensions must be due to another physical process unique to a two-phase flow.

As noted above, experiments [32] and simulations [31] have shown that uniform shearing in suspensions generates suction pressure in the suspending liquid $\Pi_{liq} = -\Pi(\dot{\gamma}, \phi)$, which is accounted here as

$$P_1 = \rho g H_1 - \Delta P_1 - \Pi_1, \qquad P_2 = \rho g H_2 - \Delta P_2 - \Pi_2. \tag{6.1}$$

Because ΔP_1 and ΔP_2 were previously evaluated and independent of viscosity, we are able to determine Π_1 and Π_2 separately as a function of fluid column height.

The measurement of self-filtration, where effluent concentration ϕ^m_{out} is below the input ϕ_{in}, is shown in figure 6.4. For $\phi_{in} \geq 0.55$, we find $\phi^m_{out} \approx 0.528 \pm 0.003$. Also, ϕ^m_{out} remains unchanged as the suspension column drops from $H_1 = 15$ cm to 8 cm. As a result of mass conservation and dilution of the effluent, the top of the column would become dry (as we observed in early experiments), unless a layer of a few mm depth of pure liquid is added on top of the suspension, and we follow this practice. Similar filtration behavior for colloidal systems was observed by [73], where it was suggested that colloidal jamming or flow instabilities are necessary to induce self-filtration. On the contrary, we observe this phenomena under steady flow.

6.4 Self-filtration model

We now propose a mechanistic model for self-filtration invoking particle pressure, and check its consistency with our experimental results. Constitutive modeling [34] and simulation at uniform shear and ϕ [18, 31] have shown that particle pressure may be expressed as $\Pi = \eta_n \dot{\gamma}$ for non-Brownian suspensions, where $\eta_n = \eta_n^*(\phi)\eta_f$ is the suspension "normal stress viscosity" modeled as $\eta_n^* \sim 0.75(\phi/\phi_{max})^2(1-\phi/\phi_{max})^{-2}$. Combining the local rheology $\Pi \sim \eta_n \dot{\gamma}$ with dependence of the shear rate on driving head, $\dot{\gamma} = K(\mathbf{x})(\rho g H_1/\eta_s)$,

$$\frac{\Pi}{\rho g H_1} \approx K(\mathbf{x}) q(\phi), \tag{6.2}$$

where $q(\phi) = \eta_n/\eta_s$ is the ratio of normal to shear stress, (or inverse of friction coefficient in granular rheology) which increases with ϕ and is independent of η_f [34] [21]. This formulation leads to the remarkable implication that for a fixed configuration and ϕ in gravity-driven flow, particle pressure is independent of the suspending liquid viscosity. We confirm this experimentally, as illustrated by the two identical curves for P_1 (within error bar) in figure 6.3a at $\phi = 0.52$, for $\eta_f = 0.3$ or 0.9 Pa.s. A second implication is that at a given point in the channel the ratio $\Pi/\rho g H_1$ is independent of H_1 and increases sharply with ϕ. At the positions of the pressure sensors, we plot $\Pi_1/\rho g H_1$ and $\Pi_2/\rho g H_1$ averaged over $8 < H_1 < 15$ cm for experiments with different ϕ_{in} (figure 6.4 inset). The small error bars confirm independence of H_1 and no considerable change in local ϕ over any experiment. The sharp rise in $\Pi_2/\rho g H_1$ with ϕ_{in} is expected, but given the constitutive modeling, the flattening of $\Pi_1/\rho g H_1$ suggests that ϕ at the contraction is reduced relative to ϕ_{in}, and is essentially unchanged for $\phi_{in} \geq 0.55$. This interpretation of dilation at the contraction agrees with flattening of measured outlet concentration ϕ_{out}^m for $\phi_{in} \geq 0.55$.

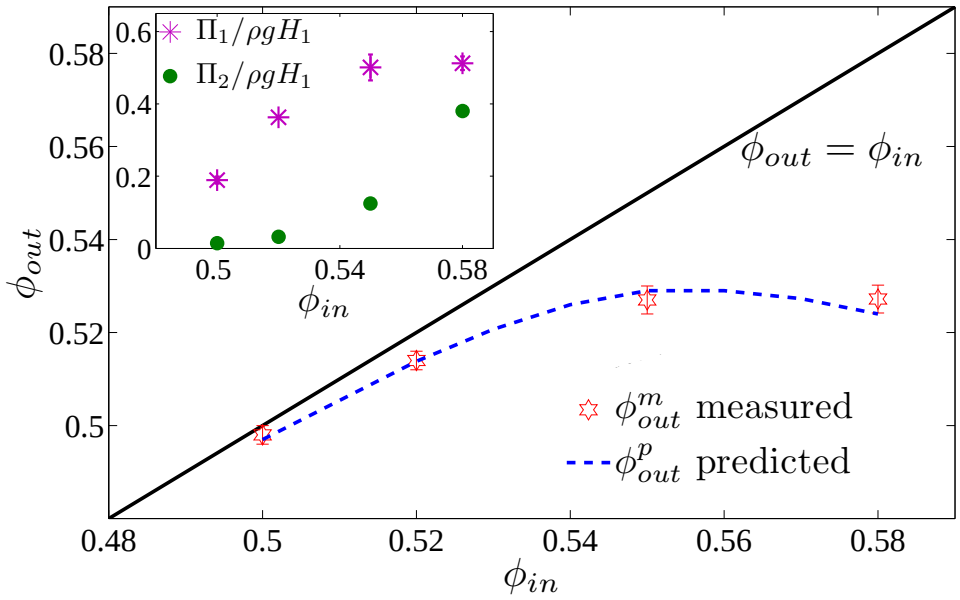

Figure 6.4: (color online) Comparison of the measured and predicted outlet particle volume fractions, ϕ^m_{out} and ϕ^p_{out} for contraction geometry $w/W = 1/6$; the inset shows $\Pi_1/\rho g H_1$ and $\Pi_2/\rho g H_1$ plotted against input particle concentration ϕ_{in}.

To address the basis of the observed dilation, we now assume that the fluid pressure variation between contraction and bulk regions induces flow of liquid relative to particles, similar to Darcy flow, sucking liquid toward the contraction. This suction force can be estimated as $[\Pi_1 - \Pi_2]_{\phi=\phi_{in}}$. A direct measure is difficult, as Π_1 is affected by dilation at the contraction. We reformulate the suction force in terms of Π_2 using equation (6.2),

$$[\Pi_1 - \Pi_2]_{\phi=\phi_{in}} = (K_1/K_2 - 1)\Pi_2, \tag{6.3}$$

where we recall that K represents the spatial dependence of the shear rate. The flow of liquid relative to particles $\Delta V = V_l - V_p$ is stated as

$$\frac{\Delta V}{V_p} \sim \frac{\Pi_2/\eta_s}{\rho g H_1/\eta_s} \sim \frac{\Pi_2}{\rho g H_1}. \tag{6.4}$$

As $\Pi_2/\rho g H_1$ is independent of H_1, equation (6.4) implies steady dilution, consistent with the experimental observation. Writing a conservation equation for the particles and incorporating equation (6.4) yields

$$\phi_{out} = \frac{\phi_{in} V_p}{\phi_{in} V_p + (1-\phi_{in}) V_l} = \frac{\phi_{in}}{1 + A\frac{\Pi_2}{\rho g H_1}(1-\phi_{in})}. \tag{6.5}$$

Using the experimental measurement of $\Pi_2/\rho g H_1$ and ϕ_{out} from figure 6.4, we obtain the dimensionless $A = 0.34 \pm 0.04$. With this value of A and a quadratic interpolation of $\Pi_2/\rho g H_1$ data in figure 6.4 inset, the prediction of the effluent concentration is in satisfactory agreement with the experimental data (figure 6.4); the downward curvature is an artefact of the quadratic fit.

Considering the spatial dependence of the shear rate $\dot{\gamma} = K(\mathbf{x})(\rho g H_1/\eta_s)$, one would expect $K_1/K_2 = 6$ in the present geometry where the ratio of the contraction channel $w/W = 1/6$. However, for $\phi = 0.50$ and 0.52, where the observed dilation is small, equation (6.2) suggests $K_1/K_2 \approx \Pi_1/\Pi_2 \approx 13$. This larger value shows that K_1/K_2 is influenced both by the variation in shear rate and change in flow type from pure shear flow to extensional flow at the contraction. We also conducted experiments with smaller particles ($150 - 250\mu$m dia.) at $\phi = 0.58$. The pressure responses P_1 and P_2 as well as the effluent concentration ($\phi^m_{out} \approx 0.53$) remains unaffected by the particle size for the studied range.

6.5 Oscillatory flow under added load

We now consider flow under additional load supplied by a 100 g piston added to the top of the mixture. The weight is equivalent to 2 kPa additional pressure. Images are captured using a high magnification lens (Sigma DG HSM) with wide field of

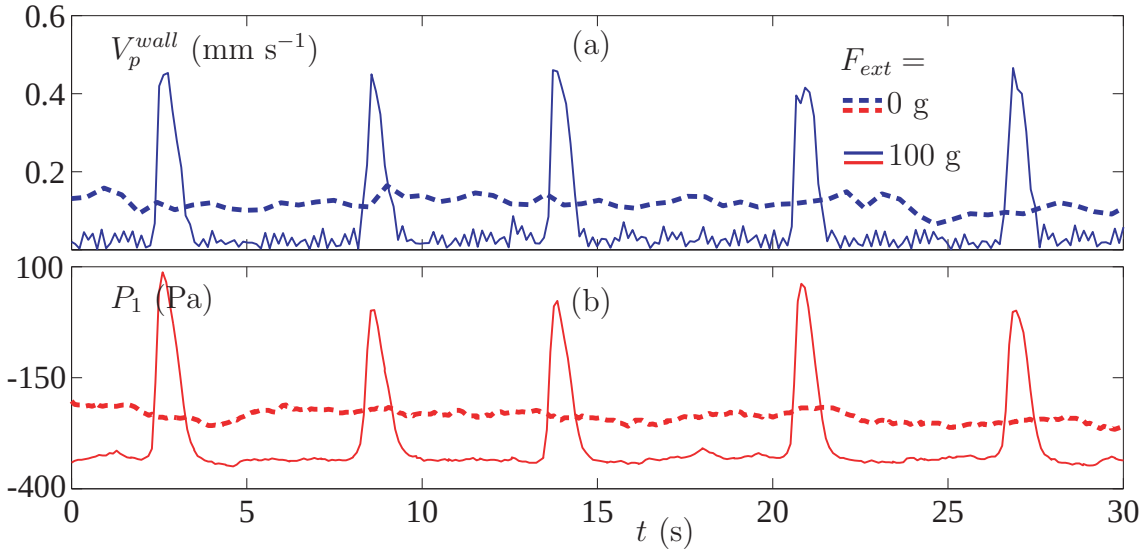

Figure 6.5: (color online) (a) velocity, V, and (b) liquid pressure, P_1, at the contraction for $\phi = 0.58$ and $w/W = 1/6$: dashed lines correspond to no external force; solid lines correspond to a weighted piston of 100 g load.

view (1.5 cm $\times$ 2 cm) focused on the contraction, illuminated by white light. Particle tracking velocimetry (PTV) is used to obtain the average particle speed along the wall. The bulk flow determined from the decline of the suspension column is 4-5 times the observed near wall motion for both steady and oscillatory flows. In the contraction of $w/W = 1/6$, at $\phi = \phi_{crit} \approx 0.58$ with the weighted piston, PTV shows that the flow alternates between 'fast' and 'slow' motions with a surprising periodicity as shown in figure 6.5. The oscillations are absent below a particular threshold load as seen in earlier work [80], but the oscillation frequency here decreases with added load, contrary to that study. Robustness of periodic flow to changes in geometry, suspending liquid viscosity and piston weight is described in chapter 7 but here we focus on $\phi = 0.58$, $w/W = 1/6$ and added piston load of 100 g. Under this condition, the measured effluent concentration is $\phi_{out}^m = 0.527 \pm 0.003$ with the stated variance based on multiple experimental trials. Thus, we demonstrate that the 'self-filtration' occurs in both steady and oscillatory flow conditions in the present geometry. Figure

6.5 shows that the particle speed in slow motion of the alternating flow is lower than with no external force. This suggests the weighted piston makes contact with particles at the upper surface, activating a granular network which supports most of the piston weight. Slow creep of the deforming granular network causes a decrease in liquid pressure P_1. When the network abruptly breaks, as indicated by the faster motion, the internal stress in the particle phase is released and the liquid pressure goes up simultaneously (figure 6.5). Thus, dilational motion near the contraction in the slow regime ultimately leads to breakage of the granular network. As the diluted batch passes through the contraction, the granular network is reestablished and begins again to creep, thus leading to periodic flow variation. Similar correlation between flow speed and pore pressure is observed in avalanching flows [81].

6.6 Conclusion

We conclude that in concentrated suspension flow in a contraction geometry, the change in shear rate at the contraction induces a spatially varying pressure field in the liquid phase, with the pressure reduced well below the value expected due to viscous losses. In the same flow, we observe self-filtration with a reduced outlet solid concentration relative to the imposed inlet concentration. We have related the reduction in the liquid pressure field to particle pressure, and proposed a model which rationalizes the self-filtration phenomenon. When driving the system with a weighted piston at $\phi_{crit} \approx 0.58$, the flow shows consistent periodic oscillations where fast and slow motion of the suspension correspond, respectively, to low and high internal stress states of the particle phase. The same type of coupling involving dilation and failure of the solid network seems responsible for this striking phenomenon. Note that the liquid pressure in the porous medium state of the mixture is equivalent to a pore

pressure in granular and soil mechanics [86]. We conclude that the concept of pore pressure is directly related to shear-induced particle pressure, Π, in suspensions, which has been established both as a nonequilibrium continuation of osmotic pressure [31] and a general drive toward particle phase dilation [32].

Chapter 7

Periodic velocity oscillations in concentrated suspension flow

7.1 Introduction

Abrupt shear thickening or jamming in dense suspensions flows is of importance to many geophysical flows such as sudden, larger movements of the earth's crust along the faults filled with slurries. This phenomenon is also observed in several industrial operations, such as blocking of transport pipes or mixer blades. Jamming can be briefly described as conversion of flowing suspension system into 'solid-like' system by imposed stress or strain leading to a dynamical arrest. Cassar *et al.* [87] studied submarine granular avalanches to probe the role of interstitial fluid pressure in avalanche dynamics and instability development. Bertrand *et al.* [71] observed conversion of a concentrated non-Brownian suspension into persisting paste when subjected to moderate shear. Lootens *et al.* [72] investigated 'giant stress fluctuations' in dense colloidal suspensions when the imposed shear rate approached a transition value. Isa *et al.* [80] observed confinement-induced flow oscillations in their study of

A part of this chapter is published as *Extreme velocity fluctuations: transient jamming in concentrated suspension flow*, S. D. Kulkarni, B. Metzger and J. F. Morris, AIP Conf. Proc. **1027**, 683 (2008)

micro-fluidic channel flow of concentrated colloidal suspensions. In the work closely related in terms of geometry and solid fraction in our study, Haw [73] probed erratic fluctuations in the flow-speed in pressure driven flow of dense colloidal suspensions through a contraction geometry.

The other remarkable phenomena observed in the dense systems, self-filtration, describes the ability to generate a spatial variation in the material concentration under various flow conditions. Chapter 6 provides the literature available in this area. In chapter 6, we studied gravity-driven flow of non-Brownian concentrated suspensions (solid volume fraction $\phi > 0.50$) through a channel contraction. We observed the self-filtration, where the effluent material through the contraction has a consistently lower solid fraction than the input suspension. The abrupt change in the flow area at the contraction forms distinct shear-rate regions having different fluid pressures, which are related to the concept of particle pressure. We demonstrated a model involving particle pressure variation coupled to a Darcy-like behavior for the fluid that captures the phenomenon of self-filtration. Note that, in the above study, the material which is under no external load, flows steadily. We briefly discussed a representative case of oscillatory flow alternating between fast and slow motions, when an external load is added on the suspension. Our goal here is to illustrate the robustness of this oscillatory flow behavior and study its dependence on changes in applied additional load, particle concentration, suspending liquid viscosity and the particle size. We also present the self-filtration behavior observed in these oscillatory flows. The system's pressure response is studied to understand the noted flow behavior. The experimental procedure and data acquisition method are described in the following section, followed by key results in section 7.3.

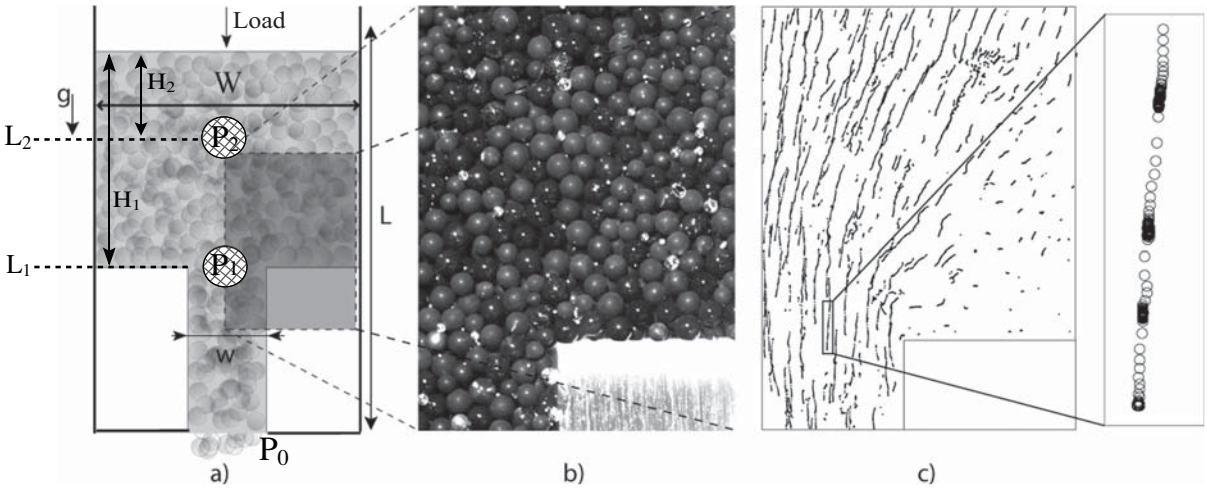

Figure 7.1: a) Front view sketch of the experimental set up. b) Sample image near contraction. c) Particle trajectories using Particle Tracking Velocimetry.

7.2 Experiment

In the present study, we use Particle Tracking Velocimetry technique to measure the near-wall particle speed at the contraction. The experimental set-up is same as described in chapter 6, thus the description here is brief.

Materials & apparatus: The suspensions are prepared by adding spherical polystyrene particles (Maxi-Blast Inc.) typically of size 380-500 μm diameter (except in one case with $150 - 250\mu$m dia. particles) to UCON oil (Dow Chemical). The density of UCON oil is 1.05 g/cm^3 at 25°, very close to that of polystyrene particles. The flow is through a rectangular channel (constructed of acrylic) as shown in figure 7.1a. The length (L), width (W) and depth of the rectangular channel are 20 cm, 2.5 cm and 2 cm, respectively. Two identical rectangular blocks of length 4 cm, depth 2 cm (equalling the channel depth) and of width yielding the ratio of the contraction channel width to that of original channel $w/W = 1/6$, are inserted symmetrically along the wall of the original channel (figure 7.1a).

Data acquisition & analysis: The Particle Tracking Velocimetry technique is

briefly described as follows. The flow is imaged by a CCD camera (Basler $A1021$) along an axis orthogonal to the channel wall. Images are captured using a high magnification lens (Sigma DG HSM) with wide field of view (11 mm X 16 mm) focused on the area near the contraction. The field of view is illuminated by a white light source. The light source is adjusted so that each particle in the field of view has a single bright reflecting spot (figure 7.1b). Images taken at a specified frequency of 5-15 frames/second are treated later to identify the bright spots (reflections) in the image, by selecting a threshold for intensity using $ImageJ$ software. Spurious reflections due to bubbles and dust are minimized by choosing bright spots in the range of circularity and size determined to be representative of the particle reflections. The positions of the bright spots in the successive images are then used to track the particles (figure 7.1c) and to obtain their velocities; a representative trajectory in figure 7.1c is highlighted.

Differential pressure transducers (Omega; $\pm$ 1 psi) are used to measure the liquid pressure response in the flowing systems; hence the reported pressures are relative to atmospheric. The liquid pressures P_1 and P_2 are measured across holes in the channel wall at the contraction (level L_1) and 5 cm above (level L_2) respectively. As noted in chapter 6, the liquid pressure in the suspension flows is measured by placing a mesh across each hole to retain the particles.

Experimental protocol: When the suspension is poured into the channel, a bottom plate blocks the outflow. The suspension is filled to a level 15 cm above the contraction. The additional load is provided by adding weights to the closely fitting piston on the top of the mixture. Each 50 g weight is equivalent to 1 kPa additional pressure. After adding the external load, the bottom plate restricting outflow is removed. The pressure and image data is recorded as the suspension flows through the contraction geometry. The material exiting the geometry (effluent) is collected as

the suspension column height drops by about 7 cm. The effluent is weighed and then the particles in the effluent are recovered by washing thoroughly with soap and water. The dried particles are weighed separately and compared with the effluent weight to obtain the effluent concentration.

Here, results are discussed for particle volume fraction $\phi \geq 0.55$; where the flow becomes periodic under external load. Experiments to study the periodicity for varying driving pressure (solid and liquid head), particle concentration, viscosity of suspending liquid and particle size are described. The external solid load is altered from 25 g to 600 g. The viscosity of the suspending liquid (η_f) is varied from 150 - 900 cP at 25° using mixtures of UCON 50-HB-660 and 75-H-90000. Inertia is negligible, i.e. $Re_p = \frac{\rho U a}{\eta} \ll 1$, where U is average particle speed, a is the radius of the particle, and ρ and η are the fluid density and viscosity, respectively. The ratio of smaller channel width to the average particle diameter is defined as β, which varied by changing the particle size. The contraction ratio w/W is denoted as ζ.

7.3 Results and discussion

When no blocks are inserted in the rectangular channel (i.e. $\zeta = 1$), the suspension flows steadily both under its own weight and under additional load (solid and liquid head) for the entire range of system parameters studied.

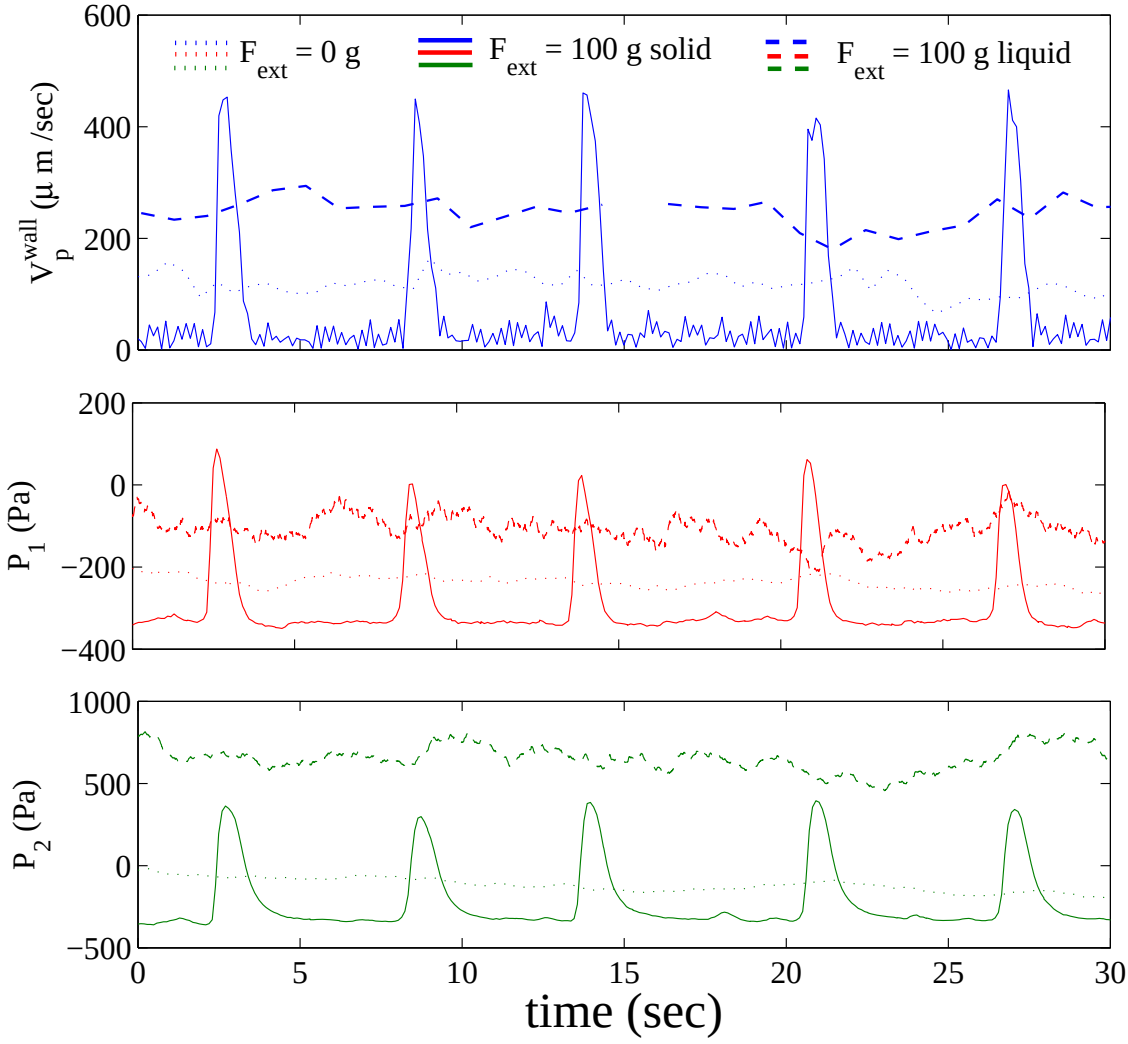

Figure 7.2: (a) particle speed V_p^{wall} in the contraction channel, (b) liquid pressure P_1 measured at the contraction (c) and liquid pressure P_2 measured 5 cm above the contraction in the bulk, at $\phi = 0.58$ and $w/W = 1/6$: dotted lines correspond to no external force $F_{ext} = 0$ gm; solid lines correspond to a weighted piston of 100 g applied to the top surface of the mixture; dashed lines correspond to a liquid head of 100 g on the top of the mixture.

7.3.1 Applied solid weight vs. liquid head

In this subsection, the flow behavior is studied for $\zeta = 1/6$ and $\eta_f = 270$ cP under different types of applied loads at $\phi = 0.58$. The effluent material concentration, $\phi^m_{out} \approx 0.53 \pm 0.003$, remains independent of the applied load conditions indicating very robust filtration mechanism which probably solely depends on the geometry of the system. Under its own weight, the flow is smooth under the noted suspension head of 15 cm above the contraction. When additional solid weight of 100 g is applied, the flow becomes periodic (figure 7.2) with cycles of alternating 'fast' and 'slow' motions (the ratio of fast to slow motion is a factor of ten or greater) exhibiting a well-defined periodicity. Note that the speed in the 'slow' motion of periodicity is lower than that observed in the smooth flow with no external load (figure 7.2a). It clearly indicates that the added load has introduced strong networking in the material which causes decrease in the flow speed for the 'slow' motion. The networking in this system may be compared with a vertical column of dry granular particles which shows Janssen effect under static and dynamic conditions [88]. The Janssen effect describes that, in the column of granular particles, the effective weight experienced at the bottom of the column is lower that the actual weight of the material. The effective weight at the bottom reaches a exponential limit as height of the column increases, this happens due to the shielding effect of contact forces between particles that redirect the weight towards the side walls. In the present study, the particle network formed under the external load breaks periodically. We interpret that the dilational motion caused by the relative flow of the suspending liquid near the contraction in the 'slow' regime ultimately leads to breakage of the particle network. As the diluted batch passes through the contraction, the particle network is reestablished and begins again to creep, thus leading to periodic flow variation.

Figure 7.2 shows that the liquid pressure responses P_1 and P_2 are correlated to the 'fast' and 'slow' motions of the periodic flow. The liquid pressure information in steady and oscillatory flows is analyzed as follows. In chapter 6, for the flow without load, we formulated the liquid pressure at the contraction as

$$P_1{}^{NL} = \rho g H_1 - \Delta P_1 - \Pi_1(\dot{\gamma}, \phi), \tag{7.1}$$

where H_1 is the height of the suspension (or liquid) column at the contraction level (see figure 7.1a) and the particle pressure $\Pi(\dot{\gamma}, \phi)$ quantifies tendency of dispersed phase to spread under shear which induces equal but opposite (and hence, suction) pressure in the suspending liquid as demonstrated experimentally by Deboeuf *et al.* [32]. We confirmed that the viscous losses are independent of the material viscosity, $\Delta P_1 \sim \eta_s \dot{\gamma} \sim \rho g H_1$.

Now, when the external solid load is added, as noted above for the 'slow' regime, strong networking is introduced in the flow which reduces the flow speed. The addition of the solid load provides a non-viscous stress transmission mechanism which distributes the load without motion in the particle network. For this 'slow' motion, the liquid pressure response at the contraction may be restated as

$$P_1{}^{slow} = \rho g H_1 - \Pi_1{}^{slow} - \Delta P_1{}^{slow}, \tag{7.2}$$

where H_1, the head experienced by the liquid phase at the contraction, is unchanged (when compared to no external load condition) as the added load is considered to be carried by the particle network. Note that the Janssen effect is applicable to the particle phase only; for the continuous liquid phase the contribution of the liquid head H_1 would remain unaffected by the networking of particles. The particle pressure

under external solid load, ${\Pi_1}^{slow}$, remains unaffected by the magnitude of the added load and is described in detail in the following subsection. The pressure drop under external solid load, ${\Delta P_1}^{slow}$, will have two contributions; first is from the viscous losses experienced because of the overall flow of the material (similar to flow for no external load) and the other contribution is from the additional loss experienced by the liquid phase when it passed through the stronger particle network established under the load (Darcy flow losses). The additional Darcy losses may explain lower values of ${P_1}^{slow}$ as compared to ${P_1}^{NL}$ (see figure 7.2b).

In the 'fast' motion of periodicity under external solid load, the network breaks, the load acts on both solid and liquid phases; the additional head would contribute to increase in the liquid pressure P_1 as observed in the experiments, where ${P_1}^{fast}$ grows sharply with the particle speed as seen in figure 7.2b. The same interpretation is applicable for the liquid pressure P_2 measured 5 cm above the contraction (figure 7.2c).

The flow behavior under added liquid head is discussed below. Under additional liquid head of 100 g (equivalent to the corresponding added solid head), the flow speed and corresponding pressure responses P_1 and P_2 are significantly higher compared to the no external load condition. The flow remains uniform and no oscillations are observed as shown in figure 7.2. Thus, there is striking difference in the flow behavior for the two methods of applying load to dense suspensions. Note that when the solid load is applied, the suspension experiences a rigid solid surface at the top, while, when the liquid head is added, the suspension experiences a deformable liquid surface on the top. Thus, only the rigid interface (provided by the solid load) can distribute the load exclusively to the particle phase, which introduces non-viscous contact forces between the particles. The contact network forms and breaks alternatively, giving rise to the observed phenomenon of periodicity.

Figure 7.2a shows that the particle speed under 100 g liquid head is smaller than the peak speed in the 'fast' motion when 100 g solid head is added; the reason for this difference is not established.

7.3.2 Progressive addition of solid loads

In this subsection, the flow behavior is studied for $\zeta = 1/6$ and $\eta_f = 270$ cP under varying external solid loads applied to the suspensions at $\phi = 0.55$ and $\phi = 0.58$. The measured effluent concentration remains unaffected by the variations in the added load ($\phi^m_{out} \approx 0.53 \pm 0.003$), confirming its robust behavior. Figure 7.3a provides time period of oscillations vs. added solid load (L) for experiments at $\phi = 0.55$ and $\phi = 0.58$. For $L < 200$ g, the change in the period remains small as the load increases. However, for $L > 200$ g, the period rises sharply with the external load. The rise in the period mostly arises from the increase in duration of the 'slow' regime as seen in figure 7.3b. This sharp rise suggests that the added load contributes to the stiffness of the network, increasing the time required for its breakage. We also find that the period under $\phi = 0.58$ is significantly larger than that under $\phi = 0.55$. Thus, the initial ϕ also influences the stiffness of the network; higher the ϕ, stronger the network, which is intuitive.

Figure 7.3b shows the liquid pressure responses P_1 and P_2 as the external solid load is added in increments from 25 g to 400 g ($\phi = 0.58$). We observe that there is a threshold external load above which system shows periodic flow behavior. For the present conditions of material and geometry, the threshold load is $\approx$ 100 g. Interestingly, once we enter in the periodic flow regime, P_1 and P_2 in the 'slow' motion (${P_1}^{slow}$ and ${P_2}^{slow}$) remain mostly unchanged irrespective of the added load. This behavior could be readily explained as follows. Prasad & Kytomaa [23] mentioned

that, in case of high particle volume fractions, when normal forces are applied at low strain rates, the shear stress remains independent of the strain rate. They call this regime as 'quasi-static' where short range frictional interactions between the particles are dominant. In this quasi-static regime, the ratio of normal to shear stresses (η_n/η_s) remains independent of applied normal forces, which is a key point in our analysis.

From equation (7.2), the column head H_1 and ${\Pi_1}^{slow}$ contributions decide the behavior of ${P_1}^{slow}$. In the 'slow' motion under varying load, we consider that the head experienced by the liquid phase at the contraction is same as the suspension (or liquid) column height H_1 as the entire external load is carried by the particle network. Constitutive modeling [34] and simulation at uniform shear and ϕ [18, 31] have shown that particle pressure may be expressed as $\Pi = \eta_n\dot{\gamma}$ for non-Brownian suspensions. Combining the local rheology $\Pi \sim \eta_n\dot{\gamma}$ with dependence of the shear rate on the material viscosity in the gravity driven flow, $\dot{\gamma} \propto (1/\eta_s)$, the particle pressure could be written as $\Pi \propto \eta_n\dot{\gamma} \propto \eta_n/\eta_s$. Now, in the 'slow' motion under external load, we enter the 'quasi-static' regime [23] and hence (η_n/η_s) or ${\Pi_1}^{slow}$ would become independent of the external load. Thus, in the 'slow' regime, both H_1 and ${\Pi_1}^{slow}$ remain independent of the added load leading to the unchanged values observed for ${P_1}^{slow}$ and ${P_2}^{slow}$. Similar behavior is observed for $\phi = 0.55$. On the other hand, in the 'fast' regime, the particle network breaks, the load 'acts' on the suspension (on both phases), and the flow speed and the liquid pressures are influenced by the magnitude of the load as seen in figure 7.3b.

(a)

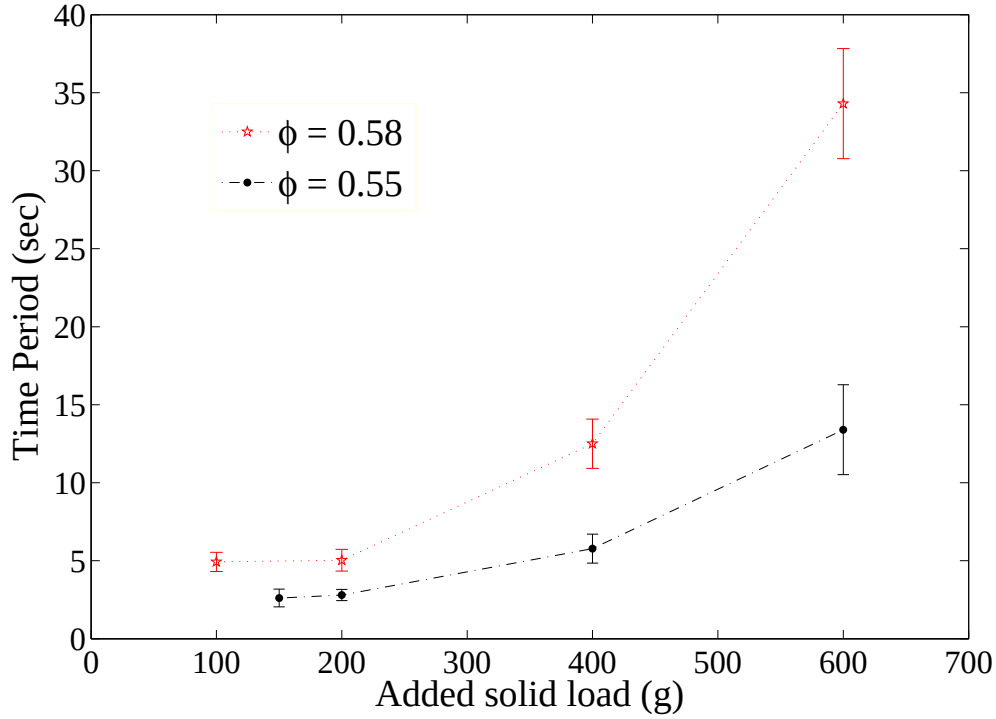

(b)

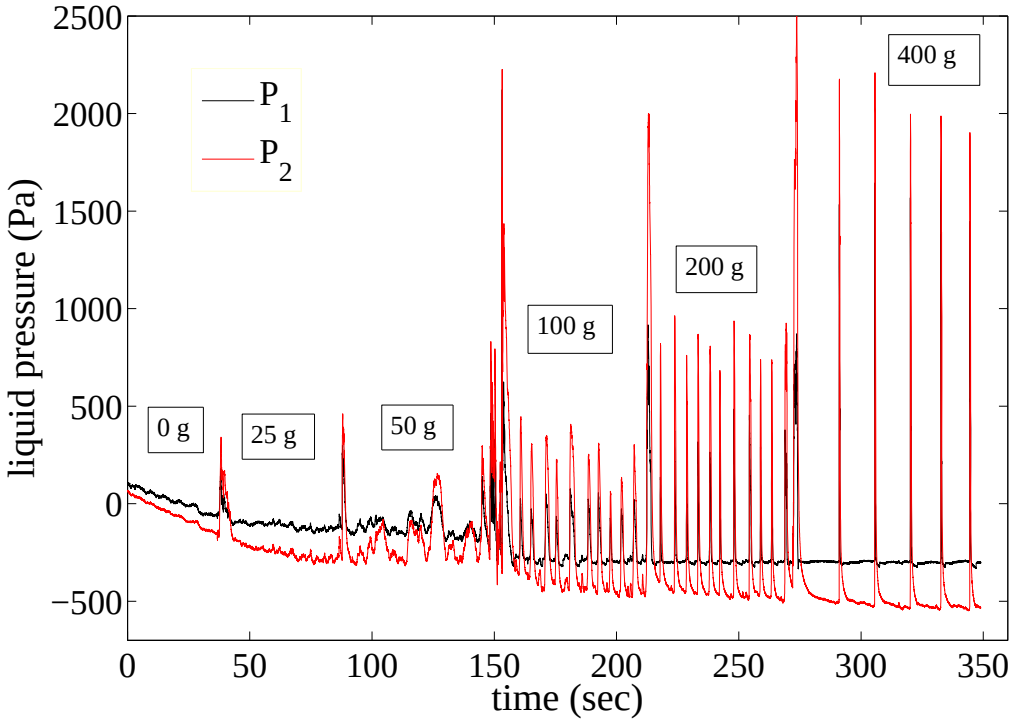

Figure 7.3: For $\zeta = 1/6$ and $\eta_f = 270$ cP (a) time period of oscillations vs. added solid load (L) for experiments at $\phi = 0.55$ and $\phi = 0.58$; (b) pressure response as the external solid load is added in increments at $\phi = 0.58$.

7.3.3 Effect of solvent viscosity

In this subsection, the flow behavior is studied for $\zeta = 1/6$ and $\phi = 0.58$ for different solvent viscosities η_f. The viscosity of the suspending liquid varies from 150 - 900 cP using mixtures of UCON 50-HB-660 and 75-H-90000. We find that the effluent concentration $\phi^m_{out} \approx 0.53$ remains unaffected by the change in suspending liquid viscosity. As both the relative flow of liquid (which causes dilution) and the average suspension speed scale with η_f, the effluent concentration is expected to be unchanged when η_f is varied as observed in the experiments.

Figure 7.4 shows the particle speed and liquid pressure P_1 data at $\phi = 0.58$ for $\eta_f = 270$ cP and $\eta_f = 480$ cP under steady and oscillatory flow conditions. Under no external load, the flow speed of the smooth flow is approximately twice for $\eta_f = 270$ cP as compared to that for $\eta_f = 480$ cP, which is evident as $\dot{\gamma} \propto (1/\eta_f)$ in the gravity driven flow. As seen in figure 7.4a, the time period of oscillations under the external load increases significantly with η_f, which is contributed by increase in both 'slow' and 'fast' motions. The flow speed in the oscillatory motion is also affected by the variation in η_f. Although the variations in speed for the 'slow' regime are less clear because of the limitations in the resolution capability of the present visualization set-up, the 'fast' regime speed has a noticeable reduction ($\approx$ by a factor of 2) as we go from $\eta_f = 270$ cP to $\eta_f = 480$ cP.

Although the flow speed varies with η_f, figure 7.4b shows that the magnitude of the liquid pressure P_1 remains unaffected by the change in the solvent viscosity in both steady and oscillatory motions. The independence of the liquid pressure magnitudes over the solvent viscosity could be explained as follows. In the earlier subsection, the particle pressure is described as $\Pi = \eta_n \dot{\gamma}$ where dependence of the shear rate on the solvent viscosity in the gravity driven flow ($\dot{\gamma} \propto (1/\eta_s)$) implies $\Pi \propto \eta_n \dot{\gamma} \propto \eta_n/\eta_s$. It

is known that the ratio of normal to shear stress, η_n/η_s, is independent of the solvent viscosity η_f [34, 21]. Thus, as Π_1 remain unchanged as η_f is varied (and of course the column head H_1 has no dependence on η_f), equations (7.1) and (7.2) indicate that the magnitudes of the liquid pressures P_1 would remain independent of the η_f. This is, in fact, observed in our experiments. A similar behavior is observed for the liquid pressure P_2.

(a)

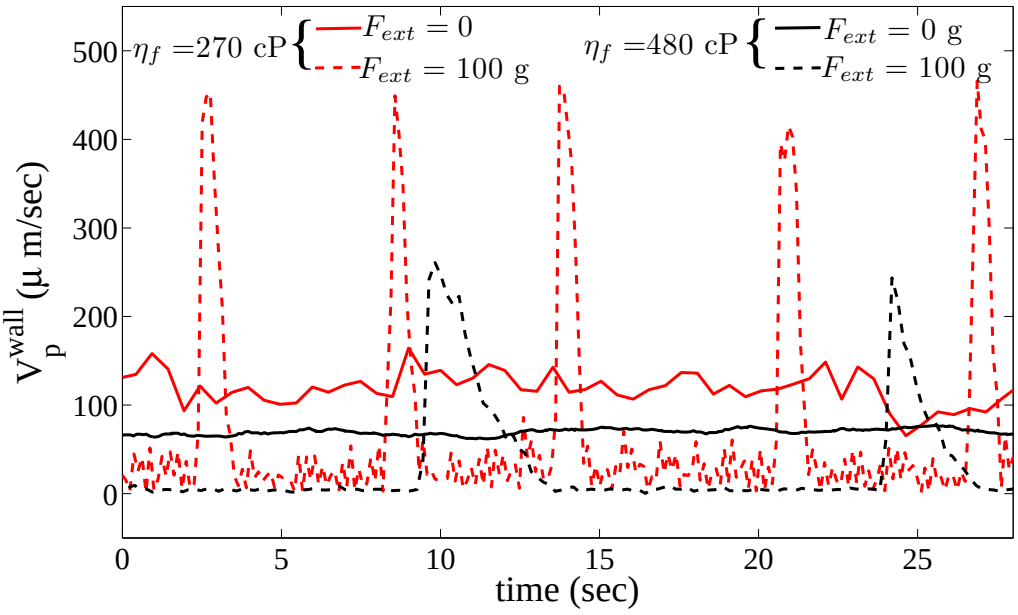

(b)

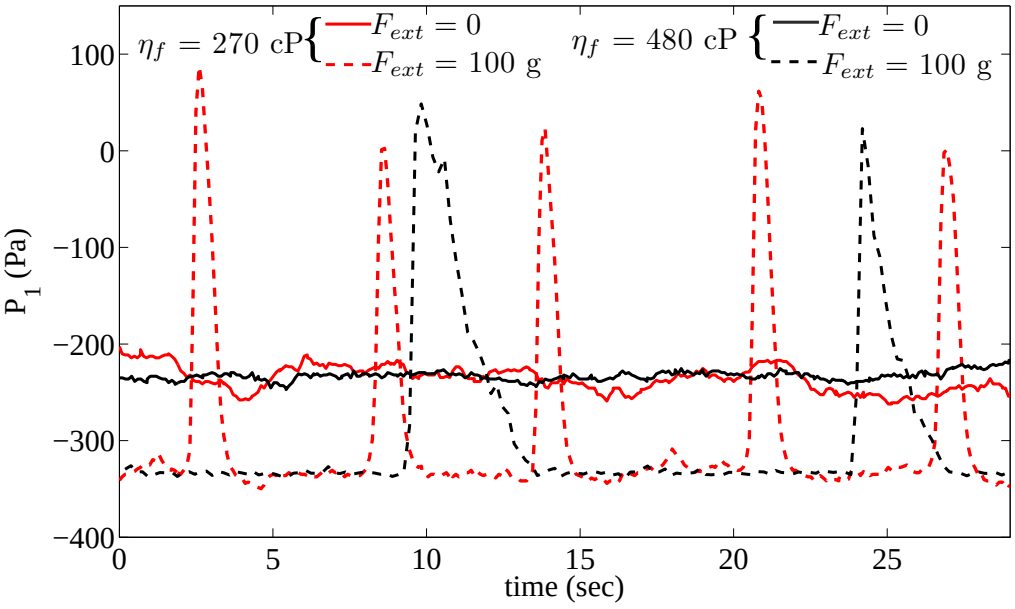

Figure 7.4: (a) The particle speed V_p^{wall} in the contraction channel and (b) the liquid pressure P_1 data at $\phi = 0.58$ for $\eta_f = 270$ cP and $\eta_f = 480$ cP under steady and oscillatory flow conditions.

η_s	τ_{cycle}	τ_{slow}	τ_{fast}
270	4.7 ± 0.4	3 ± 0.4	1.7 ± 0.3
480	14.9 ± 0.7	11.2 ± 0.7	3.7 ± 0.5
880	32.6 ± 2.5	27.2 ± 2.8	5.4 ± 1

Table 7.1: The average time period of the cycle, 'slow' motion and the 'fast' motion of the oscillatory flow for different solvent viscosities at $\zeta = 1/6$ and $\phi = 0.58$ under added solid load of 100 g.

Table 7.1 shows variations in the average time period of the cycle (τ_{cycle}), the 'slow' motion (τ_{slow}) and the 'fast' motion (τ_{fast}) in the oscillatory flow for different solvent viscosities under the added solid load of 100 g. We find that the time period of the oscillatory motion (contributed by increase in the duration of both the 'slow' and 'fast' regimes) goes up with η_f in the studied range. When the solvent viscosity is lowered to $\eta_f = 150$ cP, we observe a smooth flow under the added weight of 100 g. It is interesting to note that the plot of τ_{cycle} vs. η_f is linear which intersects the x-axis of the plot at $\eta_f \approx 170$ cP, and thus the vanishing point of oscillatory behavior indicated by this simple linear fit matches with the experimental observation of the absence of oscillatory motion at $\eta_f = 150$ cP. A further study of this issue is warranted.

7.3.4 Contraction to particle size ratio

In this subsection, the flow behavior is studied for $\zeta = 1/6$ and $\eta_f = 270$ cP for different size particles at $\phi = 0.58$. The ratio of smaller channel width to the average particle diameter $w/d_{avg} = \beta$ is varied from $\beta \approx 10$ for typical 380-500 μm particles ($d_{avg} \approx 420\mu m$) to $\beta \approx 20$ for smaller particles of 150-250 μm diameter ($d_{avg} \approx 200\mu m$). Under no external load, the pressure responses P_1 and P_2 remains unaffected by the change of particle size while the average speed drops by a factor of 4 for the smaller particles. In addition, the effluent concentration ($\phi^m_{out} \approx 0.53$) remains

unaffected by the change in the particle size. The independence of the self-filtration effect on the particle size is surprising as its well known that the Darcy behavior has a strong dependence on the particle size. This behavior is investigated further by conducting rheometric studies on the suspensions with different size particles.

Figure 7.5 shows the suspension viscosity η_s plotted as a function of shear rate $\dot{\gamma}$ at $\phi = 0.50$ and $\phi = 0.58$. The rheological measurements are done in a parallel plate geometry with plate diameter of 2.5 cm in ARES Rheometer (Rheometric Scientific). We observe quite weak shear thinning for $\phi = 0.50$ and fairly strong for $\phi = 0.58$, and clearly it is stronger for the smaller particles. The shear thinning in general is consistent with the earlier experimental studies of non-colloidal suspensions [21, 89]. For $gap/d_{avg} \geq 5$, η_s is independent of the gap size as confirmed by experiments with the suspensions of 150-250 μm particles for $gap/d_{avg} \approx 5$ and $gap/d_{avg} \approx 10$. We compare the rheological properties of the suspensions with different size particles at $gap/d_{avg} \approx 5$. At $\phi = 0.50$, we find that η_s remains independent of the particle size. This agrees with the hard-sphere suspension behavior $\eta_s = f(\phi)\eta_f$ at steady shear and $\eta_s \neq f(d)$ as established by earlier works including theory [90], simulations [18] and experiments [21]. To the contrary, at $\phi = 0.58$, we find that η_s depends significantly on the particle size. For the small shear rates ($\dot{\gamma} < 0.5s^{-1}$), we measure ${\eta_s}^{d_{avg}=200}/{\eta_s}^{d_{avg}=420} \approx 4$. We interpret that the suspension viscosity at $\phi = 0.58$ is influenced by the contact of solid surfaces, thereby making the hydrodynamic arguments of $\eta_s = f(\phi)\eta_f$ invalid. Thus, this agrees with the idea of a deforming porous medium in the contraction experiments and in fact calls into question the validity of describing the material by a 'viscosity' in general geometries.

Based on the rheology, we explain the observed independence self-filtration behavior on the particle size in the contraction geometry at $\phi = 0.58$. The effluent gets diluted as there is flow of liquid relative to the particles $\Delta V = V_l - V_p$. The

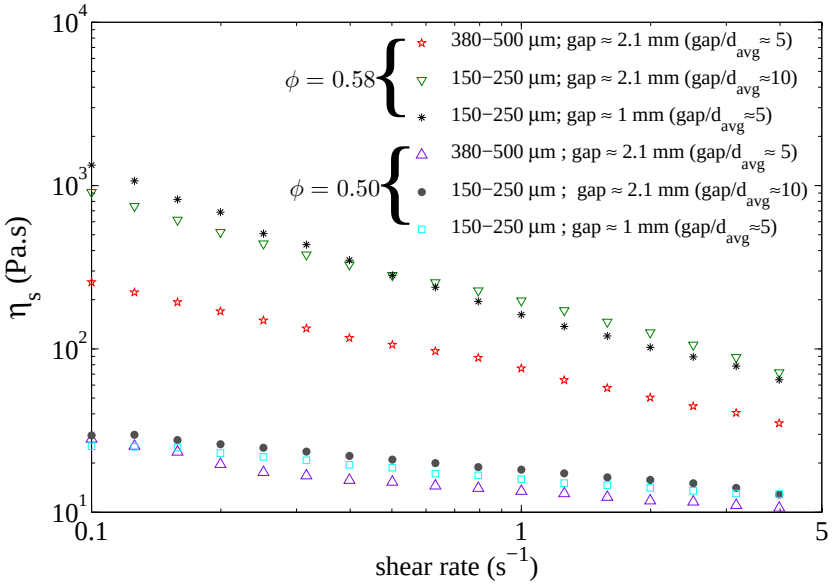

Figure 7.5: The suspension viscosity η_s plotted against shear rate for $\phi = 0.50$ and $\phi = 0.58$. At each concentration, the relative viscosity of 380-500 μm particles is compared with that of 150-250 μm particles for the same gap as well as for the same gap/d_{avg} ratio.

effluent concentration is stated as

$$\phi_{out} = \frac{\phi_{in} V_p}{\phi_{in} V_p + (1 - \phi_{in}) V_l} = \frac{\phi_{in}}{1 + \frac{\Delta V}{V_p}(1 - \phi_{in})}. \tag{7.3}$$

Thus, $\frac{\Delta V}{V_p}$ decides the effluent concentration. We consider that the relative flow of the liquid ΔV is governed by the Darcy flow behavior, $\Delta V \propto \frac{K}{\eta_f}\frac{\Delta P}{L}$, where $K = f(\phi)d^2$. Since the other parameters (ϕ, η_f and pressures P_1 and P_2) are unchanged in the present conditions, the change of particle size from $d_{avg} = 420$ to $d_{avg} = 200$, would cause drop in ΔV by a factor of 4. Coincidentally, our rheological measurements suggest that V_p drops by a factor of 4 when the particle size goes from d_{avg}=420 μm to d_{avg}=200 μm ($\eta_s{}^{d_{avg}=200}/\eta_s{}^{d_{avg}=420} \approx 4$). As ΔV and V_p are affected to the same extent when the particle size is changed, the effluent concentration would be independent of the particle size which is consistent with the experimental observations.

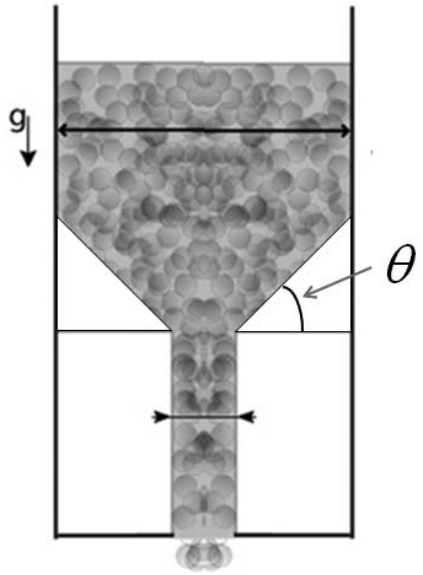

Figure 7.6: Front sketch of the angled contraction with an added slanted piece of plexiglass attached to each rectangular block, which is inclined at an angle θ with respect to the horizontal.

Note that the threshold load needed to induce oscillations is approximately 100 g for the typical particles ($380 - 500\mu$m dia.) while for smaller particles ($150 - 250\mu$m dia.), a load of 500 g is needed to drive the system in the oscillatory mode. Thus, there is strong influence of channel size/particle ratio on the oscillatory flow behavior. This behavior is similar with the observation of Isa *et al.* [80] who studied pressure-driven flow of concentrated colloids through square micro-channels.

7.3.5 Effect of contraction geometry

The results presented earlier are for the flat contraction as shown in figure 7.1a. In this subsection, we describe the suspension flow passing through an angled contractions as shown in figure 7.6. Each of the two additional slanted pieces of plexiglass has same depth as of the inserted rectangular blocks, and the piece is inclined at an angle θ with respect to the horizontal and fixed with each rectangular

Contraction Angle	τ_{cycle} (sec)
$\theta = 0^0$	4.7 ± 0.4
$\theta = 45^0$	4.1 ± 0.5
$\theta = 60^0$	3.5 ± 0.3

Table 7.2: The values of τ_{cycle} for different angled contractions in case of $\zeta = 1/6$ and $\eta_f = 270$ cP under 100 g added solid weight where input particle concentration is $\phi = 0.58$.

block as shown in 7.6.

In case of $\zeta = 1/6$ and $\eta_f = 270$ cP, we compare the flow behavior under 100 g added solid weight at $\phi = 0.58$, when the flat contraction is replaced by angled contraction with $\theta = 45°$ and $\theta = 60°$. It is observed that the periodicity is retained for angled contraction, where the average time period of oscillation τ_{cycle} slightly decreases as θ is raised to 45° and 60° as shown in Table 7.2. Thus, we comprehend that the angled contractions are also able to support the particle-chain network that results in the periodic flow behavior.

7.4 Conclusion

The alternating motion under external solid load is found to be robust, occurring for a range of imposed external loads, solvent viscosities and particle sizes. The phenomenon is studied in relation to the system's internal stress state i.e. the liquid pressure response and observed self-filtration effects. The rheological measurements demonstrate that the dense suspension flow is influenced by the non-hydrodynamic contact forces between the particles. The presence of non-hydrodynamic contact forces may provide a fundamental basis to the observed oscillatory flow in the contraction geometry. A further study to understand the periodic breakage and formation of the particle network, and to provide a predictive model for the 'transient jamming' behavior is required.

Bibliography

[1] M. P. Allen, D. J. Tildesley, Computer Simulation of Liquids, Oxford University Press Inc., New York, 1987.

[2] J. F. Brady, G. Bossis, Stokesian Dynamics, Ann. Rev. Fluid Mech. 20 (1988) 111.

[3] C. S. Campbell, Rapid granular flows, Ann. Rev. Fluid Mech. 22 (1990) 57.

[4] D. L. Koch, R. J. Hill, Inertial effects in suspension and porous media flows, Ann. Rev. Fluid Mech. 33 (2001) 619.

[5] G. K. Batchelor, The effect of Brownian motion on the bulk stress in the suspension of spherical particles, J. Fluid. Mech. 83 (1977) 97.

[6] G. K. Batchelor, J. T. Green, The hydrodynamic interation of two small freely-moving spheres in a linear flow field, J. Fluid. Mech. 56 (1972) 375–400.

[7] G. K. Batchelor, J. T. Green, The determination of the bulk stress is a suspension of spherical particles to order c^2, J. Fluid. Mech. 56 (1972b) 401–427.

[8] G. K. Batchelor, The stress system in a suspension of force free particles, J. Fluid Mech. 41 (1970) 545.

[9] A. P. Arp, S. G. Mason, The kinetics of flowing dispersions. viii. doublets of rigid spheres, J. Colloid Interface Sci. 61 (1977) 21.

[10] R. W. O'Brien, A method for the calculation of the effective transport properties of suspensios of interacting particles, J. Fluid Mech. 56 (1979) 401.

[11] D. J. Jeffrey, Y. Onishi, Calculation of the resistance and mobility functions for two unequal rigid spheres in low-Reynolds-number flow, J. Fluid. Mech. 139 (1984) 261–290.

[12] S. Kim, R. T. Mifflin, The resistance and mobility functions of two equal spheres in low-reynolds-number flow, Phys. Fluids 28 (1985) 2033.

[13] G. Bossis, J. F. Brady, Dynamic simulation of sheared suspensions. I. General method, J. Chem. Phys. 80 (1984) 5141.

[14] D. R. Foss, J. F. Brady, Structure, diffusion and rheology of Brownian suspensions by Stokesian Dynamics simulation, J. Fluid. Mech. 407 (2000) 167.

[15] P. D'Haene, J. Mewis, G. G. Fuller, Scattering dichroism measurements of flow-induced structure of a shear thickening suspension, J. Colloid Interface Sci. 156 (1993) 350.

[16] J. C. van der Werff, C. G. de Kruif, Hard-sphere colloidal dispersions: the scaling of rheological properties with particle size, volume fraction, and shear rate, J. Rheol. 33 (1989) 421.

[17] J. F. Brady, J. F. Morris, Microstructure of strongly sheared suspensions and its impact on rheology and diffusion, J. Fluid. Mech. 348 (1997) 103.

[18] A. Sierou, J. F. Brady, Rheology and microstructure in concentrated noncolloidal suspensions, J. Rheol. 46 (2002) 1031.

[19] J. F. Brady, M. A. Vicic, Normal stresses in colloidal dispersions, J. Rheol. 39 (1995) 545.

[20] F. Gadala-Maria, The rheology of concentrated suspensions, Ph.D. thesis, Stanford University, US (1979).

[21] I. E. Zarraga, D. A. Hill, D. T. Leighton, The characterization of the total stress of concentrated suspensions of noncolloidal spheres in Newtonian fluids, J. Rheol. 44 (2000) 185.

[22] A. Singh, P. R. Nott, Experimental measurements of the normal stresses in sheared Stokesian suspensions, J. Fluid Mech. 490 (2003) 293.

[23] D. Prasad, H. K. Kytomaa, Particle stresses and viscous compaction during shear of dense suspensions, Int. J. Multiphase Flow 21 (1995) 775.

[24] J. F. Morris, B. Katyal, Microstructure from simulated Brownian suspension flows at large shear rate, Phys. Fluids 14 (2002) 1920.

[25] F. Parsi, F. Gadala-Maria, Fore-and-aft asymmetry in a concentrated suspension of solid spheres, J. Rheol. 31 (1987) 725.

[26] I. Rampall, J. R. Smart, D. T. Leighton, The influence of surface roughness on the particle-pair distribution function of dilute suspensions of non-colloidal spheres in simple shear flow, J. Fluid Mech. 339 (1997) 1.

[27] D. Leighton, A. Acrivos, The shear-induced migration of particles in concentrated suspensions, J. Fluid. Mech. 181 (1987) 415.

[28] A. Acrivos, R. Mauri, X. Fan, Shear-induced resuspension in a couette device, Int. J. Multiphase Flow 19 (1993) 797.

[29] C. J. Koh, P. Hookham, L. G. Leal, An experimental investigation of concentrated suspension flows in a rectangular channel, J. Fluid. Mech. 266 (1994) 1.

[30] D. J. Jeffrey, J. F. Morris, J. F. Brady, The pressure moments for two spheres in a low-Reynolds-number flow, Phys. Fluids A 5 (1993) 2317.

[31] Y. Yurkovetsky, J. F. Morris, Particle pressure in sheared Brownian suspensions, J. Rheol. 52 (2008) 141.

[32] A. Deboeuf, G. Gauthier, J. Martin, Y. Yerkovetsky, J. F. Morris, Particle pressure in a sheared suspension : a bridge from osmosis to granular dilatancy, Phys. Rev. Lett. 102 (2009) 108301.

[33] P. R. Nott, J. F. Brady, Pressure driven flow of suspensions: theory and simulations, J. Fluid Mech. 275 (1994) 157.

[34] J. F. Morris, F. Boulay, Curvilinear flows of noncolloidal suspensions: The role of normal stresses, J. Rheol. 43 (1999) 1213.

[35] R. M. Miller, J. F. Morris, Normal stress driven migration and axial development in pressure-driven flow of concentrated suspensions, J. Non-Newtonian Fluid Mech. 135 (2006) 149.

[36] A. Sierou, J. F. Brady, Accelerated Stokesian Dynamics simulations, J. Fluid. Mech. 448 (2001) 115.

[37] A. J. Banchio, J. F. Brady, Accelerated Stokesian Dynamics: Brownian motion, J. Chem. Phys. 118 (2003) 10323.

[38] B. J. Alder, W. G. Hoover, D. A. Young, Studies in molecular dynamics. v. high-density equation of state and entropy for hard-discs and spheres, J. Chem. Phys. 49 (1968) 3688.

[39] P. N. Pusey, W. van Megen, Phase behavior of concentrated suspensions of nearly hard colloidal spheres, Nature 320 (1986) 340.

[40] S. E. Paulin, B. J. Ackerson, Observation of a phase transition in the sedimentation velocity of hard spheres, Phys. Rev. Lett. 64 (1990) 2663.

[41] R. L. Hoffman, Discontinuous and dilatant viscosity behavior in concentrated suspensions I. Observation of a flow instability, Trans. Soc. Rheol. 16 (1972) 155.

[42] B. J. Ackerson, Shear induced order and shear processing of model hard-sphere suspensions, J. Rheol. 34 (1990) 553–590.

[43] M. D. Haw, W. C. K. Poon, P. N. Pusey, Direct observation of oscillatory-shear-induced order in colloidal suspensions, Phys. Rev. E. 57 (1998) 6859.

[44] C. Voltz, M. Nitschke, L. Heymann, I. Rehberg, Thixotropy in macroscopic suspensions of spheres, Phys. Rev. E. 65 (2002) 051402.

[45] L. E. Silbert, J. R. Melrose, R. C. Ball, The rheology and microstructure of concentrated, aggregated colloids, J. Rheol. 43 (1999) 673.

[46] R. J. Butera, M. S. Wolfe, J. Bender, N. J. Wagner, Formation of a highly ordered colloidal microstructure upon flow cessation from high shear rates, Phys. Rev. Lett. 77 (1996) 2117.

[47] S. E. Paulin, B. J. Ackerson, M. S. Wolfe, Microstructure-dependent viscosity in concentrated suspensions of soft spheres, Phys. Rev. E. 55 (1997) 5812.

[48] A. M. Leshansky, J. F. Brady, Dynamic structure factor study of diffusion in strongly sheared suspensions, J. Fluid. Mech. 527 (2005) 141.

[49] S. Phan, W. B. Russel, Z. Cheng, J. Zhu, P. M. Chaikin, J. H. Dunsmuir, R. H. Ottewill, Phase transition, equation of state, and limiting shear viscosities of hard sphere dispersions, Phys. Rev. E. 54 (1996) 6633.

[50] T. N. Phung, J. F. Brady, G. Bossis, Stokesian Dynamics simulation of Brownian suspensions, J. Fluid. Mech. 313 (1996) 181.

[51] H. J. Wilson, An analytic form for the pair distribution function and rheology of a dilute suspension of rough spheres in plane strain flow, J. Fluid. Mech. 534 (2005) 97.

[52] J. P. Hansen, I. R. Mcdonald, Theory of simple liquids, Academic, London, 1986.

[53] P. J. Steinhardt, D. R. Nelson, M. Ronchetti, Bond-orientational order in liquids and glasses, Phys. Rev. B. 28 (1983) 784.

[54] B. J. Berne, R. Pecora, Dynamic Light Scattering, Wiley, New York, 1976.

[55] J. M. Rallison, E. J. Hinch, The effect of particle interactions on dynamic light scattering from a dilute suspension, J. Fluid. Mech. 167 (1986) 131.

[56] J. F. Morris, J. F. Brady, Self-diffusion in sheared suspensions, J. Fluid. Mech. 312 (1996) 223.

[57] A. M. Leshansky, J. F. Morris, J. F. Brady, Collective diffusion in sheared colloidal suspensions, J. Fluid. Mech. 597 (2008) 305.

[58] W. Xue, G. S. Grest, Shear-induced alignment of colloidal particles in the presence of a shear flow, Phys. Rev. Lett. 64 (1990) 419.

[59] J. P. Hansen, L. Verlet, Phase transitions of the Lennard-Jones system, Phys. Rev. 184 (1969) 151.

[60] V. Breedveld, D. V. den Ende, M. Bosscher, R. J. Jongschaap, J. Mellema, Measuring shear-induced self-diffusion in a counter-rotating geometry, Phys. Rev. E. 63 (2001) 021403.

[61] A. Sierou, J. F. Brady, Shear-induced self-diffusion in non-colloidal suspensions, J. Fluid. Mech. 506 (2004) 285.

[62] J. Bergenholtz, J. F. Brady, M. Vicic, The non-Newtonian rheology of dilute colloidal suspensions, J. Fluid. Mech. 456 (2002) 239.

[63] J. J. Stickel, R. L. Powell, Fluid mechanics and rheology of dense suspensions, Ann. Rev. Fluid Mech. 37 (2005) 129.

[64] J. J. Stickel, R. J. Phillips, R. L. Powell, Application of a constitutive model for particulate suspensions: time-dependent viscometric flows, J. Rheol. 51 (2007) 1271.

[65] V. G. Kolli, E. J. Pollauf, F. Gadala-Maria, Transient normal stress response in a concentrated suspension of spherical particles, J. Rheol. 46 (2002) 321.

[66] C. Gao, J. F. Gilchrist, Shear-induced particle migration in 1d, 2d, and 3d flows, Phys. Rev. E. 77 (2009) 025301.

[67] C. Gao, B. Xu, J. F. Gilchrist, Mixing and segregation of microspheres in microchannel flows of mono- and bidispersed suspensions, Phys. Rev. E. 79 (2009) 036311.

[68] D. Dendukuri, S. S. Gu, D. C. Pregibon, T. A. Hatton, P. S. Doyle, Stop flow lithography in a microfluidic device, Lab Chip 7 (2007) 818.

[69] J. C. Crocker, D. G. Grier, Methods of digital video microscopy for colloidal studies, J. Colloid Interface Sci. 179 (1996) 298.

[70] S. D. Kulkarni, J. F. Morris, Ordering transition and structural evolution under shear in Brownian suspensions, J. Rheol. 53 (2009) 417.

[71] E. Bertrand, J. Bibbete, V. Schmitt, From shear thickening to shear induced jamming, Phys. Rev. E. 66 (2002) 060401.

[72] D. Lootens, H. van Damme, P. Herbraud, Giant stress fluctuations at the jamming transition, Phys. Rev. E. 90 (2003) 178301.

[73] M. D. Haw, Jamming, two-fluid behavior, and 'self-filtration' in concentrated particulate suspensions, Phys. Rev. E. 92 (2004) 185506.

[74] R. C. Ball, J. R. Melrose, Lubrication breakdown in hydrodynamic simulations of concentrated colloids, Adv. Colloid Interface Sci. 59 (1995) 19.

[75] Y. Yurkovetsky, J. F. Morris, Triplet correlation in sheared suspensions of brownian particles, J. Chem. Phys. 124 (2006) 204908.

[76] R. S. Farr, J. R. Melrose, R. C. Ball, Kinetic theory of jamming in hard-sphere startup flow, Phys. Rev. E. 55 (1997) 106365.

[77] B. J. Maranzano, N. J. Wagner, Flow-small angle neutron scattering measurements of colloidal dispersion microstructure evolution through the shear thickening transition, J. Chem. Phys. 117 (2002) 10291.

[78] N. J. Wagner, W. B. Russel, Nonequlibrium statistical mechanics of concentrated colloidal dispersions: hard spheres in weak flows with many-body thermodynamics interactions, Physica A 155 (1989) 475.

[79] J. F. Brady, Computer simulations of viscous suspensions, Chem. Engg. Sci. 56 (2001) 2921.

[80] L. Isa, R. Beselling, A. N. Morozov, W. C. K. Poon, Velocity oscillations in microfluidic flows of concentrated colloidal suspensions, Phys. Rev. Lett. 102 (2009) 058302.

[81] M. Pailha, O. Pouliquen, A two-phase flow description of the initiation of underwater granular avalanches, J. Fluid. Mech. 633 (2009) 115.

[82] P. Yaras, D. M. Kalyon, U. Yilmazer, Flow instabilities in capillary flow of concentrated suspensions, Rheol Acta. 33 (1994) 48.

[83] S. Rough, J. Bridgwater, D. Wilson, Effects of liquid phase migration on extrusion of microcrystalline cellulose pastes, Int. J. Pharm. 204 (2000) 117.

[84] S. S. L. Peppin, J. A. W. Elliott, M. G. Worster, Pressure and relative motion in colloidal suspensions, Phys. Fluids 17 (2005) 053301.

[85] R. M. Miller, J. P. Singh, J. F. Morris, Suspension flow modeling for general geometries, Chem. Engg. Sci. 64 (2009) 4597.

[86] R. M. Iverson, M. E. Reid, R. G. LaHusen, Debris flow mobilization from landslides, Annu. Rev. Earth Planet. Sci. 25 (1997) 85.

[87] C. Cassar, M. Nicolas, O. Pouliquen, Submarine granular flows down inclined planes, Phys. Fluids 17 (2005) 103301.

[88] Y. Bertho, F. Giorgiutti-Dauphine, J. Hulin, Dynamical janssen effect on granular packing with moving walls, Phys. Rev. Lett. 90 (2003) 144301.

[89] D. T. Leighton, A. Acrivos, Viscous resuspension, Chem. Eng. Sci. 41 (1986) 1377.

[90] J. F. Brady, The rheological behavior of concentrated colloidal suspensions, J. Chem. Phys. 99 (1993) 567.